Lubricated Rolling Over a Pool

by

Hatef Rahmani

M.A.Sc., The University of British Columbia, 2016

A THESIS SUBMITTED IN PARTIAL FULFILLMENT OF

THE REQUIREMENTS FOR THE DEGREE OF

DOCTOR OF PHILOSOPHY

in

THE FACULTY OF GRADUATE AND POSTDOCTORAL STUDIES

(Mechanical Engineering)

THE UNIVERSITY OF BRITISH COLUMBIA

(Vancouver)

December 2021

The following individuals certify that they have read, and recommend to the Faculty of Graduate and Postdoctoral Studies for acceptance, the dissertation entitled:

Lubricated Rolling Over a Pool

submitted by Hatef Rahmani in partial fulfillment of the requirements for

the degree of Doctor of Philosophy

in Mechanical Engineering

Examining Committee:

Sheldon Green, Professor, Mechanical Engineering, UBC
Co-supervisor

Boris Stoeber, Professor, Mechanical Engineering, Electrical and Computer Engineering, UBC
Co-supervisor

Neil Balmforth, Professor, Department of Mathematics, UBC
Supervisory Committee Member

Dana Grecov, Professor, Mechanical Engineering, UBC
Supervisory Committee Member

James Feng, Professor, Chemical and Biological Engineering, Department of Mathematics, UBC
University Examiner

Gwynn Elfring, Associate Professor, Mechanical Engineering, UBC
University Examiner

Roger Lewis, Professor, Mechanical Engineering, The University of Sheffield
External Examiner

Additional Supervisory Committee Members:

Mark Martinez, Professor, Chemical and Biological Engineering, UBC
Supervisory Committee Member

Savvas Hatzikiriakos, Professor, Chemical and Biological Engineering, UBC
Supervisory Committee Member

Mu Chiao, Professor, Mechanical Engineering, UBC
Supervisory Committee Member

Abstract

The focus of this research is the rolling of a cylinder over a pool of viscous fluid. This process has many industrial applications such as roll coating, lubrication of bearings, and rail transport (the primary motivator of this research). The problem is studied for Newtonian and shear-thinning fluids. The speed, width and loading of the cylinder are varied as are the initial depth and length of the viscous pool. Depending on the operating conditions, the cylinder will either ride on a lubrication film or remain in solid contact with the underlying substrate (although in the wheel/rail interface, there could also be a mixed or boundary lubrication regime). For the former situation, a lubrication theory is provided to predict the pressure underneath the cylinder and the film thickness deposited on the substrate. To account for the flux of fluid escaping towards the cylinder edges (3D effects), an approximation of the lubrication theory is used that includes an adjustable parameter. Once this single parameter is calibrated against experiment, the theory predicts peak lubrication pressures, gap sizes and film thicknesses to within about ten percent. The printer's instability arises during the splitting process, patterning the residual fluid films on the substrate and cylinder. If the pool length is less than the cylinder circumference, the fluid adhering to the cylinder is rotated back into contact with the substrate, and when there is sufficient adhered fluid a lubrication film forms that can again be modelled by the theory. Conversely, if there is insufficient adhered fluid, no contiguous lubrication film is formed; instead the pattern from the printer's instability "prints" from the cylinder to the substrate.

A field experiment was conducted to understand the initial pickup of the liquid by the train wheel and subsequent carrydown along the track. Due to the high wheel-rail contact pressure, the liquid failed to form a lubrication layer (not the preferred outcome) and was squeezed out laterally,

adhering to the edges of the wheel contact band. This edge liquid, however, provides tribological benefits on the curved track due to movement of the contact band as the train rounds a curve.

Lay Summary

Liquid friction modifiers (LFMs) are applied to the wheel-rail interface to manage friction between the wheel and rail. A pool of liquid is deposited on the track ahead of the approaching train. The liquid pool is overridden by an advancing wheel, picked up by the wheel and transferred down the track. Although this process has been used for many years, it is important to further understand the fluid behavior at the wheel-rail interface. A novel experimental apparatus was developed that mimics some key aspects of realistic rail conditions, and experimental and theoretical studies were performed on this device. The focus was to understand the fluid flow in a simplified contact and then translate it to the actual contact. The findings of this research will be used to further improve the product formulations and its application to the track.

Preface

This PhD thesis entitled “Lubricated Rolling Over a Pool” is original work carried out by the author, Hatef Rahmani, under the supervision of Professor Sheldon Green, Professor Boris Stoeber, and Professor Neil Balmforth. The experiments were mostly conducted at Applied Fluid Mechanics (AFM) lab, located at Pulp and Paper Centre. The following papers are in progress for publication:

- A version of Chapter 2 has been accepted for publication in the Journal of Fluid Mechanics. The author of this thesis was the principal contributor to this publication. Prof. Green, Prof. Stoeber, and Prof. Balmforth supervised the research and assisted with data analysis, model derivation, and writing the paper.

- A version of Chapter 3 will be submitted to a peer-reviewed journal shortly. The author of this thesis was the principal contributor to this publication. Prof. Green, Prof. Stoeber, and Prof. Balmforth supervised the research and assisted with data analysis, model derivation, and writing the paper.

- A version of Chapter 4 has been submitted to a peer-reviewed journal and is currently under review. The author of this thesis was the principal contributor to this publication. Prof. Green and Prof. Stoeber supervised the research and assisted with discussion, data analysis and writing the paper. Dmitry Gutsulyak and Louisa Stanlake from LB Foster Rail Technologies contributed to this paper by providing insightful discussion and coordinating the field

experiments. Dmitry Gutsulyak also helped with conducting the experiments at the site and collecting data.

Table of Contents

List of Tables

List of Figures

Nomenclature

C	Free constant in the model for a wide wheel
C'	Free constant in the model for a narrow wheel
Ca	Capillary number
$h(x)$	Gap size
h_0	Minimum gap
h_{in}	Initial pool depth
h_l	Gap size at the jump
h_m	Gap size at the meniscus
h_{out}	Deposited film thickness
K	Consistency index
L	Wheel load
L_0	Initial pool length
l_c	Steady state length
l_p	Plowing length
n	Power-law index
$\hat{\boldsymbol{n}}$	Normal vector
p	Fluid pressure
$\overline{p}$	Average pressure across the wheel width
P	Dimensionless pressure
p_{atm}	Atmospheric pressure
p_{vap}	Vapor pressure
Q_{in}	Incoming flux
R	Wheel radius
$\mathcal{R}$	Length scale ratio (lubrication length scale to the wheel width)
Re	Reynolds number
R_c	Radius of crowning
U	Cylinder/substrate speed

$\boldsymbol{u} = (u, v, w)$	Velocity vector
W	Wheel width
We	Weissenberg number
x_l	Position of the upstream jump
x_m	Position of the meniscus
λ	Dimensionless flux
η	Dimensionless y
ρ	Fluid density
μ	Fluid viscosity
μ_a	Apparent viscosity
γ	Surface tension
$\dot{\gamma}$	Shear rate
θ	Contact angle
ξ	Dimensionless x

Acknowledgements

I would not have been able to complete this research without help and instruction of several individuals. I would like to take this opportunity and thank them all in my humble acknowledgment. First and foremost, special thanks to my diligent supervisors, Prof. Sheldon Green, Prof. Boris Stoeber, and Prof. Neil Balmforth whose insight and knowledge into the Fluid Mechanics steered me through this research. I am deeply grateful to you for your continued support, guidance, effort, and significant time you devoted to this research from the early on. Sheldon and Boris, thank you for teaching me how to be a fluid experimentalist, and Neil, thank you for teaching me how to apply my mathematical skills to the real-world problems.

Many thanks are owed to my PhD advisory committee members, Prof. Grecov, Prof. Martinez, and Prof. Hatzikiriakos for their valuable feedback, advice, and comments from the early stage of my thesis till the end.

I also had great pleasure working and collaborating with Drs. Dmitry Gutsulyak and Louisa Stanlake from LB Foster Rail Technologies. Their guidance and valuable insights during our monthly meetings helped me to make great progress in my research. They also provided commercial samples for the research, trained me to use the equipment at the LB Foster, and contributed to the field experiments. Financial supports of the LB Foster Rail Technologies and NSERC are also gratefully acknowledged.

I would like to thank my lab-mates during this research who became my friends over time. In particular, I like to thank Dr. Amir Farzad Forughi and Arthur Rostami who, on multiple occasions, devoted time and helped me with the experiments and results interpretations. I extend my appreciation

to Omid Eghraghy, Athena Liu and Hooman Mahdavi (my current lab-mates and friends) for being there when I needed them.

Last but not least, my debt of gratitude is to my parents and family. In particular, my sister Hoda who unconditionally supported me through this journey.

Dedication

To my family

For their unconditional love,

Encouragement, and

Endless support.

Chapter 1: Introduction

1.1 Motivation

Rail transport is one of the most efficient and cost-effective forms of freight and passenger transportation in North America. The railroad sector in Canada includes more than 72,000 kilometers of track, and transports more than 270 million tons of freight and 70 million people annually [1]. Railways will continue to be in demand as alternative methods such as ground and air freight are relatively less cost-effective. To meet the growing demands for both passenger and freight trains, a high-efficiency railway system is essential. It has been shown that through an integrated approach, railroad industries can manage the energy consumption, the lateral force on the track (I use "rail" and "track" interchangeably in this thesis), noise, and the wheel-rail wear [2]–[4].

Friction management at the wheel-rail interface can significantly improve the energy consumption of the train. At the wheel-rail interface resides an intermediate layer, denoted by the third body layer (Figure 1-1), comprised of wear particles and other contaminants from the surrounding. From a tribological perspective, it is recommended to introduce the liquid friction modifiers (LFMs) to the third body layer to reduce shear between rubbing surfaces. Field trials have shown that LFMs can reduce fuel consumption by 6-9% while maintaining sufficient friction to permit safe breaking and slope climbing [5]. In addition, LFMs provide significant benefits such as extended rail life, reduction in noise (by 10-12%), reduction in wheel-rail wear, reduction in track corrugation and damage from rolling contact fatigue, which is a major cause of the derailment [6]. LB Foster Friction Management, among other railroad companies, is currently researching to optimize railway system management.

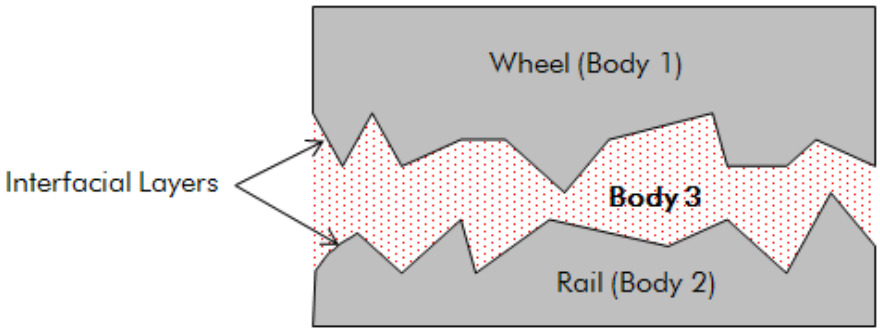

Figure 1-1 Third body layer (TBL) in the wheel-rail interface

As illustrated in Figure 1-2, depending on the application and the desired friction regime, different products may be applied to the wheel/rail interface. For instance, in heavily deciduous forested areas, where wet leaves on tracks can reduce the wheel-rail traction to dangerously low levels, traction enhancers are used [7], [8]. The product can increase the friction in the leaf-contaminated third body and permit safe breaking. On the contrary, where a reduction in energy consumption is required, the rail is coated with a low-friction material that reduces the friction to an intermediate level. Dry rail has a high coefficient of friction ($\boldsymbol{\mu = 0.5 - 0.7}$), and using the LFM, a coefficient of friction $\boldsymbol{\mu \approx 0.3}$ is achieved [9]. In this study, the focus is on friction modifiers, which are water-based top-of-rail products.

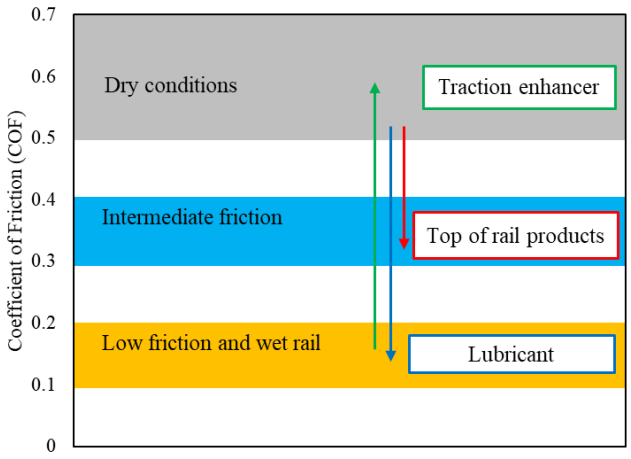

Figure 1-2 Friction regimes in wheel/rail interface, showing the product used for each regime

Depending on the amount of product present in the contact, three lubrication regimes are possible between the wheel and the rail, as shown in Figure 1-3[9]. This diagram is often known as Stribeck curve. In boundary lubrication, there is a constant contact between two surfaces, although minute amount of products may be present. In mixed lubrication, there is a partial contact between two surfaces, and in hydrodynamic lubrication, the two surfaces are completely separated by a thin film.

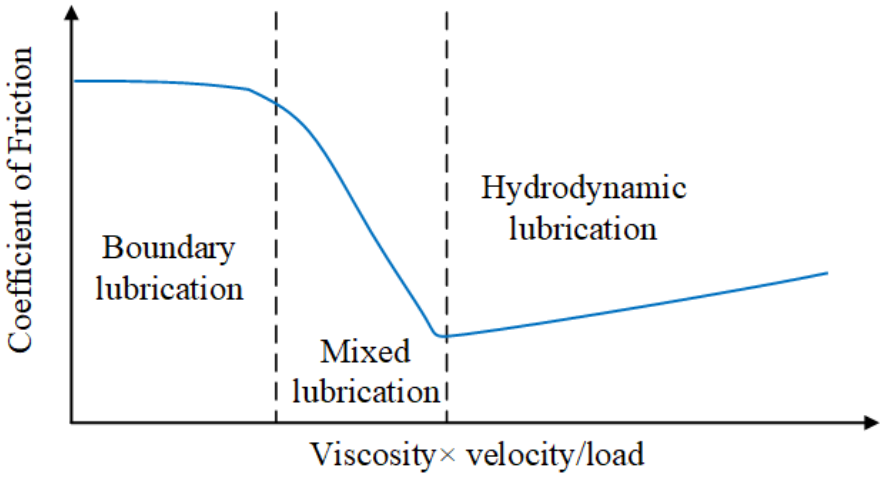

Figure 1-3 Lubrication regimes for liquid products (adapted from [9])

1.1.1 Liquid friction modifiers (LFMs)

Research is ongoing to develop a highly effective liquid friction modifier. LFMs are typically water-based suspended polymers and inorganic solids, and often contain anti-wear additives [10]. Kelsan Technological Corporation (now a part of LB Foster) has produced several friction modifiers (proprietary products) for various applications. One of the commercial LFMs used in practice is a water-based suspension, named KELTRACK. KELTRACK is a shear-thinning fluid that exhibits viscoelastic behavior [11]. Several researchers studied the impacts of coating the rail

with KELTRACK, and they observed the tribological benefits, such as reductions in friction, lateral force, and wear [5].

1.1.2 Modes of application

LFMs are typically applied to the wheel-rail interface in two ways: onboard application and trackside application (the subject of the present thesis). In onboard applications, an atomizer or a nozzle is mounted on a moving train. The liquid is deposited to the top of rail (TOR) in the form of atomized droplets or continuous jets. However, this application has some inherent problems: first, the atomized droplets or continuous jets are sometimes excessively deflected by the cross-wind. As a result, the liquid may never reach the track surface, resulting in poor transfer efficiency. In addition, this application method causes some implementation difficulties as it requires a large reservoir in the train to store fluids and also requires a high-pressure supply for atomizer operations.

To eliminate these challenges, a different approach is used. In trackside applications, an applicator unit is stationary and is located near the rail, pumping the liquid to the top of the track (shown in Figure 1-4 (a) and (b)). The manufacturers recommend this system for applications where a long section of the rail to be covered with LFMs [12]. A pool of LFM is deposited on the rail ahead of the approaching train. Then this pool is overridden by the advancing wheel, spreading the liquid and coating both the wheel and rail surfaces. This process is governed by hydrodynamics. When the wheel contacts the liquid pool, the lubrication pressure builds up in the pool. In some cases, this lubrication pressure is sufficient to raise the wheel slightly off the track. The LFM passes through this gap and the liquid film splits at the downstream meniscus behind the wheel, with part of the LFM adhering to the wheel and part remaining on the track (Figure 1-4(c)). The portion adhering to the wheel is transferred further down the track (henceforward referred to

as "carry-down"- defined as the distance from the application unit up to a point where the tribological benefits are no longer noticeable.), where it may be deposited back onto the track. Trackside applicators are usually located before the track's curve section, where the need for friction management is the greatest.

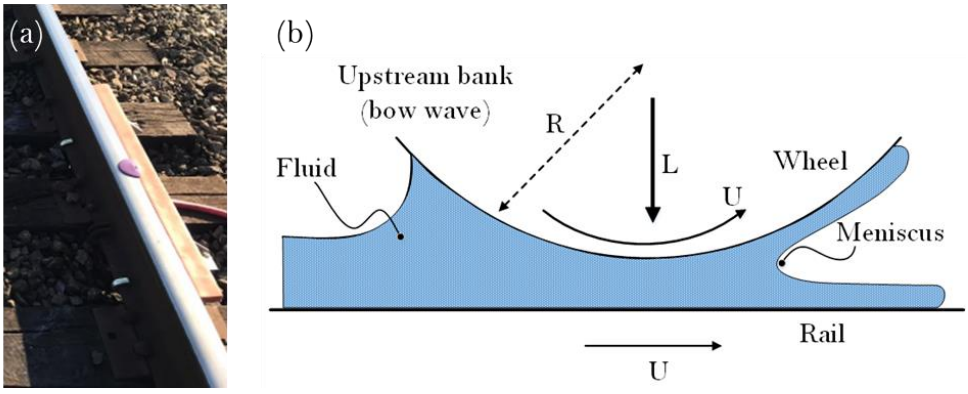

Figure 1-4 Liquid pool on the track prior to the passage of the train (a), and the schematic to describe the fluid dynamics of the rolling mechanism and film splitting in a roller-plate configuration (b). In the frame of reference of the wheel axle, the liquid pool approaches with speed U and the wheel circumference has the same speed. L is the load applied to the wheel. The liquid film carried through the nip splits at the downstream meniscus.

In order to assess and improve the trackside application, it is key to understand the fluid dynamics of this rolling and the "carry-down" by subsequent revolutions of the contaminated wheel. Many questions are of interest to the railroad industry, yet little is known to address them [13]. Some key questions include:

- Is liquid able to support the applied load on the wheel and stay in the wheel-rail contact? Or is it get squeezed out of the contact band due to high contact pressure?
- Does the coating film thickness depend on the fluid's rheological properties and operating conditions?

- How can one achieve optimal initial product pickup and carrydown efficiency? What is the best approach to study carrydown?
- In general, how does the knowledge of the fluid flow in the simplified version of the wheel/rail contact aid the real application?
- How do non-Newtonian properties alter our answers to the previous questions?

This study aims to answer these questions.

1.2 Literature review

The aim of this section is to review some related works to that of the lubricated fluid flow in the wheel/rail interface. This problem has not been extensively studied in the context of the railroad industry, however useful conclusions can be drawn from analogous studies, two of which are the classical coating flows and hydrodynamic levitation. Hydrodynamic levitation is a new set of experiments recently proposed by Eggers et al [14], Mullin et al [15], and Dalwadi et al. [16], where they showed that a solid object can be held aloft by a vertical moving belt coated with a thin layer of viscous fluid. Coating flows and hydrodynamic levitation are discussed in detail in the remainder of this section.

1.2.1 Coating flows

In those situations that the liquid raises the wheel off the track and forms a lubrication film, the problem becomes analogous to the classical coating flows. Coating flow is a longstanding industrial process through which a thin layer of fluid is applied to an underlying substrate [17]. Coating flows have been extensively studied in the literature [18]–[28]. Weinstein and Ruschak [29] presented a detailed summary of those works. In coating flows, fluid is carried into the narrow gap between two rotating rolls or one rotating roll and one translating sheet, the exact geometry

depends upon the coating application. The fluid passes through the nip and then splits downstream of the nip and deposits on the underlying moving sheet. The process can be symmetric, where the rolls radii and speeds are the same, or it can be asymmetric. The process is called forward coating, where rolls are counter-rotating, and is called reverse coating when rolls are co-rotating. There is a clear distinction between forward and reverse roll coating, particularly for the regions before and after the nip where fluid/air interfaces are formed [27], [30]. The upstream may be flooded where the incoming flux (or the incoming thickness) exceeds the flux through the nip or starved when the incoming thickness is equal to or less than the gap size between two rolls [31], [32]. The roll coating can be further categorized using either rigid or elastic (allowing for elements to deform) rolls [33], [34]. Hence, our lubricated problem is similar to the forward roll coating with roll-sheet configurations and with rigid surfaces. The upstream may be flooded or starved, depending on the fluid flux entering the nip (to be discussed). It is noted that there are several distinctions between the coating flow, for which there is a prescribed gap between two surfaces and liquid is carried to the nip from a pool of liquid, and the current problem, for which there is a prescribed normal load applied to the wheel. These distinctions lead to many important, but different, features in the behavior of the fluid.

In the coating flow, the steep rise in pressure acts as a pump at the fluid inlet, pushing the fluid into the narrow gap. As the film goes through the gap, the pressure starts to drop. At the nip exit, the film is subjected to flow in a direction normal to the surfaces, causing negative pressure. Once the negative pressure sufficiently develops, the liquid splits into two layers, coating each surface. At slower roll speeds, film splitting occurs smoothly, whereas at higher roller speeds, cavitation and bubble formation occur [35]. The competition among viscous, capillary, pressure, and elastic forces governs the problem and determines how much liquid is carried through the nip

[36]. As a result, one can control the coating thickness for a variety of liquid properties and loads. Ideally, it is desired that the fluid coats the surface uniformly. However, except in some conditions (purely two-dimensional and low-speed film splitting), films are usually non-uniform (ribbed pattern) in the transverse direction, due to the instabilities at the time of film separation [23] (to be discussed).

Coating flows are traditionally studied within a classical lubrication framework, but the approximation fails near fluid/air free surfaces. In the lubrication analysis, the flow geometry is divided into two regions [18]: i) outer problem (lubrication region or nip region); where the pressure is scaled with the viscous forces and the lubrication approximations apply, ii) inner problem (flow regions before and after the nip); where there is a free surface. The lubrication-based analysis fails to explain the front and back menisci, where the surface tension effects may be significant (characterized by Capillary number). It has been shown that the leading order pressure is generated in the nip, and the local behavior of the flow near free surfaces does not significantly affect the global behavior of the system [37], [38]. The lubrication equation predicts the pressure distribution in the nip, from which it is possible to predict a force that tends to separate two surfaces. However, one still needs to impose boundary conditions on free surfaces to close the equation system. Typically, there is a boundary condition for pressure on either end of the nip region, and if the film-forming meniscus is present, one additional condition is required to determine the meniscus position [29], [39]. Selecting the appropriate boundary condition can be challenging and give rise to a number of recurring issues in these types of flow [40]–[44]. In particular, it is more complicated for the downstream meniscus in view of the severe low pressures that are achieved there, the cavitation that likely results and the so-called printer's instability. The

question of what boundary conditions to use has long been of interest to theoreticians studying the coating flows, some of which will be discussed next.

In pioneering work, Coyle et al. [18] presented a steady two-dimensional lubrication- based model and 2D numerical computations for the Newtonian flow in forward roll coating. In more generality, they studied the problem through three different perspectives: 1) the classical lubrication theory, 2) matched asymptotic expansion, which was first presented by Ruschak [40], 3) the full solution to the Navier-Stokes equation near fluid/air interfaces using a numerical approach. They used the numerical solutions to the Navier-Stokes equations to validate the first two approximations. In addition, they discussed the possible boundary conditions for the meniscus in the lubrication theory and specified the conditions under which they can be used. Among those, the most straightforward case was for the fully submerged rolls, where the pressure at a known meniscus location is set to zero [45]. Another possible boundary condition was to set the pressure and pressure gradient at the meniscus to zero. This boundary condition is most suited for an irregular film splitting (as discussed by [46]). Alternatively, one can set the pressure and velocity to zero at a point midway between two surfaces at the downstream meniscus (in this model, the pressure distribution terminates at a location that is both a stagnation point and a separation point [22]). This is suited for a smooth film separation (as discussed by [41]). Considering only the smooth flow-separation regime, Coyle et al. [18] predicted the coating thickness on the roll as a function of the rolls' speed ratio. They also specified the limitations and ranges of Capillary number and gap-to-radius ratio $\frac{H_0}{R}$, in which each approximation may apply. The lubrication approximation is accurate in the limit of high Capillary number, and the asymptotic approach is applicable when $\frac{H_0}{R} < 0.001$ and $Ca > 0.1$. Savage [47] reviewed the early theories concerning the approximations

for the boundary conditions and cavitation in a journal bearing, a similar problem. In journal bearings, the flow between two eccentric cylinders with inner rotating, is similarly analyzed by the lubrication approximation.

Ruschak [40] was among the first to propose a formal procedure to supply a boundary condition at the point of formation of the fluid/air interface to complete the lubrication equations. He asymptotically matched the pressure in the outer region to that of the inner region, hence providing a boundary condition for pressure and pressure gradient at the free surface meniscus.

Unlike downstream meniscus, less attention has been given to the upstream jump in film thickness at the fluid inlet [37], [48], [49]. There is an essential distinction between an inlet problem and an analogous outlet problem. That is, in many coating applications, the upstream is either flooded (i.e., the fluid flux supplied to the system exceeds the flux passing through the nip) or "pre-metered" (i.e., the fluid flux far upstream the nip is *a priori* known), which makes the inlet problem less interesting [37]. In contrast, the downstream is "self-metered", and the fluid flux at the meniscus is *a priori* unknown. In fact, the flux at the meniscus has to be determined as a part of the solution to the lubrication equation. This flux is of great importance as it determines the final coating film thickness on the surface [36].

In this study, to develop a theoretical model, I make some simplifications by introducing cruder approximations to deal with the inlet (jump bank) and outlet (meniscus) conditions. In previous work on the two-dimensional version of the problem, matched asymptotic expansions are exploited to treat those regions more accurately than in the lubrication analysis, which formally breaks down owing to sharp streamwise gradients. The matched asymptotics allow one to incorporate a more faithful representation of the jump and film splitting, albeit at the expense of treating the full fluid mechanical problem at these locations [18][40][16]. Rather than dealing with

such complications, and because the flow under the rolling wheel inevitably becomes three-dimensional (particularly at film splitting) and may cavitate, I opt for the cruder approach of replacing these finely scaled regions by simple, but plausible boundary conditions on the lubrication theory along the lines discussed by Coyle et al. [18].

1.2.2 Hydrodynamic levitation

Our lubricated flow is even more similar to the levitation of a cylinder/block by a thin layer of viscous fluid [14], [15], [50]. More recently, Eggers et al. [14] revealed an interesting experiment where they placed a cylinder horizontally on a vertical moving belt. The belt was uniformly coated with a very viscous oil. They observed that at the specific rate of the belt speed, the cylinder maintains its balance on the belt and is rotating freely around its axis in a stable position. At the higher belt speeds, the cylinder starts to move in the direction of the belt (upward in this case), and downward for the lower speeds. The viscous stresses generated within the viscous fluid supports the cylinder weight. They presented a simple lubrication model to understand the theoretical basis for this experiment. While successful in explaining the key features of the fluid dynamics, there was a mismatch between their experiments and the theoretical predictions. The mismatch was attributed to the lack of numerical simulations to understand the inner problems (free surfaces), where the film on the cylinder coalesces (separates) with (from) the film on the belt (the film on the cylinder was allowed to return to the nip). They assumed a very simple geometrical constraint, where an upstream film with a known height meets the cylinder surface, to determine the position of the upstream boundary.

This study was extended to the levitation of a block, replacing the cylinder with a rectangular block/cube [15]. For the levitated block, the problem is simplified in a sense that the

lubrication region is no longer a free boundary problem, where the two ends of the nip region are *priori* unknown. In fact, in block levitation, the two ends of the block are also the start and end of the lubrication region, reducing two degrees of freedom from the system. Although experimentally more challenging, they showed that similarly it would be possible to achieve the balance for the block, even for a broader range of the belt speeds. In addition, they observed that the fluid flux entering the nip exceeds the flux leaving the nip; therefore, the fluid is accumulated ahead of the block (similar to jump bank in Figure 1-4(c)). As a result of excessive feed to the nip, the liquid started to run back down the belt (referred to as the fluid 'tongue'). Through image processing, they were able to estimate the length and speed of the fluid tongue for different test conditions.

Similar problems were also explored in a different setting [51]–[53]. A paper by Bico et al. [51], is an example where they studied the rolling of a solid sphere on a smooth tilted wall, lubricated with a thin layer of viscous fluid (the film thickness is of the order $50 - 100\ \mu m$). In the case of solid-solid contact, the sphere rolls down the wall at a constant acceleration. However, once the wall is coated with lubricated fluids, the sphere motion becomes steady under certain conditions. They explored the impacts of the operating conditions (sphere radius and tilt angle) and fluid properties (layer thickness, surface tension, viscosity, and density) on the sphere's constant velocity. While providing many interesting experimental insights to the problem, their attempts to theoretically model the observations failed due to the complexities arising from the three-dimensional free surface around the front and back menisci.

Our theoretical analysis broadly follows that provided by [14]–[16], although here I must also deal with the finite width of the wheel, which permits significant amounts of fluid to leak out sideways.

1.2.3 Experiments on coating flows

In addition to these theoretical analyses, nip flows and film splitting have been studied experimentally for decades. The experiments often include measurement of the coating thickness and interface location, visualizations of the flow-field in the nip, measurements of the fluid pressure and velocity, and discussing the instabilities at the free surfaces [25], [54]–[57]. Arguing the inherent challenges for the theoretical and computational analyses, Benkreira et al. [25] studied the roll coating experimentally for both Newtonian and non-Newtonian fluids. They examined the fluid flux through the nip and the flux distribution after leaving the nip for various experimental conditions. They proposed a simple correlation for the volumetric flow distribution as a function of rolls speed ratio ($\frac{q_1}{q_2} = a(\frac{U_1}{U_2})^b$), where free constants were fitted to the experimental data.

Schweizer [58] was the first to present a flow visualization technique to display the streamlines and free surface profiles of the fluid flow. He managed to visualize the small-scale films by introducing the tracer dye to the liquid. The pictures clearly showed the merge of two liquids on an inclined plane and the free surface profiles in the slide coating application, which were compared against the available computer simulations. This method was later adjusted and used for slot coating [59], multilayer slot coating [60], and roll coating [61].

Subsequently, the evolution of the experimental techniques resulted in more direct quantitative knowledge of the meniscus shape and instantaneous velocity field in the fluid [54], [55], [57]. Decre et al. [54] performed extensive measurements on the meniscus shape and its position in the forward roll coating using the laser-induced fluorescence (LIF) technique. From the meniscus profiles, it was therefore, possible to obtain the flux through the gap and its distribution on each surface. The meniscus tip positions were mapped as a function of the Capillary number and compared with the theoretical predictions. For larger Capillary numbers, the meniscus moved

closer to the minimum gap location. Moreover, they concluded that the theoretical predictions, derived by assuming the flooded upstream, may not be sufficient to explain the fluid flow behavior near the meniscus profile. Hence, one needs to include the upstream bank into the analysis.

Particle tracking velocimetry (PTV) and particle image velocimetry (PIV) were also used to evaluate the nip flows [57], [62]. For the first time, Carvalho et al. [57] used PIV to measure the instantaneous velocity field of the flow near the free surface meniscus, in a rotating-roll and stationary-plate configuration. Many challenges arose for the optical technique due to the strong curvature of the meniscus, small-scale flow, and restricted optical access. The velocity fields near the meniscus revealed a large recirculation area, attached to the free surface. Below the critical Capillary number ($Ca \approx 0.54$, in their study), the flow was 2D. Above that threshold, the flow became 3D (this is apparent by looking at the velocity vectors presented in [57]).

Nip pressure measurement

Knowledge of the nip pressure is crucial to enhance the fundamental understanding of the flows in a narrow gap. It is also key to assess the load-supporting capacity of the system. Several researchers attempted to measure the pressure profiles experimentally [34], [63]–[69]. Keller [63] was the first to measure nip pressures using a force sensor. While providing some interesting results which agreed with the theories, their measurement was only limited to the positive pressure region. Reglat and Tanguy [34] repeated the exact measurements but used a piezo-transducer instead. Piezoelectric transducers are appropriate for measuring dynamic pressures. The sensor was installed on one of the roll's surfaces, and in order to remove the intrusion effects, the mount of the sensor was carefully machined to fit the surface of the roll. The pressure plots showed a region with positive pressure followed by a region with sub-atmospheric pressure. The maximum

pressure increased with the velocity and viscosity, and decreased with the gap size, consistent with the lubrication analysis predictions.

The method to measure the nip pressure was later improved and applied to the deformable roll coating [67] and the coating for complex rheology fluids [68]. Both studies examined the factors (including nip pressure) affecting the misting occurrence (ejection of droplets from the film at the time of separation). Poranen et al. [66] extended the analysis to measure the pressure profiles of the slurry coatings in the nip between an elastic roll and a metal rod. Ascanio and Ruiz [69] elegantly summarized the experimental technique to measure the fluid pressure in the nip, and exposed some of its challenges. The technique includes a high-sensitivity piezoelectric sensor and a slip ring for data collection from the rotating frame. The residence time of the fluid in the nip is very short (of the order of 5 ms); hence, a high-frequency sensor and data conditioner are required. They have shown that the positive pressure from the lubrication theory is in reasonably good agreement with the experiments (a difference of 12.67% in peak pressures). However, owing to cavitation, there is no agreement in regions where the lubrication theory predicts a substantially sub-atmospheric pressure (the sub-atmospheric pressure is overpredicted by a factor of almost 3) [43].

In this study, among these experimental measurements, I take pressure measurements (using a piezoelectric sensor), use a proximity sensor to record the separation of the wheel and rail, and map out the depth of the film of fluid left on the track once the wheel rolls by using laser-induced fluorescence. I also image the bow wave and film splitting at the downstream meniscus using high-speed cameras and a borescope. Identifying the meniscus shape or using PIV/PTV to find the velocity fields is beyond the scope of this research.

Printer's instability

The fluid flow in the nip region is relatively simple and can be considered 1D; however, at the film splitting, the associated two-dimensional flow is known to be prone to instability, which generates a complicated three-dimensional filamentary structure. For our rolling flows, the film splitting is complicated still further by the generation of substantial negative pressures that likely induce cavitation. This classical instability has received a lot of attention in the literature and is referred to as "ribbing/printer's" instability [70]–[72]. Instability occurs above a critical roll speed. Ideally, it is desired to avoid instability as it presents the defects on the final coating product. Thus, the goals of the studies in the literature were to define a space in which the flow is stable, resulting in a uniform-coated layer. Ribbing instability is characterized by the periodic wavy or ribbed pattern of the film in the transverse direction that extends downstream in the axial direction [73]. In the diverging channel, viscous forces tend to increase the pressure gradient in the downstream direction (destabilizing factor), and capillary forces under the curved meniscus tend to stabilize the flow. The competition between these two forces (characterized by Capillary number), and elastic forces in the case of viscoelastic fluids, determine whether the flow is unstable.

One of the early works on film-splitting instability was published by Pearson [72]. He studied the liquid spreading on the plane surface by means of a wedge-shaped spreader and observed the regularly spaced crest and troughs in the emergent film. He then characterized the ribbing pattern using line spacing (wavelength), defined as a number of crests or troughs per unit length. Interestingly, he showed that the wavelength depends very little on the fluid property and velocity. In contrast, the impacts of the gap size and rolls radii are significant (the number of crests increases for the narrower gap sizes). This study was followed by [42], where they defined two main parameters for the instability occurrence: the mean Capillary number ($Ca = \frac{\mu U}{\sigma}$) and the gap

ratio ($G = \frac{h_0}{R}$). In an experimental investigation, they showed that the stability starts to appear when $Ca \sim 62 \frac{h_0}{R}$ or exceeding that ratio.

Ribbing stability was also examined in a theoretical domain using the standard linear stability analysis of free surface flows [71], [74]. As an example, Carvalho and Scriven [71] studied the stability of the flow with respect to infinitesimal three-dimensional disturbances. Numerically solving the eigenvalue problem arising from this analysis, they predicted the critical Capillary number at which smooth film-splitting becomes unstable. In addition, they showed that, despite the widespread belief that the flow between two counter-rotating cylinders is two-dimensional, it is indeed three-dimensional due to the end effects. Results from this theory were in agreement with the experiments. Later on, Carvalho and Scriven [70] interestingly showed that the onset of ribbing could be delayed by using a deformable cover on one of the rolls.

Given the range of Capillary number and gap-to-radius ratio for our lubricated flow under the rolling wheel, the flow is known to be unstable. In fact, experiments show that the deposited film on the surface is filamented, caused by the printer's instability at the meniscus. However, I do not go beyond that to study instability as that will be outside the scope of this study. There is a pool of papers in the literature discussing the instability and conditions in which they may occur. If interested, the reader may additionally review [75]–[81].

1.2.4 Wheel liftoff

Later in this thesis, I demonstrate that in some conditions (lower speeds or higher loads on the wheel), the wheel does not lift off from the rail, and no liquid (within the detection limit of our measurement technique) passes through the gap between the two surfaces. In other words, the wheel remains in solid contact with the underlying substrate. For those conditions, the lubricated

pressure generated in the nip fluid must be insufficient to support the applied load. The lubrication mechanism obviously fails for these cases as theory always predicts the formation of lubrication layer regardless of the magnitude of the applied load. In this section, I aim to describe some of the related observations reported in the literature that resemble the wheel's failure to lift off. Those observations are in the context of the journal bearing and the car's tire hydroplaning.

Almost a century ago, Stribeck interestingly showed that the coefficient of friction in journal bearing is directly related to shaft speed [82]. Referring to Stribeck's curve (a classical curve for journal bearings studies), the coefficient of friction is high at low speeds (metal-to-metal contact or mixed lubrication contact). However, once the speed increases, there is a critical point (known as a liftoff speed) after which the transition to full-film hydrodynamic lubrication occurs, resulting in a significantly lower coefficient of friction. The lubrication pressure in the fluid increases with speed, and at some point, it is sufficient to support the load on the inner shaft. Vogelpohl [83] developed a simple empirical equation to predict the liftoff speed, which was revisited later by different researchers [84], [85]. The prediction of liftoff speed is a complicated problem because liftoff speed is a function of many variables, including surface roughness [86]. Some researchers [87]–[89] relied on the tribology of the surfaces to obtain the liftoff threshold. They suggested that the minimum gap between two surfaces should be exceeding the RMS roughness of both surfaces (multiplied by a constant) so that liftoff can happen, i.e. $h_{min} = \lambda\epsilon$, where λ is a constant and ϵ is the RMS roughness. Once the minimum gap size is known, the lubrication mechanism determines the liftoff speed. In the present thesis, to check the relevance of this observation to the wheel liftoff, I will vary the surface roughness by a factor of 3 and examine whether that alters the liftoff threshold.

Liftoff problem is also relevant to hydroplaning/aquaplaning wheels on cars although the Reynolds number achieved there is quite higher. Hydroplaning is a situation when a layer of water builds between the wheels of the vehicle and the road [90]. There is a critical speed of the car/plane (as a function of tire pressure) above which the resulting pressure in the water, accumulated ahead of the tire, becomes superior to the weight of the car [91]. At those speeds, the water layer lifts the tire, resulting in a loss of traction (similar to the lubricating film in this study). At low speeds, the water has sufficient time to escape the gap under the tire, and therefore the tire contact is maintained. Hydroplaning was similarly solved by utilizing the 2D Reynolds equation [92]. This problem is a difficult one as it involves complicated fluid/structure interaction, producing the need for 3D-CFD. Direct measurement of the fluid pressure in hydroplaning conditions (using a piezoelectric transducer) verified the use of the Reynolds equation to predict the pressure [93].

1.2.5 Non-Newtonian fluids

Nearly all industrially important coating fluids are non-Newtonian, yet little has been published, either experimental or theoretical, to study the coating physics of the non-Newtonian fluids [94]. The levitation problem considered by [16] was also limited to the Newtonian fluids. The reason is, in part, more advanced models are needed to incorporate non-Newtonian behavior (see the review article by [95]). The non-Newtonian fluids show shear-dependent viscosity and often contain polymer additives, hence exhibiting shear-thinning and viscoelasticity. In some cases, the fluids are aqueous suspensions of solid particles with specific binders, making the rheology even more complex. The problem becomes further complicated as the shear rate in lubrication geometry is very high due to narrow gap (of the order of $\dot{\gamma} \sim 10^4 - 10^5\ s^{-1}$), and a knowledge of fluid rheology at those high shear rate is required.

Among the non-Newtonian properties, this study focuses only on the shear-thinning fluids. Elasticity and extensional viscosity significantly impact the flow near the free surfaces and in the inner region; however, elastic forces is believed to make a minor contribution to the load-carrying capacity of the fluid as long as the fluid's relaxation time is small [19]. In the lubrication geometry, the elastic effects may not appear and hence and shear-sensitive viscosity is a dominant factor affecting the global force balance. Most papers in the literature similarly focused on the shear rate dependence of viscosity, and little work has been reported to examine viscoelasticity. Even in their detailed review of the coating fluids, Weinstein and Ruschak [29] did not examine the viscoelastic fluids, citing the lack of broadly acceptable constitutive equations to generalize the results.

In two pioneering works, Coyle et al. [96] and Greener and Middleman [19] theoretically examined the non-Newtonian fluid by adapting a purely viscous power-law fluid. By solving 2D conservation equations, Coyle et al. [96] obtained a relationship between the coating thickness ratio and the roll speed ratio: $\frac{h_1}{h_2} = S^{\frac{n}{n+1}}$, where h is the coating thickness on each surface, S is the speed ratio, and n is the power-law index. This relationship suggests that with increasing the shear-thinning degree (decreasing the power-law index, n), the flow rate through the gap increases due to i9ncreeased mobility of the fluid (conversely, the load-carrying capacity decreases). However, Greener and Middleman [19] reported the exact opposite trend, which was incorrect and later corrected by [97]. Besides, [96] showed that the shear-thinning behavior moves the meniscus further out of the gap and delay the onset of ribbing instability (shear-thinning is stabilizing the flow, similar to surface tension). Film splitting is more symmetric for the shear-thinning fluids than the Newtonian fluids when the rolls rotate at different rates. In Newtonian fluids, typically, the faster roll carries more fluid. For ease of analysis, [96] only dealt with flows in a large Capillary

limit, avoiding the need to define the characteristics viscosity for Capillary number. Hewson and Kapur [98] extended this work to account for surface tension forces. The shear-thinning fluid analysis was later improved and adapted to different geometries, such as blade coating [99] and slot coating [100]. In the limit of weakly non-Newtonian fluids, Ross et al. [99] showed that the shear-thinning fluids may increase or decrease the pressure and the coating thickness, depending on the geometry of the slot/blade.

Elasticity, on the other hand, is a destabilizing factor. Bauman et al. [101] experimentally showed that the onset of instability occurs at much lower speeds once minute amounts of polymers are added to the liquid. Thus, it is more challenging to have a uniformly coated layer with viscoelastic fluids. Elastic stresses that are present in extensional flows near the meniscus contribute to flow instability. The Weissenberg number (the ratio of the elastic force to the viscous force, $We = \frac{\lambda U}{h_0}$, where λ is the fluid relaxation time, U is the substrate speed, and h_0 is the minimum gap) is the dimensionless number that identifies the significance of elasticity. There is a critical Weisenberg number, for each Capillary number, above which the instability appears. Despite the nonlinear viscous models (i.e., power-law fluids), which are possible to model, difficulties may arise as one couples the viscous terms with the elastic terms [102]. The flow must be solved using the constitutive equations. Several attempts have been made to model such a flow exploiting the well-known constitutive models (Oldroyd-B, Giesekus fluids, to name a few), but they are often simplified for algebraic tractability. If the reader wishes to pursue these studies, the reader may review [68], [94], [102]–[105].

As our lubricated flow is different from the coating flow, there is no guarantee that any of the above findings for the shear-thinning fluids apply to our problem in the same fashion. As

mentioned earlier, one clear distinction is that there is a fixed gap in the coating applications, whereas in our problem the surfaces are initially in contact and the lubricated flow may raise the wheel off the track. The distinction may lead to different, but important, features in the behavior of the fluid flow.

1.2.6 Railroad application and carrydown

Here, I expand on the industrial application of this study and provide a summary of the industry-driven researches in the literature. Those researches often focus on the carrydown of the liquid friction modifier- a mechanism by which the liquid is conveyed further along the track. In Chapter 4, I run laboratory and field experiments to study carrydown.

Top-of-rail friction control through application of liquid friction modifiers (LFM) is widely implemented in heavy haul freight railways [7], [9]. In this application, a thin layer of liquid friction modifier (LFM) is applied to the track prior to the passage of the wheel [106]. LFMs change the coefficient of friction between the wheel and rail to a value less than that of pure metal-to-metal contact, but still sufficiently high not to compromise traction and braking. This reduced level of friction significantly reduces wear, curve noise, and the lateral force at the wheel-rail interface in a curve [4], [106]–[110].

Harmon and Lewis [12] have recently conducted a review of top-of-rail (TOR) friction modifiers. They identify a gap in the literature – the lack of a thorough understanding of carrydown. TOR products are usually applied to the track via a trackside application unit. The trackside system is recommended when a long distance of the rail is to be coated with the LFM [12]. When the wheel rolls over the LFM pool, the wet film splits between the wheel and the rail, with some remaining on the rail and some depositing on the wheel. The coated wheel then comes into contact with the rail at the next revolution, where the product is intended to be transferred

back to the rail. LFMs can be water-based, oil-based, or hybrid (mixed). The water phase of LFMs has been shown to vaporize quicker in the wheel-rail contact (high-temperature zone) [10], changing the carrydown performance.

One device that I used to study carrydown in a laboratory is the twin-disc machine. Gutsulyak et al.[111] outlines the test protocol and instrument discussion for this machine. In this machine, the product was applied to the interface between two counter-rotating metal discs with an applied normal force, and the friction coefficient between the discs was measured as a function of the number of disc rotations. The variation in friction coefficient (specifically, how long the coefficient remains below that of bare metal-to-metal contact) was then used to identify the carrydown distance. A friction modifying effect was observed even 1000 rotations after application of the LFM to the twin discs. 1000 rotations approximately correspond to ~3 km travel of the train with minimal slip between wheel and rail (assuming a wheel diameter of 1 m). However, twin disc machines had a dramatically smaller size than a full-scale train wheel. In addition, LFM on one disc interacted with a surface that has already been in contact with LFM, in contrast with LFM application in the field, for which LFM adhering to the first wheel interacts with the bare metal rail downstream of the application site [11]. Stanlake [112] studied the initial stage of carrydown, using an apparatus that consists of a ramp and a steel roller. The roller was released from a certain height and rolled over a patch of wet friction modifier at the base of the ramp. The mass of the liquid transferred to the roller was measured and it was shown that a small change in the product formulation could lead to a drastic change in the amount of film transferred during film splitting.

Initial pick-up and carrydown are further discussed in [113]–[115], chiefly in a laboratory setting. In particular, Harmon and Lewis [113] studied the impacts of different variables such as

slip, load and speed on pick-up. They also proposed a simpler method to rank different FMs in terms of the initial pick up, with a similar performance as to expensive large-scale tests.

Carrydown has also been studied in the field. Chiddick et al. [116] showed that the lateral force on the rail is reduced by 35% (with a decrease in wear and rolling contact fatigue) almost 2 miles downstream of a trackside LFM dispensing unit. Manufactures often rely on the friction measurement to confirm the LFM presence. That is the lower friction level is an indication of product presence. However, some researchers [2], [117] questioned the accuracy of the handheld tribometer measurements as the friction level is also a strong function of the weather conditions and rail contamination. Khan et al. [118] directly studied LFM coverage on the wheel and the rail. They used cotton swabs to collect samples from the wheel and the rail surfaces at various distances downstream. The samples were subsequently analyzed using the energy dispersive X-ray (EDX) method, searching for LFM elements such as molybdenum (Mo) and Magnesium (Mg). Those researchers were unable to detect LFM on the rail more than ~100 m from the application site. In addition, they showed that the product could not support the high contact pressure at the wheel-rail interface and that it is pressed out of the contact band, limiting the carrydown distance. In an experimental trial, Eadie et al. [119] showed there is an optimal amount for the LFM pool, beyond which increasing the initial pool volume barely changes the carrydown distance.

Although these studies give insight into some aspects of carrydown, other aspects of carrydown are not fully understood. For instance, we do not have a complete understanding of the mechanism by which the LFM functions at the wheel-rail interface and transfers down the track. The impacts of the LFM rheological properties on carrydown is another open question that requires further attention. This information is particularly important for LFM manufacturers. Additional information is also needed to optimize the unit spacing and the application rate of the wayside

systems. It would be also interesting to see the spatial distribution of the deposited LFM on the track after passage of the train. Certainly, this is not possible when samples are collected from the track surface, as was done by previous researchers. Motivated by these gaps in the literature, this research aims to enhance our understanding of the carrydown mechanism.

1.3 Thesis outline

This thesis primarily concerns the experimental and analytical study of the lubricated rolling over a pool of liquid, applicable to the railroad industry. This problem has not been thoroughly investigated at the wheel-rail interface. However, some relevant information can be drawn from analogous studies of the coating process in the paper industry. Having said that, there is a clear distinction between the coating flow (in which there is a fixed gap between two surfaces) and our lubricated flow (in which two surfaces are initially in contact). This distinction leads to different, but important, features in the fluid flow. To explore the fluid dynamics of rolling over a liquid pool and the “carry-down" by subsequent revolutions of the contaminated wheel, I conduct an idealized laboratory experiment in Chapter 2 for Newtonian fluids and in Chapter 3 for non-Newtonian fluids. The experiments include simultaneous measurements of the load, coated film thickness, instantaneous gap size between the wheel and the rail, and the fluid pressure. The complementary lubrication-based model is also provided for those chapters. Chapter 5 discusses the industrial application of this research in which I outline some field experiments. The thesis is structured as follows:

In Chapter 2, I explore the problem for a Newtonian pool (silicone oil and water-glycerin solutions). The speed, width and loading of the cylinder are varied as are the initial depth and

length of the viscous pool. I experimentally show that, depending on the operating conditions, two outcomes are possible: either the cylinder will ride on a lubrication film or remain in solid contact with the underlying substrate. For the former situation, a lubrication theory is provided which successfully predicts the pressure underneath the cylinder, the gap size, and the thickness of the coating film. I also discuss some other features of this lubricated flow that was observed experimentally. This chapter aims to provide baseline understanding of our lubricated flow with a simple Newtonian fluid.

In Chapter 3, I extend the experimental and theoretical analyses to the non-Newtonian fluids as many industrial fluids are non-Newtonian. The study is limited to shear-thinning fluids. Mixtures of glycerin and xanthan gum at two low concentrations are used as inelastic shear-thinning fluids. Similar to Chapter 2, first I conduct experiments to investigate the effects of the loading, speed and fluid's rheology on the lubricated flow. Then, I also provide a complimentary lubrication-based model for the shear-thinning fluids and compare the predications and the measurements.

Chapter 4 attempts to evaluate the industrial application of this research. First, I conduct idealized laboratory experiments for the conditions which closely resemble those at the wheel-rail interface. Then, I perform field experiments on an operating track and draw parallels between the laboratory studies and the field trials. Test fluid is a commercial water-based liquid friction modifier (KELTRACK®) which shows shear-thinning behavior. Laser-induced fluorescence served to measure the LFM thickness left on the track after the passage of the wheel. Some interesting observations were made, from both lab and field experiments, which are detailed in this chapter.

Chapter 5 provides a summary of the major findings of this thesis, including the limitations of the study, and provides suggestions for future work.

Chapter 2: Lubricated Rolling Over a Newtonian Pool

2.1 Introduction

In this chapter, the interaction of a rolling cylinder or wheel with a pool of liquid resting on a substrate (Figure 2-1) is studied. This process is relevant to many practical problems such as roll coating, lubrication of bearings, and rail transport. First, an idealized laboratory experiments are conducted on a custom rig (Section 2.2). The experiments include measurement of the coating thickness, the instantaneous gap size between the cylinder and the substrate, fluid pressure, and visualization of the flow-field. The key results are presented in Section 2.3. The complementary theoretical model is derived and compared against the experimental results in Section 2.4. Comparison of the model predictions and experiments (Section 2.5) both validates aspects of the model and exposes its limitations. I conclude in Section 2.6 with a discussion of key findings. Supplementary results for this chapter are presented in Appendix A.

2.2 Materials and methods

2.2.1 Experimental apparatus

Figure 2-2 shows the experimental apparatus used in this study. The apparatus consists of a highly modified woodworking band-saw, chosen because the band-saw provides a long and continuous moving flat surface. The original band-saw is modified to incorporate various wheels, motors, pneumatic air cylinders, and sensors to model the rolling mechanism and collect experimental data.

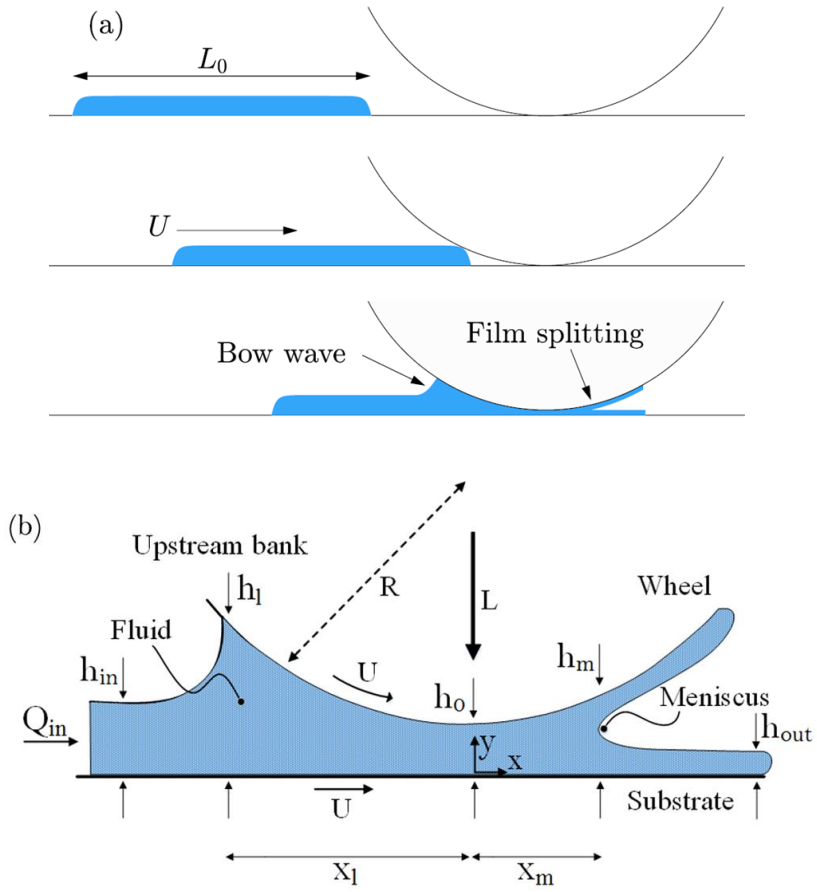

Figure 2-1 Sketches of the geometry for lubricated rolling over a viscous fluid layer, showing (a) the wheel rolling into the initial pool, and (b) the details of the lubrication film, with various physical parameters indicated. h_{out} is the coated film thickness left behind after passage of the wheel.

The wheels were machined from mild steel and had radii of $R = 10$ cm; four different widths of $W = 2$ mm, 5 mm, 10 mm and 20 mm were used. The wheels were loaded by means of pneumatic air cylinders that were controlled by fast-acting solenoid valves. Two magnetic Hall effect sensors, with a 15 kHz sampling rate, measured the speed U of the blade and wheel. A 2 kN load cell measured the normal force at the wheel-rail contact patch. The backing wheel was not driven and prevented any deflection of the blade under the applied normal load. Both wheels were mounted on a linear rail guide to ensure smooth and accurate activation. The parallelism of the wheel axle

and the blade surface was verified by placing pressure-sensitive papers (Fujifilm Prescale HHS PS) between the wheel and the dry blade and observing the uniformity of the pressure distribution across the wheel width. To reduce the light reflection from the surface of the band saw blade (which is a requirement for the film thickness measurement technique, described next), the blade was chemically treated with black oxide (magnetite). It should be noted that the geometries of the wheel and blade in this apparatus are different than those in operating trains, and one needs to be very cautious when translating these results to the real application. In addition, Chapters 2 and 3 concern the fundamental studies of lubricated fluid between two surfaces moving at the same speed (i.e. no slip). Also, the applied load in this chapter are significantly milder than real application.

The flow visualization was challenging because of the limited optical access to the nip, the small-scale flow, and the very short residence time of the fluid in the nip (of the order of 20 $\boldsymbol{ms}$). A high-speed camera (Phantom V.12, with a resolution of 512×512 pixels, and frame rates of 2000-5000 fps) was used to image the nip from the side. The flow was backlit with a LED light source (6700 Lumen). A side view is clearest to image fluid flow upstream of the nip. To observe the downstream meniscus, I used a 90-degree, 4 mm-diameter rigid borescope (MEDIT 9430E) coupled to a camera with illumination provided by two fiber optic lights (MO150-JH Technologies and MidoriTM-35 Watt).

To measure the instantaneous gap size between the wheel and the blade, a laser-based proximity sensor (Baumer OM20-P0026.HH.YIN), with a sampling rate of 5 kHz and an accuracy of 1 μm, was mounted on the bed of the experimental apparatus. The sensor measured the distance to the wheel axle (shown in Figure 2-2).

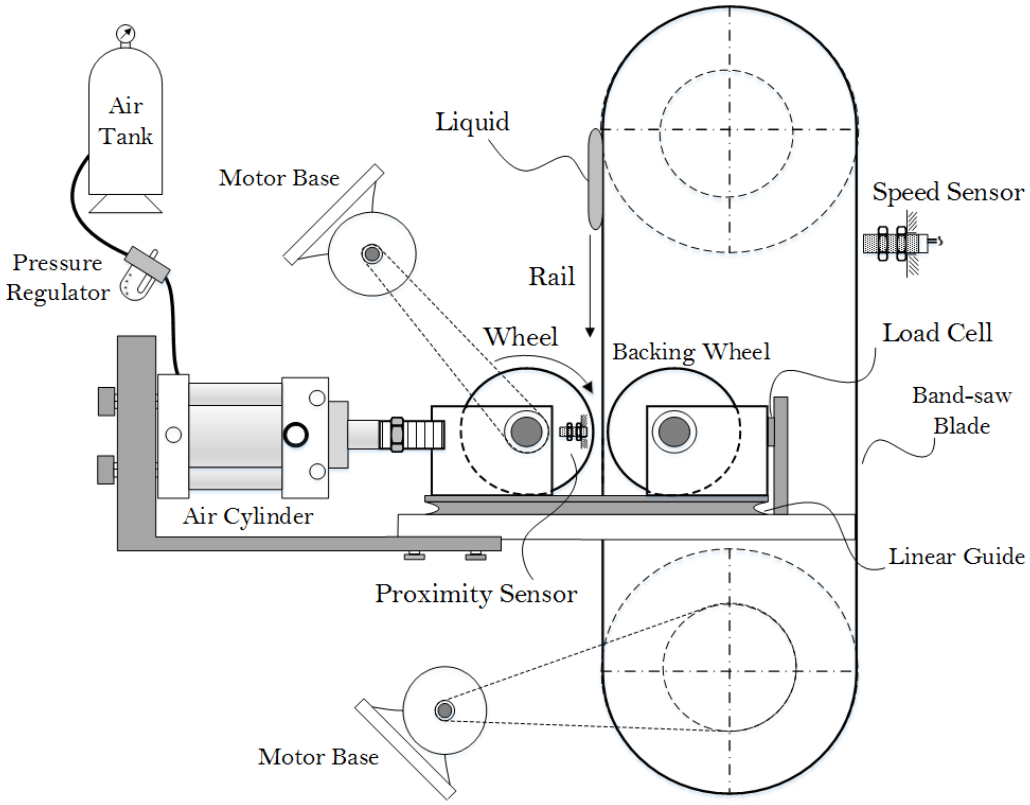

Figure 2-2 Schematic of the experimental apparatus, showing the wheel-rail interaction. The wheel represents the train wheel and the blade represents the rail. The backing wheel provides support to prevent the deflection of the band saw blade under a large normal load. The load is applied through an air cylinder and various components measure the speeds and force. The schematic is not to scale.

At the start of each experiment, a pool of liquid with a known thickness and length was applied to the blade. The initial pool was wider than the wheel width and covered the entire blade section ($\sim 6\ cm$). The test liquid was either water-glycerin solution or silicone oil. The water-glycerin solutions had dynamical viscosities of $\mu = 0.73 - 1.19\ Pa \cdot s$, density $\rho = 1210\ kg\ m^{-3}$, a fluid-air surface tension of $\gamma = 60\ mN\ m^{-1}$, and a contact angle of $\theta_c = 62 \pm 4°$ on the treated band-saw blade (as measured by shadowgraphy, see Section 2.2.3). The silicone oil was characterized by $\mu = 8.72\ Pa \cdot s$, $\rho = 950\ kg\ m^{-3}$, $\gamma = 21\ mN\ m^{-1}$ and $\theta_c = 16 \pm 3°$.

To initiate the experiment, the speeds of the wheel and the blade, and the pneumatic cylinders operating pressure, were set. Once a photo diode sensor detects a marker on the blade, the pneumatic cylinders were activated, driving the wheel into contact with the blade upstream of the pool of liquid. The wheel then rolls over the liquid pool and picks up some of the liquid as it passes. One circumference downstream from the original pool, the liquid adhering to the wheel returns to the nip between the wheel and the blade, and the process repeats. The large length of the blade allowed six wheel-rail interactions before the wheel again approaches the initial pool location. During the course of the experiments, the gap between the wheel and the blade, the fluid pressure, and the applied load were recorded. Once the experiment was complete, laser-induced fluorescence (LIF) of the deposited liquid was used to measure the film thickness left behind on the blade. Details of the LIF technique are provided in Section 2.2.3.

Experiments were carried out to study the effects of speed U, load L,and viscosity μ on the rolling process. The wheel-blade speeds U were varied between $0.2 - 8 \sim ms^{-1}$ and four different load-to-width ratios ($L/W = 11.2, 17.1, 38.8, 76.3\ \ kNm^{-1}$) were used.

2.2.2 Pressure measurement system

Figure 2-3 shows the pressure measurement system, including the general view and the schematic of the pressure transducer mounting. Pockets were machined in each quadrant of the largest (20 mm width) wheel to accommodate a small-scale piezoelectric gauge pressure transducer (Kistler, type 603CBA01000). The sensor has a rise time less than $0.4\ \mu s$, a natural frequency exceeding 500 kHz, and a pressure range up to 1000 bar.

The sensor area of the transducer (5.55 mm in diameter) was too large to provide adequate resolution of the lateral pressure distribution on the wheel. To measure the lateral pressure

distribution, 4 custom pressure taps, each 1 mm in diameter, were press-fit into the wheel and the pressure transducer was connected to each tap in turn. The centers of the pressure taps were located at z=0, 2.5, 5, 7.5 mm, where z=0 mm corresponds to the wheel centerline and z=10 mm corresponds to the outside edge of the wheel. After placement into the wheel, the pressure taps were carefully machined flush with the surface. All the cavities, from the tapping area to the sensing tip, were filled with vacuum grease. A slip ring (SparkFun Electronics, ROB-13063) was used to transfer the electronic signal generated by the rotating pressure transducer from the rotating wheel to the laboratory frame of reference. The slip ring was attached to the end of the shaft using a custom-made adapter. The sensor cables were routed through the keyway of the shaft and then connected to the slip ring.

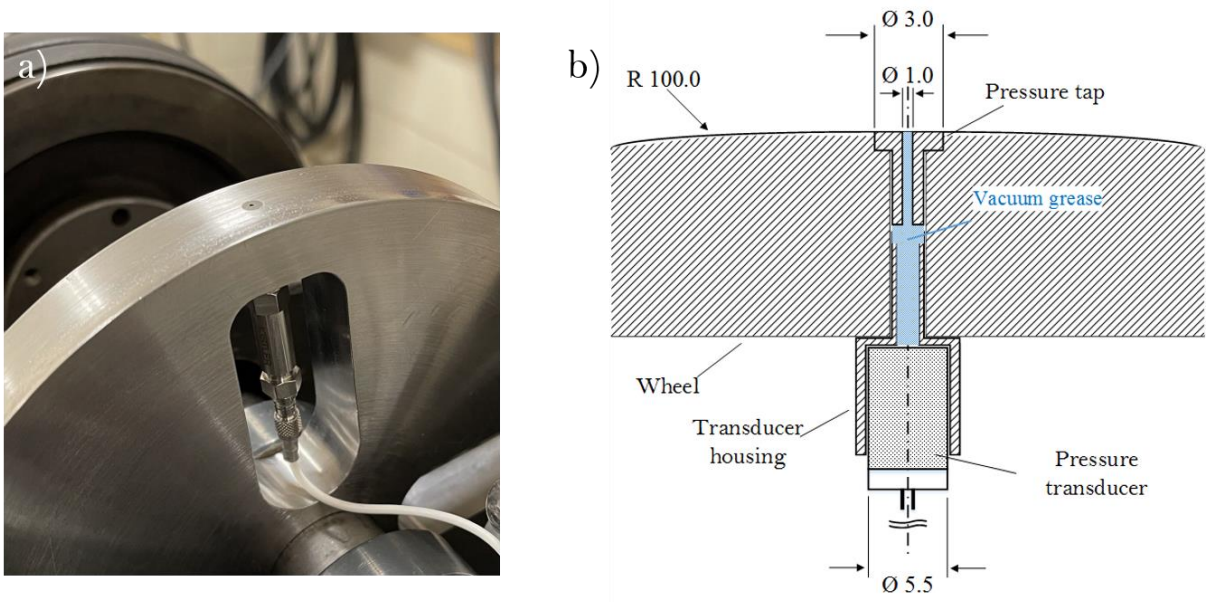

Figure 2-3 (a) General view of the wheel and centerline pressure port, (b) mounting of the pressure transducer and the pressure tap (dimensions in mm). The schematic is not to scale.

The pressure transducer was independently calibrated and the manufacture's calibration was verified. To further validate it, the pressure measurements are compared against the load cell

readings in Figure 2-4 at three applied loads. As discussed later, the trapezoidal rule was used to integrate the pressure over the four pressure ports. This method commonly underpredicts the area (given the lateral pressure distribution that is presented later), and that could well explain the 2% underprediction (on average) by the integrated pressure in Figure 2-4.

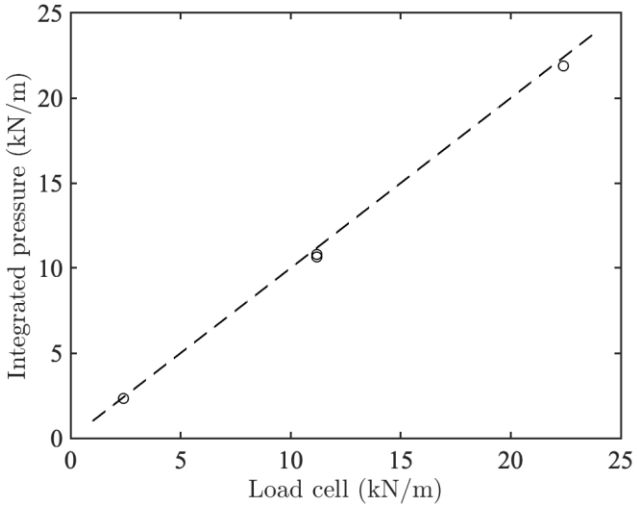

Figure 2-4 Integrated pressures compared to the load cell

2.2.3 Optical technique

The thickness of the film on the blade after the passage of the wheel is on the order 100 μm or less. To measure the spatial distribution of the film thickness with sufficient resolution, trace amounts of a fluorescent dye (Rhodamine-B) were added to the liquid pool. Several rheological experiments confirmed that the minute amount of dye (0.04% by mass) added to the liquid does not change the fluid viscosity. Upon calibration, laser-induced fluorescence (LIF) of the dyed liquid yields the film thickness.

The optical setup is shown in Figure 2-5(a). A 1000 mW diode-pumped solid-state green laser (532 nm) was spatially expanded prior to passing through an optical filter-cube (Nikon 67007 gold-spectrum filter cube set, dichroic filter cut-off: 552 nm, excitation range: 530-554 nm, emission range: 570-613 nm). The light was then directed onto the liquid, causing fluorescence of the Rhodamine-B dye. The light emitted by the dye passed back through the filter cube and was collected by an intensified CCD camera (FLIR Blackfly S3 camera). A two-dimensional map of the film thicknesses is generated based on the fluorescence signal.

Figure 2-5(b) shows a typical calibration curve for the LIF setup. For this case, the LIF signal is linearly proportional to the film thickness for thicknesses below $200\ \mu m$. At larger film thicknesses (not shown), the intensity asymptotically approaches a maximum value. The typical error, and also the smallest thickness measurable, using the current setup is $2.3\ \mu m$.

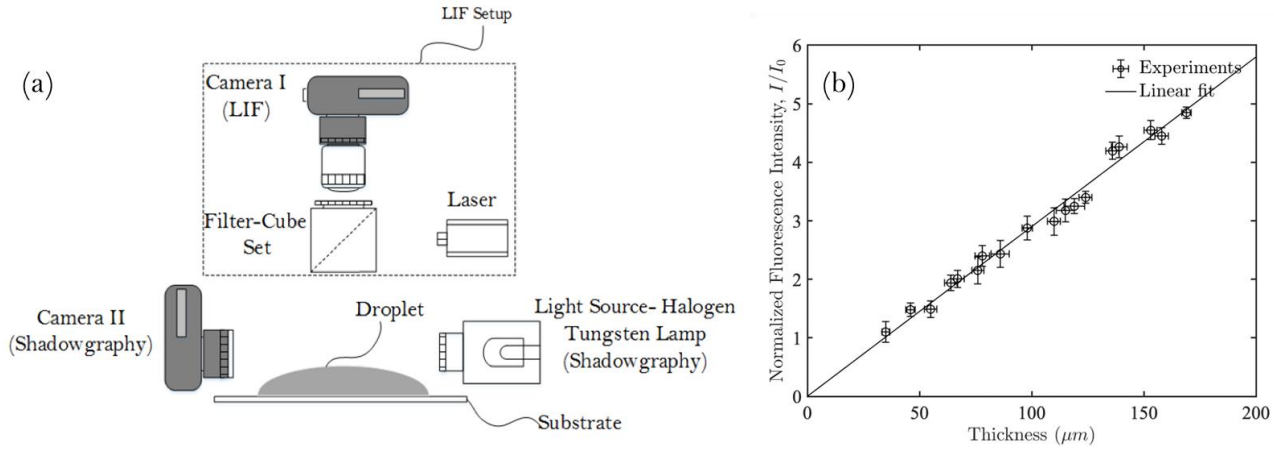

Figure 2-5 (a) Laser-induced fluorescence and shadowgraphy measurements of the droplet geometry. (b) Typical calibration curve (glycerin-water liquid). The normalized LIF signal is a linear function (R^2=0.968) of the film thickness

It is conventional to calibrate LIF signals with measurements of liquid layers of known thickness. However, producing samples of liquid layers with exact micrometer-scale thicknesses, varying from 0 to $200\ \mu m$, is difficult. Several attempts were made to prepare samples by placing

a metal shim with known thickness between two glass slides and filling the gap with the liquid. However, those attempts failed because they often generated large measurement errors. In addition, this approach applies to a condition where the liquid surface curvature is negligible; whereas, the deposited liquids on the track have high curvature. The surface curvature could impact the measured LIF signal owing to refraction effects. Instead, I chose to calibrate the LIF signal using the shadowgraph images of droplets to infer their geometry.

A capillary glass tube was used to generate droplets of different sizes, with peak heights ranging from 30 to 180 μm. Droplets were deposited on the surface, and the droplet thickness distribution was measured by shadowgraphy with an uncertainty of 2.3 μm. Simultaneously, the fluorescence signal was measured with LIF. Once two interface profiles were obtained via LIF and shadowgraphy, a single fitting parameter was used to correlate the LIF signal with the liquid thickness (Figure 2-6(c)). To investigate the effects of the surface wettability, tests were also carried out on surfaces with different contact angles. It was observed that even on a surface with high contact angle, LIF and shadowgraphy were in good agreement. Although one cross-section of the droplet from shadowgraphy is shown in Figure 2-6(a), other cross-sections were also imaged by mounting the droplet on a rotary stage. The calibration curve (shown in Figure 2-5(b)) shows the normalized fluorescence intensity versus liquid thickness, measured for 18 droplets. The calibration, as discussed, is highly linear ($R^2 = 0.986$).

The LIF calibration was also validated against gravimetric measurements (Figure 2-6(d)). As the density of the liquid droplet is known, and its volume can be inferred from the LIF imaging, its mass can be calculated. The comparison of the droplets' LIF-inferred mass with the direct measurement of mass yielded excellent agreement with an RMS error of 6.1%.

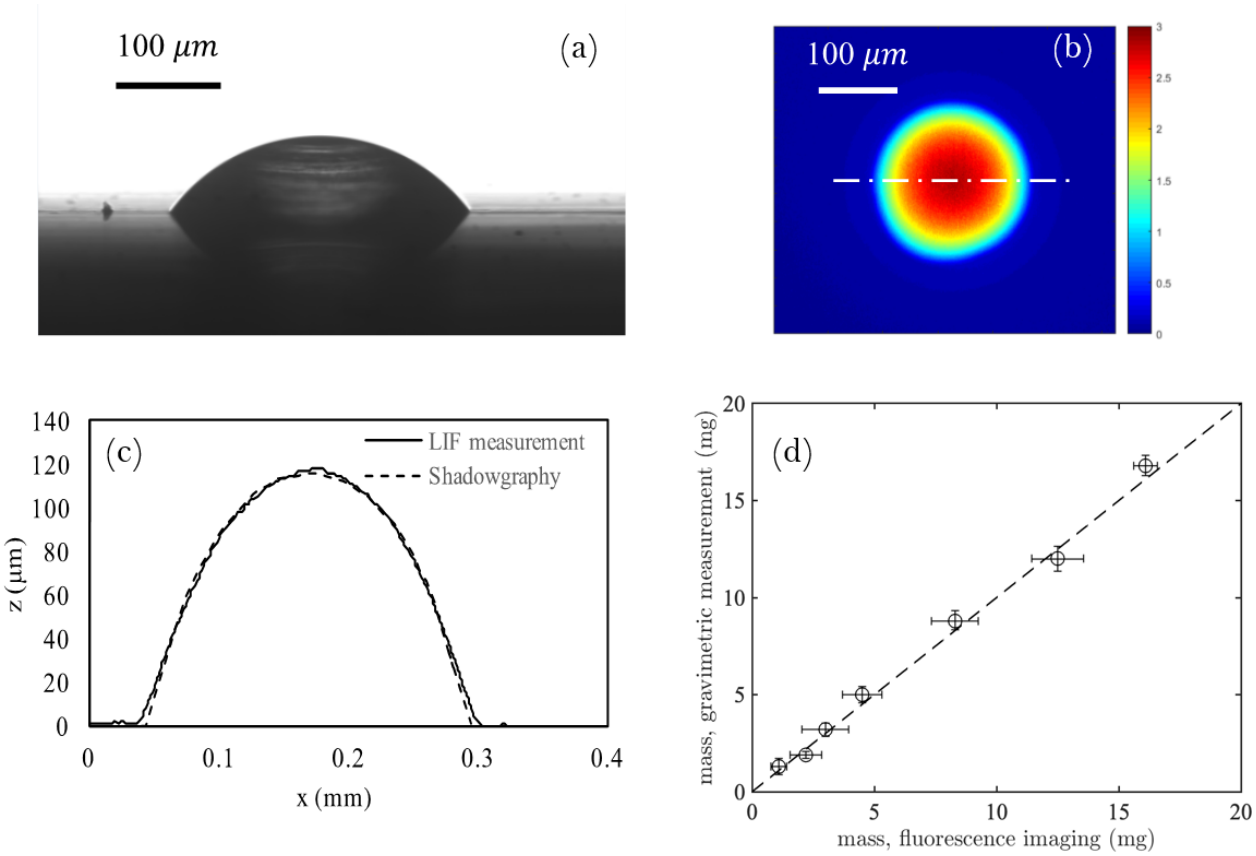

Figure 2-6 a) One cross-section of droplet profile from shadowgraphy, b) normalized LIF signal for the same droplet, c) matched profile. The y-axis scale is greatly exaggerated for graph clarity. d) Validation of fluorescence imaging technique. The RMS difference between the fluorescence-imaging-inferred mass and the directly measured mass is 6.1%.

2.3 Results

2.3.1 Interaction One

I refer to the passage of the wheel through the initial pool as Interaction One; Interactions Two and more refer to carry-down, where the liquid present on the wheel (from Interaction One) is subsequently transferred from the wheel back to the blade. The image on the left of Figure 2-7(a) shows a typical example of the measured film on the band saw blade after Interaction One, and

illustrates several aspects of the fluid mechanics of the lubricated rolling process. First, the finite depth of the film above the band on the track over which the wheel rolled highlights how the cylinder is lifted off that surface by the fluid pressure; the corresponding displacement recorded by the proximity sensor is shown in Figure 2-8. The lubrication film extends both in front of the original pool, demonstrating how liquid is plowed ahead of the rolling wheel, and also slightly behind it (a feature that is barely visible in Figure 2-7(a), but more evident in other examples). The backward advance of the fluid edge results from the finite depth of the initial pool: contact between the wheel and fluid takes place before the location where the wheel touches the rail, and fluid is then pushed backwards into the small intervening gap (*cf* Figure 2-1(a)).

In addition to the forward ploughing, liquid is also squeezed out to the side from the gap between the wheel and rail. This "side flux" (the lateral spreading of liquid out of the nip caused by the high lubrication pressure) creates the two thin stripes bordering the ploughed-ahead film. Note that the initial pool is too deep for the side flux to be detected where the wheel rolls over the original pool, with the signal saturating there (red regions in Figure 2-7).

Although the fluid-filled gap between the rail and wheel is constant across the width, the deposited film thickness forms a distinctive pattern. Indeed, as mentioned earlier, when a film of fluid passes through a narrow gap and splits at the meniscus, the film-splitting flow is prone to the printer's instability [42], [71], [72]. For the typical Capillary number $Ca = \mu U/\gamma$ and ratio of minimum gap h_0 to wheel radius R encountered in our experiments ($\frac{h_0}{R} \sim 0.001$), the splitting flow is expected to be unstable [72]. The instability leads to a filamentation of the fluid film deposited on the track and wheel, as seen in Figure 2-7(a), for the silicone oil. For the glycerin experiment shown on the left of Figure 2-7(c) the interaction process is similar, with the film filamenting as it

splits. This time, however, the glycerin filaments subsequently break and bead up on the blade surface, due to the higher surface tension and contact angle.

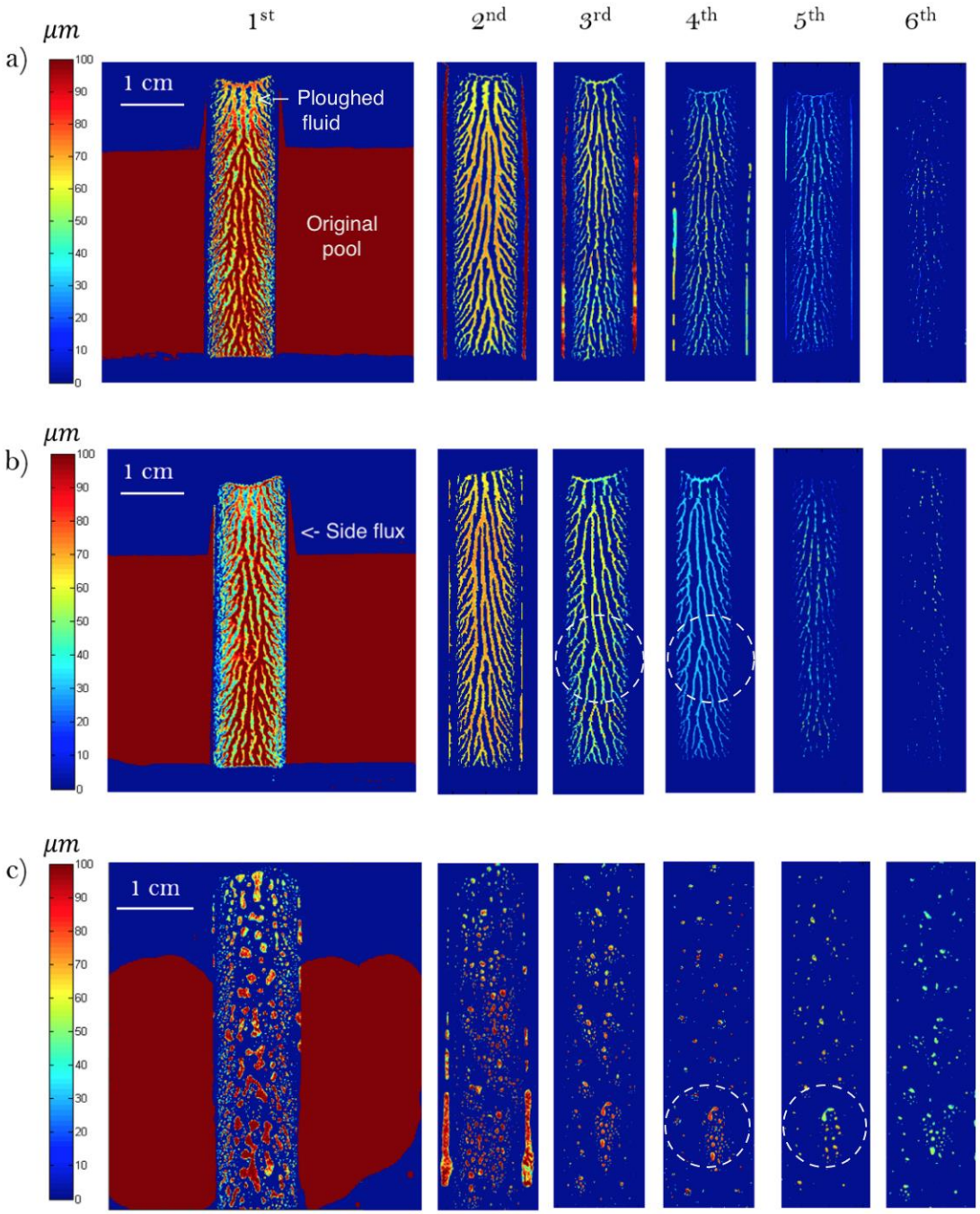

Figure 2-7 Deposited film thickness of six interactions for (a,b) silicone oil and (c) glycerin. The track is moving from top to bottom (equivalent to the wheel moving from bottom to top over a stationary track). Shown is a

color map of the liquid thickness in µm (the original pool is very deep, which causes the LIF signal to saturate in places). In (a), the wheel edge is not cleaned after first interaction; in (b) and (c), the wheel is cleaned. The dashed circles highlight sectors of the film over which the thickness pattern is reproduced during an interaction. Test conditions: U=1 m/s, L/W=11.2 kN/m, L_0=4 cm, h_{in}=500 µm, and W=10 mm.

From the perspective of the lubrication dynamics of the rolling wheel, the patterning of the deposited films by the printer's instability is a distraction that can be eliminated by averaging the film thickness over an area exceeding the typical length scale of the filamentary structure. Such average film thicknesses for the first interaction are plotted against distance down the track in Figure 2-8 and is compared with the proximity sensor measurements tracking the wheel position. For these examples, the film thickness is averaged laterally across the path of the wheel, and over sliding windows of length 0.25 cm in the direction of motion. Just after the wheel makes contact with the pool, the film thickness rises rapidly, then remains constant for a distance l_c (region II). The fluid ploughed ahead of the wheel supports the wheel for a further distance of l_p (region III), over which the film thickness first decreases slowly before diminishing abruptly (region IV). Normally, the ploughed fluid reaches the end of the pool at location $L_0 - x_l$ relative to the start of the pool, ignoring the small backward motion of the fluid as the wheel initially hits it. Therefore, one might expect l_c to be on the order of $L_0 - x_l$, whereas it is slightly longer in the experiments (on the order of the original pool length). Likely, the reason is fluid pressure on or near x_l is very close to the atmospheric value and has a minor contribution to the fluid net pressure. The pressure around x_l becomes more significant once the bow wave has sufficiently receded towards the minimum gap whereupon the wheel starts to move down.

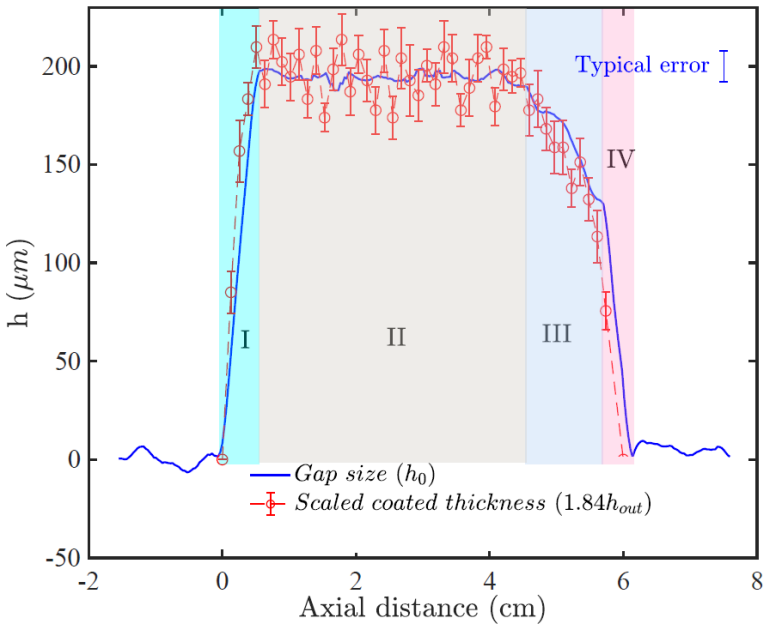

Figure 2-8 The gap h_0 between the wheel and track as measured by the proximity sensor. Also shown is the scaled thickness of the deposited fluid film on the track. Test conditions: U=1 m/s, L/W=11.2 kN/m, μ=8.72 Pa·s (silicone oil), L_0=4 cm, h_{in}=500 μm, and W=10 mm. The typical error bar of the gap measurement corresponds to the standard deviation of three experiments run under identical conditions.

The average film thickness, when scaled by a suitable constant factor (of 1.84), closely tracks the wheel displacement. Thus, the take-off of the wheel from the deposited film does not substantially redistribute the fluid other than by creating the pattern of filaments, and the average film thickness consequently reflects primarily the wheel position. That said, however, some lateral redistribution of fluid does occur near the sides of the wheel, as illustrated in Figure 2-10, which shows results for different wheel widths (the contour plots of the deposited film are also provided in Appendix A.). In these tests, the ratio L/W is held fixed, which would imply similar lubrication dynamics in the absence of side flux. However, the amount of side flux varies with the wheel width, which modifies the volume of fluid ploughed forwards and adjusts the minimum gap h_0

(panel (b)). The final take-off of the wheel from the film also introduces a distinctive decrease in film thickness towards the sides (panel (c)).

Figure 2-9(a) displays the minimum gap observed for pools with different initial pool length L_0. In agreement with Figure 2-8, the steady gap is established after the wheel has run about 6 mm into the pool. For these test conditions, initial pools with $L_0 \lesssim 6$ mm cannot therefore reach steady state, as observed for the shortest two pools in Figure 2-9(a). For $L_0 \gtrsim 6$ mm, a steady state is attained over a distance l_c depending on L_0, and the steady minimum gap h_0 and final ploughing length l_p then become independent of pool length. For the remainder of this study, I consider pools that are significantly longer (typically $L_0 = 4$ cm) than the distance over which the wheel lifts up to ensure that the steady-state is achieved.

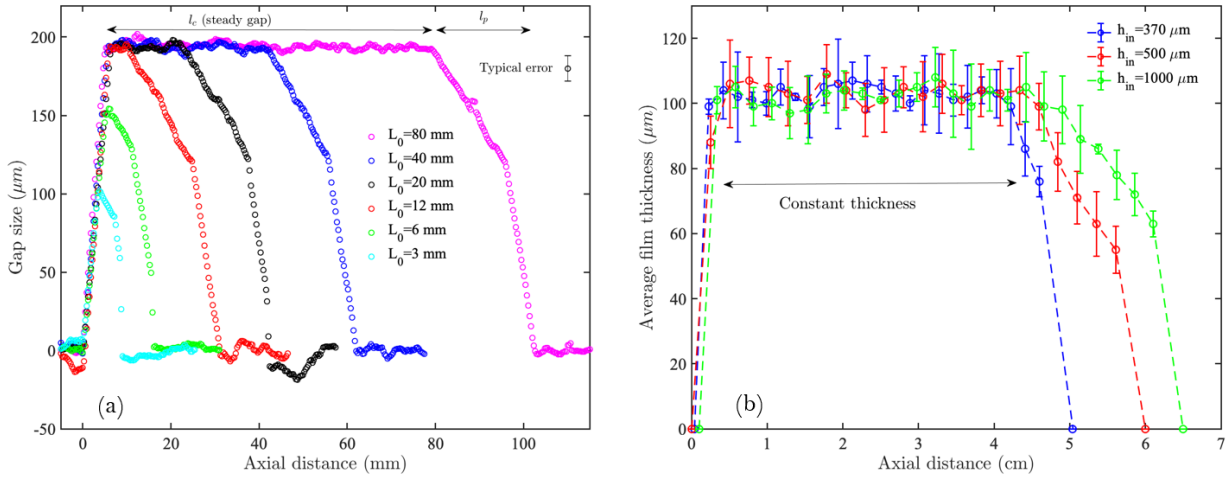

Figure 2-9 a) Gap size measurements for Interaction One versus the axial distance for different pool lengths when pool depth is constant , h_{in}=500 µm, b) film thickness for Interaction One, averaged laterally, versus the axial distance for different pool depths when pool length is constant, L_0=4 cm. The gaps size (or equivalently film thickness) is constant over a distance L_c, and then declines over a "ploughing length" L_p. Test conditions: U=1 m/s, L/W=11.2 kN/m, µ=8.72 Pa·s (silicone oil), h_{in}=500 µm, and W=10 mm. Error bars correspond to one standard deviation of the data with three repeats.

Figure 2-9(b) shows averaged film thicknesses for pools with different depth h_{in}. The constant film thickness over l_c is, to within experimental error, independent of the initial pool depth h_{in} but depends on wheel speed, loading and width. The ploughing length l_p, however, increases with the pool depth due to increased volume of ploughing ahead of the wheel.

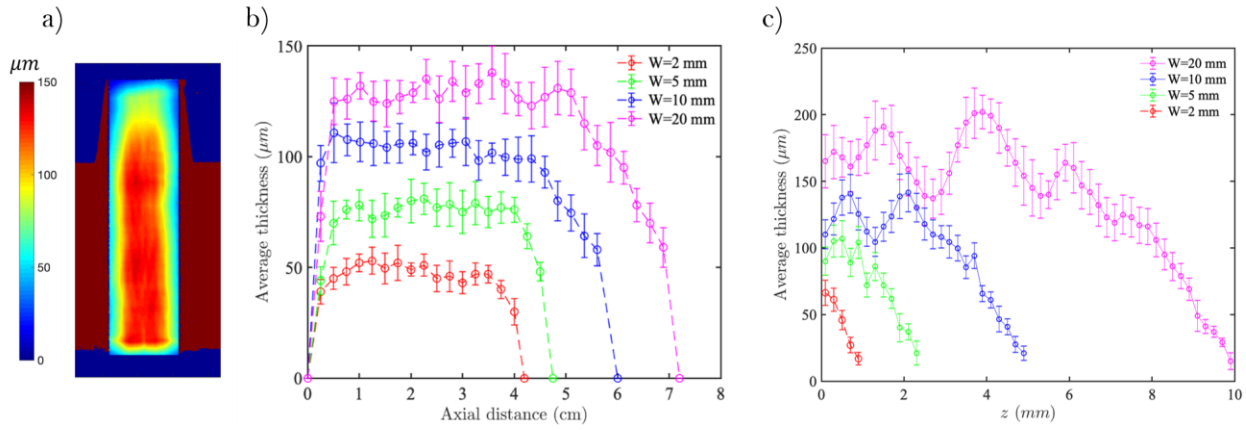

Figure 2-10 Variation of film thickness from Interaction One for different wheel widths. In (a) we show the thickness distribution calculated by averaging the LIF measurements over 2 mm square windows to eliminate the filament pattern resulting from the printer's instability, for W=10 mm. In (b), we plot film thickness averaged laterally over the path of the wheel against distance along the track for four wheel widths. For (c), the film thickness is first averaged over the strip of length L_c, and then averaged laterally over running windows of length 0.2 mm. Test conditions: U=1 m/s, L/W=11.2 kN/m, μ=8.72 Pa·s, L_0=4 cm, and h_{in}=500 μm. Error bars correspond to one standard deviation of the data with three repeats.

Observations of the bow wave and downstream meniscus during the first interaction are shown in Figure 2-11 and Figure 2-12. The two side views in Figure 2-11 show the bow wave during and at the end of the passage through the initial pool. The bow wave forms a steep planar face lying some distance ahead of the minimum gap (Figure 2-11(a)). Once the bow wave reaches the end of the pool, the side profile changes and the position recedes to the minimum gap Figure

2-12(b)). Measurements of the bow wave position as a function of time show that x_l generally follows the trend of gap size shown in Figure 2-9(a): $|x_l|$ increases quickly initially as fluid rapidly accumulates ahead of the wheel, generating the lift force that raises the wheel until the incoming flux matches that underneath the wheel. Over the ensuing steady state, $|x_l|$ remains roughly constant, before falling in the same fashion as h_0 once the wheel reaches the end of the pool.

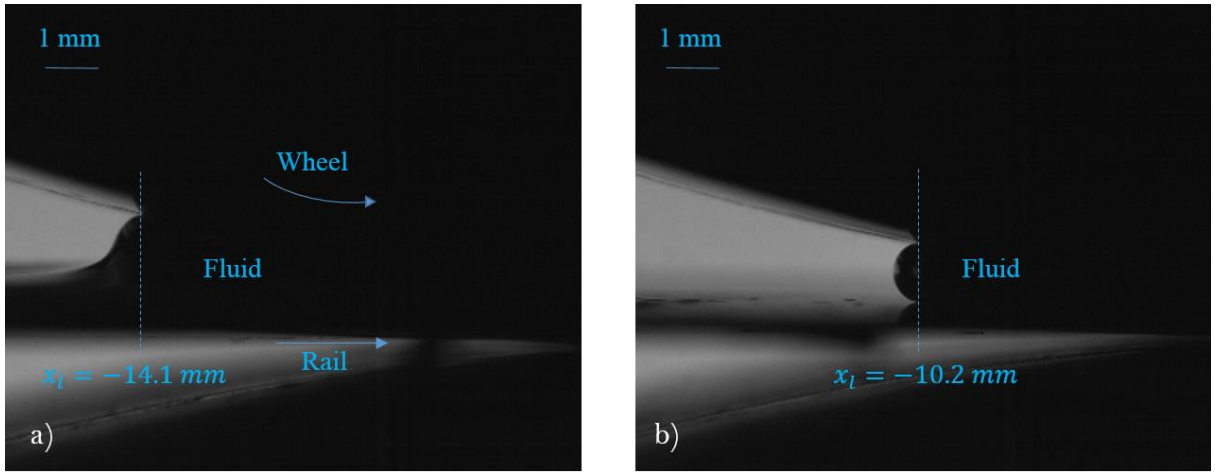

Figure 2-11 High-speed images of the upstream fluid-air interface when the wheel is (a) midway through, and (b) beyond the initial pool. Also indicated is the position x_l, relative to the minimum gap, where the bow wave leaves the wheel. Test conditions: U=1 m/s, L/W=11.2 kN/m, μ=8.72 Pa·s (silicone oil), h_{in}=500 μm, and W=10 mm.

The images from borescope clearly reveal the filamentation produced by the printer's instability at the downstream meniscus (Figure 2-12); the typical distance between fluid filaments in the image matches that inferred from film thickness measurements (see below), to within 10%.

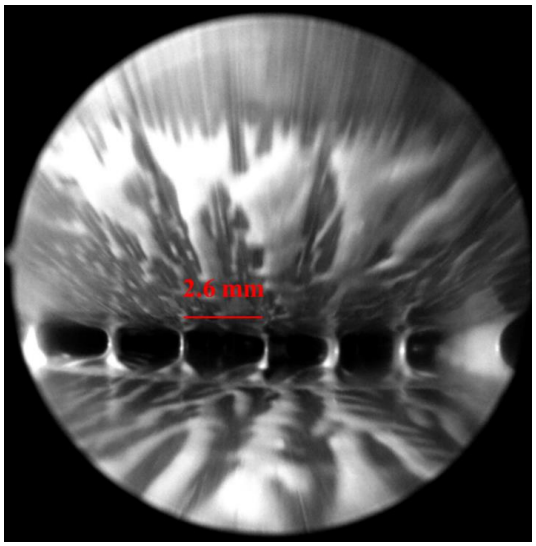

Figure 2-12 Borescope image of the film-splitting meniscus, showing the formation, elongation, and break-up of the fluid filaments in the lateral direction. Also visible is the filamented pattern in the deposited films. The top surface is the rotating wheel and the bottom surface is the moving rail. The borescope was positioned approximately 3 cm downstream the minimum gap location. Test conditions: U=1 m/s, L/W=11.2 kN/m, μ=8.72 Pa·s (silicone oil), h_{in}=500 μm, and W=20 mm.

Pressure measurements during the first interaction are shown in Figure 2-13. Substantial lubrication pressures are encountered as fluid moves towards the minimum gap; just beyond the nip, the pressure falls substantially and becomes subatmospheric. The subatmospheric pressure is very small and likely matches the vapor pressure of the liquids, which is approximately 0.1 MPa below the atmospheric pressure. Pressures are almost constant for the middle two pressure ports ($z = 0{,}2.5\,mm$), but drop nearer the edge of the wheel (Figure 2-13(b)). The implied lateral pressure gradient drives the side flux and may play a role in the redistribution process at take-off that leads to the lateral variation of film thickness in Figure 2-10. For the three test conditions shown in Figure 2-13(b), the pressure profile is slightly flatter and falls more quickly towards the sides for wheels that are relatively wider, as quantified by the lengthscale ratio, $W/\sqrt{Rh_0}$, a

dimensionless parameter that will be introduced in §2.4. The pressure profiles for different experimental conditions are discussed in Appendix A.

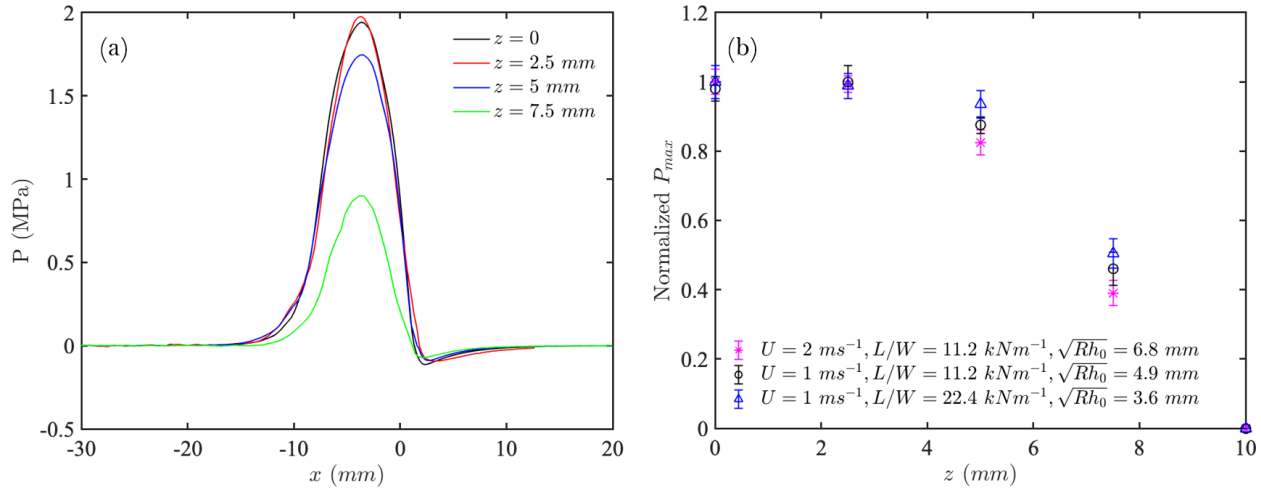

Figure 2-13 a) Axial pressure variation at different lateral locations for U=1 m/s, L/W=11.2 kN/m, μ=8.72 Pa·s (silicone oil), and W=20 mm. b) Variations of the normalized peak pressure in the lateral direction for multiple test conditions at constant width W=20 mm. The peak pressure is normalized by centreline pressure for each test condition. The peak pressures vary by a factor of almost 3 for test conditions in panel (b), from 1.6 MPa for U=2 m/s, L/W=11.2 kN/m to 5.0 MPa for U=1 m/s, L/W=22.4 kN/m. Test fluid is silicone oil.

2.3.2 Higher interactions

Figure 2-7 also displays film thicknesses for higher interactions. Turning first to the silicone oil experiment shown in Figure 2-7(a), one may notice that the fluid left on the running track reduces in depth each time the film splits, weakening the filamented pattern left behind. Also, the side flux during Interaction One leaves fluid adhering to the sides of the wheel, which then transfers back on to the track in subsequent revolutions to reproduce the stripes on either side of the running band. To verify that fluid did not re-enter the gap from the sides during the higher interactions, I conducted other experiments in which the experiment was immediately stopped after the first

wheel-rail interaction. The wheel was separated from the blade by deactivating the pneumatic air cylinders. The edges of the wheel were then carefully cleaned and the experiment resumed with the liquid only present on the contact band of the wheel. For the restart, both wheel and blade were independently brought up to speed whilst separated. The pneumatic air cylinders were then re-activated to drive the wheel into contact with the blade, allowing the subsequent interactions to occur. Figure 2-7(b) displays the repeat of the experiment in Figure 2-7(a), but with the wheel cleaned after Interaction One. The two tests have comparable average film thicknesses on the running band, verifying that an insignificant amount of fluid is transferred back from the sides of the wheel during the higher interactions.

As highlighted by the dashed circles also drawn in Figure 2-7(b,c), the patterns for higher interactions contain common features between consecutive interactions. To explore this observation further, I cross-correlate the images, with the results shown in Figure 2-14. This analysis indicates that Interactions One and Two are not correlated, with small peaks in correlation coefficients (0.13 for silicone oil and 0.08 for glycerin) for spatial shifts that are located far from the center of the images. On the other hand, the Interaction pairs Three/Four and Four/Five are closely correlated, with large peak correlation coefficients (of 0.85 or 0.92 for silicone oil, and 0.69 and 0.58 for glycerin) occurring at the center of the images. Interactions Two and Three are weakly correlated, with correlation coefficients of 0.15 or 0.24 at zero spatial shift.

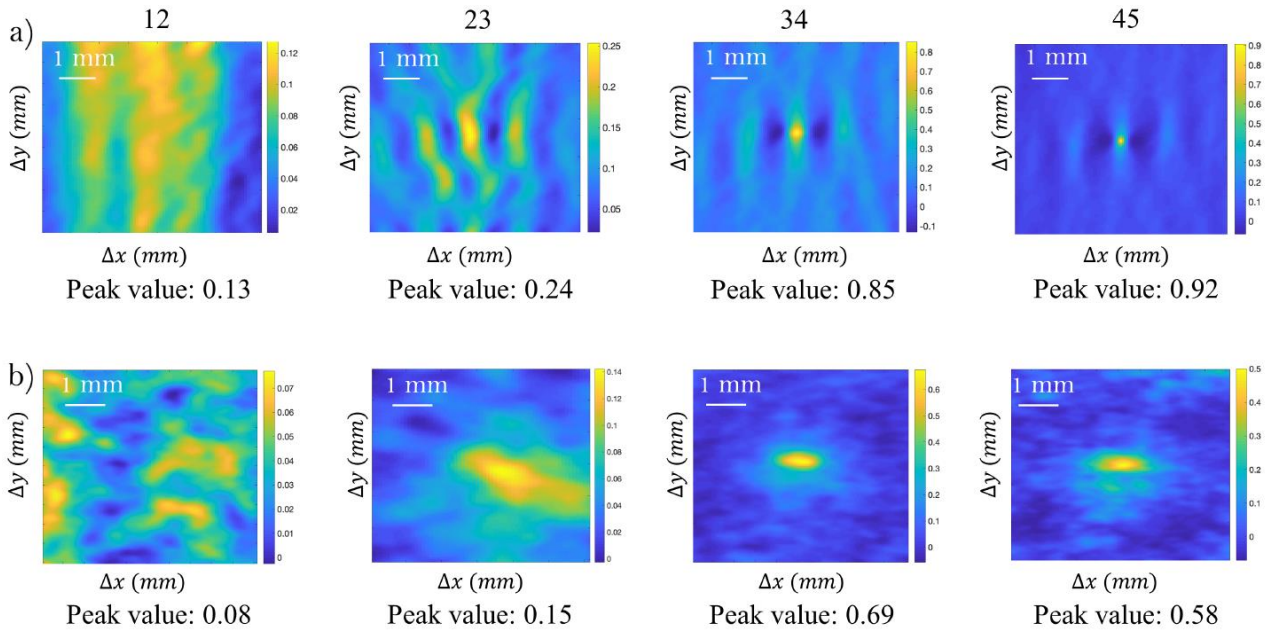

Figure 2-14 Cross-correlation of the experimental images (from Figure 2-7) between different interactions for silicone oil (a) and glycerin (b). As an example, Column "12" refers to the cross-correlation between Interaction pair One/Two. U=1 m/s, L/W=11.2 kN/m, W=10 mm, and h_{in}=500 µm.

The cross-correlation map for silicone oil has negative peaks a short distance to the left and right of the peak coefficient, followed by secondary peaks at twice that distance to either side. These secondary peaks arise from the characteristic length scale present in the pattern of the deposited film in each image, namely the separation between the filaments. The length scale estimated from the cross-correlation is in agreement with direct visual observations using the borescope, as mentioned earlier. For glycerin, however, the secondary peaks are not present because the beading up on the surface generates a largely random pattern of droplets that cannot be aligned for any nonzero spatial shift.

The cross-correlation analysis implies that the pattern in the deposited film is reproduced during the higher interactions, where the liquid layer on the wheel is thin. Evidently, in these interactions, the fluid film is not squeezed back into a uniform sheet by the passage of the wheel,

as it would otherwise suffer another film splitting instability to generate an uncorrelated pattern. Instead, the existing filaments or droplets must retain their shape and become evenly split and "printed" back on the blade after passage through the nip. The fluid mechanics of this "printing" process is very different from that sketched in Figure 2-1(b).

Given that the radius of curvature of the wheel is relatively large ($\frac{R}{h_0} > 100$), one expects the film splitting at the meniscus to be symmetric, with equal amounts of fluid coating the blade and adhering to the wheel. Indeed, by placing aluminum strips on the blade and wheel, it was possible to directly measure the mass of the split films. The split masses after each interaction were equal to within the experimental error, indicating a symmetric film split.

In view of the symmetrical film split, if there is no side flux, the net mass of the lubrication film on the blade for Interaction i should be exactly half the mass at Interaction $i-1$. Figure 2-15 is a plot of twice this mass ratio. The lubricated film mass for Interactions Two and Three is somewhat less than half that at the previous interaction, and the discrepancy identifies side flux. The side flux is obviously important for Interaction One, but cannot be directly measured as the side flux is pushed into the original pool. For Interactions Four and above, the side flux is insignificant. Referring to Figure 2-7(b), one can alternatively calculate the side flux by measuring the mean thicknesses (and thus mass) of the two long strips adjacent to the lubrication film at Interaction Two. This alternative calculation agrees with the direct mass measurements to within experimental error.

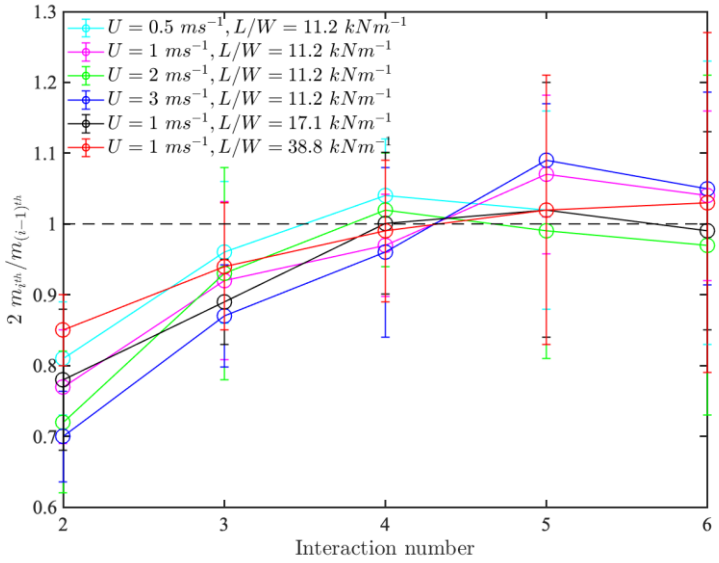

Figure 2-15 Mass m_i^{th} left on the blade after Interaction i multiplied by two and divided by this mass at the previous interaction plotted against *i*. Test conditions are μ=8.72 Pa·s (silicone oil), and W=10 mm. Experiments are averaged over three repetitions and the error bars correspond to one standard deviation of the data.

2.3.3 Wheel liftoff

Although the wheel was pushed off the substrate to deposit a fluid film with finite average thickness in many of our experiments, such lift-off did not always occur. As illustrated in Figure 2-16, the wheel failed to take off at relatively low speed or high load, leaving behind a film with a thickness that was undetectable by the LIF technique. This figure presents experimental film thicknesses averaged over width and the strip of constant depth with length l_c for different speeds (panel (a)) and loads (panel (b)). Note that, as expected from previous discussion, when the wheel lifts off, the deposited film thickness falls by almost a factor of two between interactions. Moreover, for the first interaction, the thickness is roughly proportional to speed and inversely proportional to load (the depth falls by close to a factor of two as the speed is adjusted from

$8\ ms^{-1}$ to $4\ ms^{-1}$ in Figure 2-16(a), then increases by a similar factor when the load decreases from $38.8\ kNm^{-1}\ to\ 17.1\ kNm^{-1}$ in (b)).

One might expect that lift-off fails to occur when the minimum gap required for the fluid flow to build up the lubrication pressure to balance the wheel load becomes smaller than the roughness scale of the solid surfaces, as in bearings [83], [84]. To test the possibility that lift-off was sensitive to surface roughness, thin metal shims were roughened to differing degrees and attached to the blade. The roughness of each shim was measured using an optical profiling system. The liquid was then pooled on top of the shims, and the experiments were conducted as for the original blade surface. No difference was observed in the conditions for lift-off, leading us to conclude that surface roughness did not play any role. In fact, the tests suggested that for the first interaction, lift-off usually occurred provided that

$$\frac{\mu URW}{L} > 19\ \mu m. \qquad \textbf{2-1}$$

As I expose in §2.4 below, the dimensional grouping on the left of equation 2-1 is the primary scaling of the minimum gap h_0 predicted by lubrication theory. Thus, the criterion in 2-1 is equivalent to one on the minimum gap h_0. In line with the shim experiments, the observed threshold of $19\ \mu m$ is far larger than the root-mean-square surface roughness of the wheel and rail, which was measured to be about 850 nm. Indeed, for some of the cases without lift-off, gravimetric measurements of the small amount of liquid that does pass through the nip and becomes left on the blade indicates an average thickness of about 400 nanometers, with the fluid filling the valleys created by the surface roughness rather than forming a continuous sheet. Thus, in these situations, metal-to-metal contact likely occurs between the wheel and track and lubrication pressures are evidently insufficient to counter the applied load and lift the wheel. A similar situation arises for

hydro-planing, although the Reynolds numbers reached there are much higher, and the surface topography of the wheel plays an important role [90], [93].

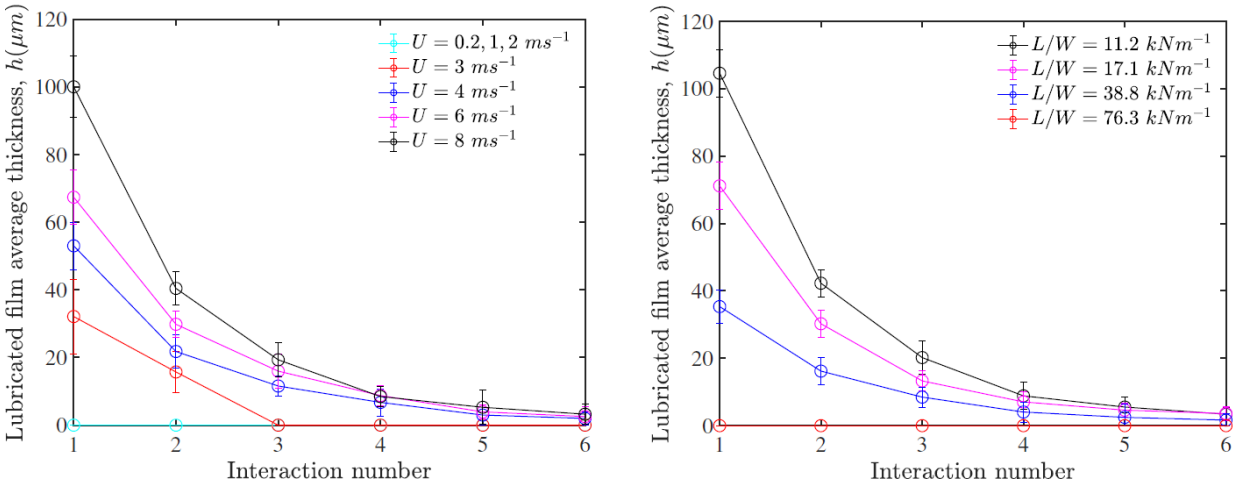

(a) $\mu = 1.19\ Pa \cdot s\ (glycerin),\ L/W = 11.2\ kNm^{-1},\ W = 10\ mm$ (b) $\mu = 8.72\ Pa \cdot s\ (silicone\ oil),\ U = 1\ ms^{-1},\ W = 10\ mm$

Figure 2-16 Film thickness versus interaction number for (a) varying speed U, with a glycerin-water mixture, and (b) varying load, with silicone oil. The initial pool has depth h_{in}=500 µm and length L_0=4 cm. The error bars correspond to one standard deviation of the data with three repeats.

Somewhat surprisingly, the criterion in equation 2-1 is clearly violated for many of the higher interactions of the cases with lift-off in Figure 2-16. The reason for this disagreement is not apparent, although the cross-correlation analysis performed in §2.3.2 highlights how the higher interactions do not take place with the formation of a continuous lubrication film. Rather, the filamentary pattern generated by the printer's instability becomes printed between interactions. Perhaps this spatial inhomogeneity is sufficient to permit lift-off in cases where a continuous film of the same amount of fluid cannot generate the required lubrication pressure.

2.4 Lubrication analysis

Our observations suggest that, when the wheel lifts off, a steady lubrication film is quickly established underneath the cylinder that provides the lift force to counter the load. The steady lubrication continues until the fluid that is ploughed forwards reaches the end of the reservoir entering the gap. In this section, I exploit standard lubrication theory to provide a model for the steady lubrication layer, ignoring the final thinning of the film and touchdown of the wheel back on to the track. I then compare the predictions of the theory with our experimental observations.

2.4.1 Mathematical formulation

As illustrated in Figure 2-1, a Cartesian coordinate system (x, y, z) is used to describe the geometry, in which the $x-$axis points in the forwards direction and the $y-$axis is perpendicular to the rail. I consider the fluid in the nip region from the location of the bow wave $x = x\_l$ to the downstream separation at the meniscus $x = x_m$. Over this region, the gap h in the $y-$direction is much smaller than both W (width) and the length scale $\sqrt{Rh_0}$ characterizing variations in the $x-$direction. The leading-order expressions of mass conservation and force balance then demand

$$u_x + v_y + w_z = 0, \tag{2-2}$$

$$p_x = \mu u_{yy}, \tag{2-3}$$

$$p_y = 0, \tag{2-4}$$

$$p_z = \mu w_{yy}, \tag{2-5}$$

where the fluid velocity and pressure are (u, v, w) and p (respectively), and I have used subscripts as a short-hand notation for partial derivatives. Here, I have neglected gravity, in view of the high

pressures experienced underneath the wheel, and inertia, because the Reynolds number for typical experimental conditions is low ($Re = \frac{\rho U h_0}{\mu} = O(10^{-2})$ for $\rho = 10^3\ kgm^{-3}, U = 1\ ms^{-1}, h_0 = 10^{-4}\ m$ and $\mu = 10\ Pa \cdot\ s$).

The positions, x_l and x_m, as well as the minimum gap h_0 are not known at the outset, but must be determined as a part of the solution to the lubrication equations after the imposition of suitable boundary conditions. On the rail and wheel there is no slip condition:

$$u = U \text{ and } v = w = 0 \text{ at } y = 0, \qquad \textbf{2-6}$$

$$u = U\ , v = Uh_x \text{ and } w = 0 \text{ at } y = h. \qquad \textbf{2-7}$$

Our observations of the free surface profile upstream demonstrate that the bow wave is too steep to be modelled by the lubrication mechanism (Figure 2-11). Therefore, I treat this region as infinitely narrow and replace the bow wave by a discontinuity in depth, applying continuity of mass (i.e., flux) across the resulting shock; see Figure 2-1(b). Because typical capillary numbers are large ($Ca = \frac{\mu U}{\gamma} = 10^2$ for surface tensions γ of order 0.1 Nm^{-1}), I also neglect surface tension and set the pressure to the atmospheric value p_{atm}.

Any treatment of the downstream meniscus is more complicated in view of the severe low pressures that are achieved there, the cavitation that likely results, and the ever-present printer's instability. I avoid such complications by assuming that the fluid cavitates at its vapour pressure $p = p_{vap}$, and the printer's instability does not affect the net flow across the meniscus region. This leads us to follow the analysis of film splitting problems in roll coating [18] and assume that a stagnation point appears at the center of the film.

2.4.2 Reduction

Equation (2-4) implies that the pressure is independent of y; in view of the boundary conditions in Equations (2-6) and (2-7), we may then integrate (2-3) and (2-5) to find the velocity components u and w together with their associated flow rates. The integral of 2-2) across the gap then leads to the Reynolds equation,

$$\frac{\partial}{\partial x}\left(Uh - \frac{h^3}{12\mu}p_x\right) - \frac{\partial}{\partial z}\left(\frac{h^3}{12\mu}p_z\right) = 0, \qquad \textbf{2-8}$$

Where

$$h \approx h_0 + \frac{x^2}{2R}. \qquad \textbf{2-9}$$

In general settings, the solution of (2-8) is complicated by the unknown locations of the curves along the (x, z) −plane identifying the bow wave and downstream meniscus. As our treatment of these locations is rudimentary anyway, to avoid such complications, I adopt a cruder approach in which I assume that the wheel is sufficiently wide that the pressure distribution remains close to that of the two-dimensional problem. With this assumption, the bow wave and downstream meniscus follow approximately straight lines (x_l and x_m are independent of z), and I may solve 2-8) more simply. The key is to first integrate the equation over the wheel width, assuming symmetry about the centreline $z = 0$:

$$\frac{\partial}{\partial x}\left(Uh - \frac{h^3}{12\mu}\bar{p}_x\right) = \left[\frac{h^3}{6\mu W}p_z\right]_{z=\frac{1}{2}W}, \qquad \textbf{2-10}$$

where

$$\bar{p} = \frac{2}{W}\int_0^{\frac{1}{2}W}(p - p_{atm})dz. \qquad \textbf{2-11}$$

To relate the lateral pressure gradient at the edge to the average pressure $\bar{p}$, I employ the approximation, based on dimensional analysis,

$$[p_z]_{z=\frac{1}{2}W} = -\frac{\bar{p}}{\Delta}, \qquad \textbf{2-12}$$

where Δ denotes the characteristic length scale in z over which the pressure falls to its atmospheric value as the side of the wheel is approached. For relatively wide wheels, the most obvious choice for this length scale is $\sqrt{Rh_0}$, and so I take

$$\Delta = C\sqrt{Rh_0}, \qquad \textbf{2-13}$$

where C is a dimensionless constant that must be calibrated by other means. Hence

$$\frac{\partial}{\partial x}\left(Uh - \frac{h^3}{12\mu}\bar{p}_x\right) = \frac{h^3}{6\mu W\Delta}\,\bar{p}\,. \qquad \textbf{2-14}$$

Note that the right-hand side of (2-14) models the loss of fluid at the edges of the wheel; *i.e.*, the side flux. For an infinitely wide wheel $W \to \infty$, this term disappears (2D lubrication) and the equation can be integrated analytically to find the pressure distribution (*e.g.*, Coyle et al. [18]).

Having eliminated the dependence on the lateral coordinate z in this fashion, I must next impose the boundary conditions at x_l and x_m, including an average across the wheel. In particular, at the bow wave I impose

$$\bar{p}(x_l) = 0 \quad \text{and} \quad Q_{in} = Uh_{in} = \left[Uh - \frac{h^3}{12\mu}\,\bar{p}_x\right]_{x=x_l}, \qquad \textbf{2-15}$$

And at the downstream meniscus,

$$\bar{p}(x_m) = p_{vap} - p_{atm} \quad \text{and} \quad \bar{p}(x_m) = 0, \qquad \textbf{2-16}$$

the last of which corresponds to the stagnation-point condition at the film center. Finally, the force balance on the wheel dictates that the net lubrication pressure must balance the applied load:

$$\frac{L}{W} = \int_{x_l}^{x_m} \bar{p}\, dx. \qquad \textbf{2-17}$$

The second-order differential equation (2-14) in combination with the five conditions (2-15), (2-16), and (2-17) determine the average pressure distribution $\bar{p}(x)$ together with the unknown parameters x_l, x_m and h_0. For this task, I solve the equations numerically, employing MATLAB's in-built boundary-value solver, BVP4C.

2.4.3 Sample solutions

To provide some physical insight into the solutions of the model, I display in Figure 2-17 a family of solutions in which I fix the wheel geometry and speed (R, W, and U), the fluid properties (μ and p_{vap}) and the applied load L, but vary the incoming flux Q_{in} by adjusting the incomping pool depth h_{in}. The dimensionless constant C is taken to be 0.87 (the rationale for this choice is provided in §2.4.4).

For low incoming fluxes, the fluid cannot build up appreciably in front of the minimum gap. As a result, the wheel descends close to the rail, with the decrease in h_0 offsetting the relatively small wetted length ($x_m - x_l$) to raise the net lubrication pressure in order to balance the load.

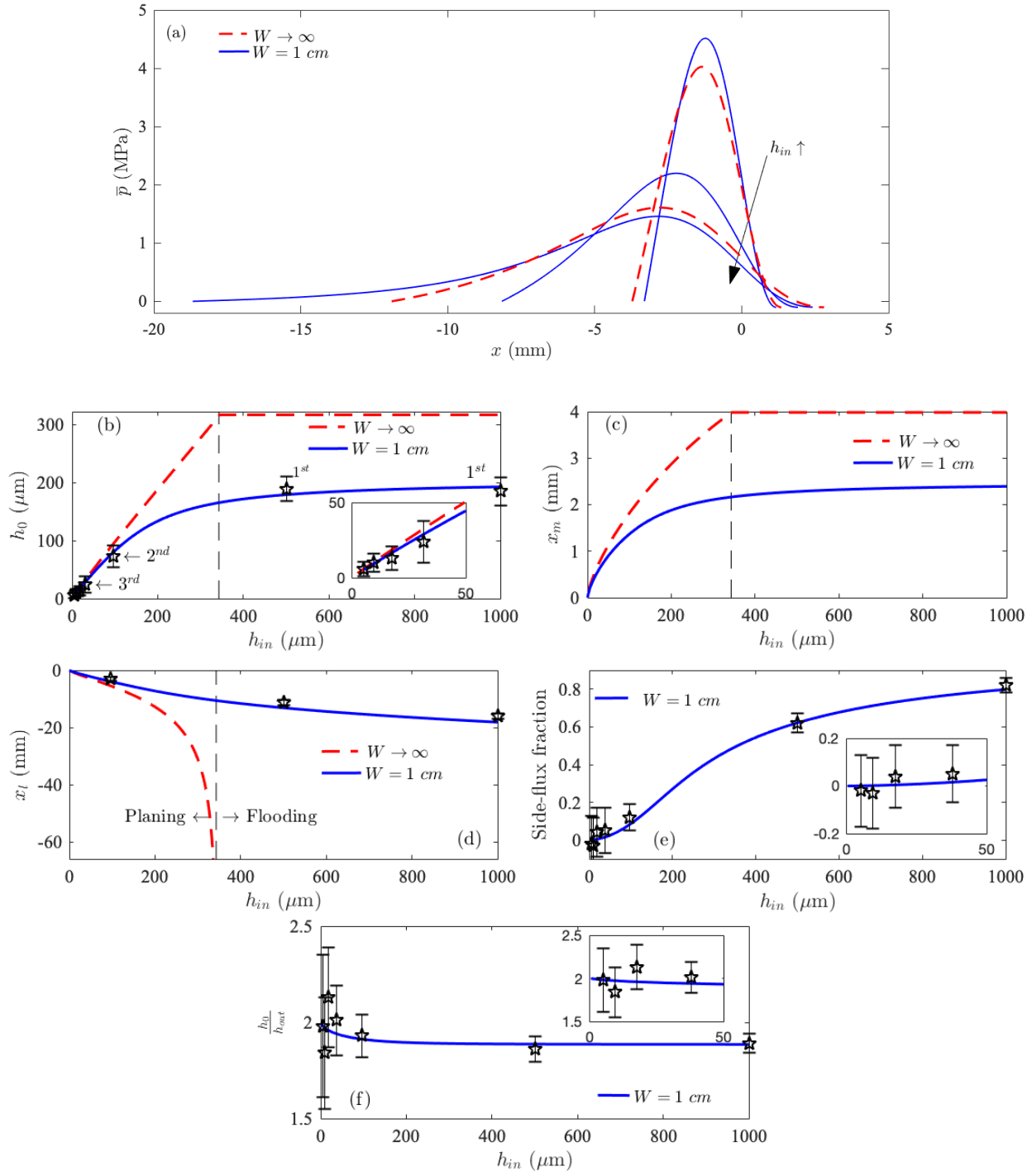

Figure 2-17 Model solutions for varying initial pool depth h_{in}. The solid (blue) curves show result for W=1 cm; the dashed (red) lines show results for an infinitely wide wheel. In (a) we plot a selection of pressure profiles for h_{in}=50, 200, 1000 µm (solution for an infinitely wide wheel is not possible for h_{in} beyond ~ 350 µm, therefore

two red curves correspond to h_{in}=50, 200 μm). Below, against h_{in}, we plot (b) h_0, (c) x_m and (d) x_l. In (e) and (f), for the model with W=1 cm, we respectively plot the fraction of fluid that is diverged to the sides and the ratio h_0/h_{out} . For (b),(d), (e), and (f), we include results from tests conducted at the same experimental parameter settings, showing the gap size, x_l, side-flux fraction, and h_0/h_{out} during the first interaction for a pool with initial depth h_{in}=1000 μm, and then those variables (except x_l) for all six interactions for a pool with h_{in}=500 μm. The bow wave does not form after Interaction Two due to printing, therefore x_l is plotted only for the first two interactions in panel (d). U=1 m/s, L/W=11.2 kN/m, μ=8.72 Pa·s, C=0.87, p_{vap}-p_{atm} = -0.1 MPa. The error bars correspond to one standard deviation of the data with three repeats.

As the flux is increased, the wheel sits further from the rail and the wetted length increases. For somewhat higher fluxes, the wetted length continues to increase, but the minimum gap h_0 and meniscus position x_m level off. This feature reflects how the pressure distribution becomes largely independent of h_{in} once the incoming flux is sufficiently large, and so the load can be balanced without changing h_0. The higher fluxes are compensated chiefly by an increase in the upstream length $|x_l|$. The increased wetted length enhances the side flux, whilst permitting the flow through the nip to remain unchanged.

For comparison, Figure 2-17 also shows corresponding results for an infinitely wide wheel ($W \to \infty$). In this case, steady force balance cannot be maintained for all h_{in}. Below a threshold flux, steady states are possible with a finite wetted length; i.e. “planing states”", as observed when the wheel has finite width and there is side flux. By contrast, above the threshold, the incoming flux is too high to permit steady force balance. Instead, the steady solution disappears and I anticipate a “flooding state” in which the upstream length continually increases with time, all the while maintaining the same minimum gap.

A key feature of the solutions for typical experimental parameter settings is that the peak gauge pressures near the nip are far larger than the pressure at which the fluid cavitates. Consequently, $\bar{p}$ becomes small at $x = x_m$, and the solution becomes insensitive to the precise pressure imposed at the downstream meniscus (as long as it remains small). In this setting, in view of equation (2-14), I then expect the pressure to scale as $\mu U R^{\frac{1}{2}} h_0^{-\frac{3}{2}}$ (the usual pressure scale for a journal bearing or rolling cylinder), but depends on the length scale ratio $\mathcal{R} = \frac{Rh_0}{W\Delta}$ (from the side flux term) and the dimensionless incoming flux $\lambda = \frac{Q_{in}}{Uh_0}$, which mostly controls the position of the bow wave. Thus, the load condition implies a scaling of the form

$$h_0 \sim \frac{\mu URW}{L} I(\mathcal{R}, \lambda), \qquad \textbf{2-18}$$

where the dimensionless factor I incorporates the relative effect of side flux and the bow wave position. This scaling is unfortunately implicit because $\mathcal{R}$ and λ depend on h_0. Nevertheless, when the wheel is wide and the wetted length is sufficiently large that the pressure distribution becomes insensitive to x_l, I is approximately constant and (2-18) identifies the main dependencies of the minimum gap on the experimental parameters. Even if the wheel is not wide and the wetted length is not large (so that the problem remains sensitive to the incoming flux), the minimum gap is expected to depend only on load and viscosity through the combination L/μ. The dependence on wheel width and speed is more convoluted, as changing those parameters affects the wetted length and degree of side flux.

2.4.4 Calibration of C

Our method for dealing with side flux in the model introduces a free parameter C that requires calibration. For this task, for each of the tests that was conducted, I match the experimental parameters and then find (using Newton iteration) the value of C for which the theoretical prediction for the final deposited film thickness h_{out} matches that measured experimentally. The resulting values of C are plotted against $\frac{W}{\sqrt{Rh_0}}$ in Figure 2-18(a).

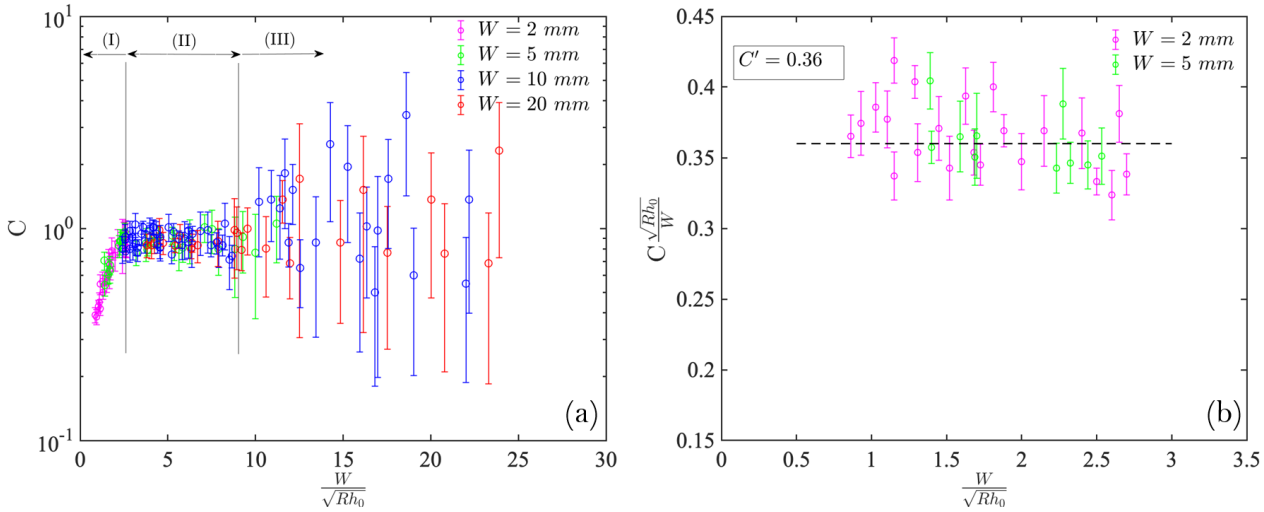

Figure 2-18 a) Fits of the constant C as a function of the ratio $W/\sqrt{Rh_0}$. Three distinct regions are identified based on whether the fitted values depend systematically on $W/\sqrt{Rh_0}$ (I), are independent of this ratio (II), or inaccurately identified because side flux is low (III). In (b) The results for $\frac{W}{\sqrt{Rh_0}} < 2.5$ are replotted, scaling C with $\frac{W}{\sqrt{Rh_0}} < 2.5$.

Three regions are identified on this graph: for relatively wide wheels with $\frac{W}{\sqrt{Rh_0}} > 9$ (labelled III in the figure), there is much scatter in the fitted values of C. This scatter reflects how the side flux for such cases is small, and any attempt to fit the corresponding parameter C of the

theory is suspicious. In addition, this is also the region where printing interactions can occur and the model does not apply. For moderate wheel widths, $2.5 < \frac{W}{\sqrt{Rh_0}} < 9$ (region II in the figure), the scatter in the fitted values of C is less and the experiments support the parameterization of the model, $\Delta = C\sqrt{Rh_0}$ with $C \approx 0.87$. At yet lower wheel widths $\frac{W}{\sqrt{Rh_0}} < 2.5$ (labelled I in the figure), the fitted values for C depend systematically on the ratio $\frac{W}{\sqrt{Rh_0}}$. For such narrow wheels, I conclude that the parametrization $\Delta \sim \sqrt{Rh_0}$ is poor, owing to significant lateral pressure gradients and side flux. An alternative for these cases is to use the wheel width W for the length scale Δ over which the pressure declines near the side of the wheel. As shown in Figure 2-18(b), the alternative parameterization $\Delta = C'W$ with $C' \approx 0.36$ (or $C = \frac{C'W}{\sqrt{Rh_0}}$) performs better here. In view of these findings, to complete the model, I set

$$\Delta = \begin{cases} C'W \approx 0.36W & \text{for} \quad \dfrac{W}{\sqrt{Rh_0}} < 2.5 \\ C\sqrt{Rh_0} \approx 0.87\sqrt{Rh_0} & \text{for} \quad \dfrac{W}{\sqrt{Rh_0}} > 2.5 \end{cases} \qquad \textbf{2-19}$$

2.4.5 Comparison of theory and experiments

The performance of the calibrated model in predicting the final average film thickness is shown in Figure 2-19. Figure 2-17 also makes a direct comparison of the theory and experiment for a particular pair of tests. In Figure 2-19, I include results from all the interactions from experiments conducted with different pool depths, pool lengths, wheel widths, velocities, fluid viscosities, and loadings. For comparison, I also show the corresponding results in which the side flux is neglected. That version of the model is insufficient to reproduce the observations, particularly for the first

interaction. By contrast, for the full model (labelled "Finite W"), the root-mean-square discrepancy between the model and the experiments is 5.9%, which is comparable to the experimental error. Note that, strictly speaking, the model cannot apply to Interaction Three and higher, owing to the switch of the dynamics for these interactions to printing. Nevertheless, the model continues to perform well, simply because it predicts a weak fluid flow under the wheel and an equal split of the film between wheel and rail, leading to $h_{out} = \frac{1}{2} h_{in}$, as for printing.

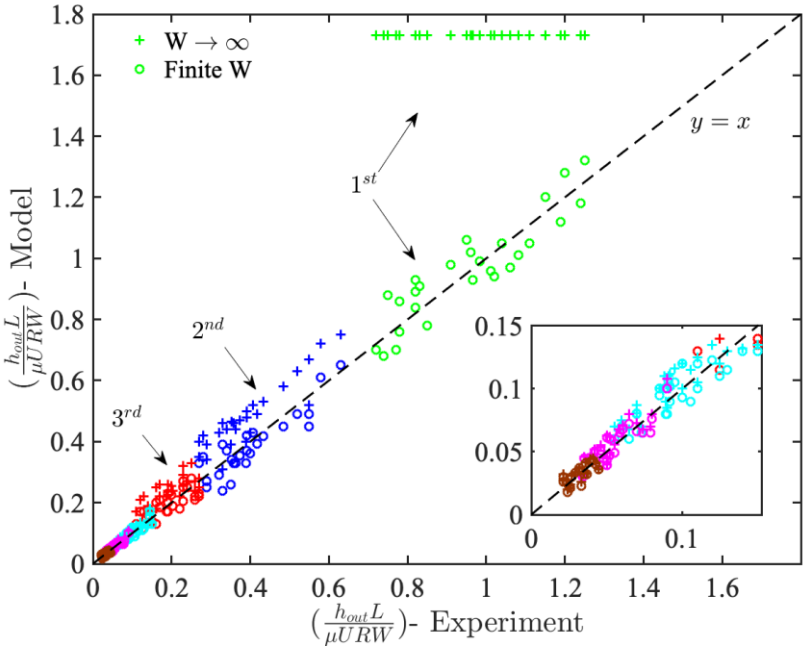

Figure 2-19 Scaled film thicknesses $h_{out}L/(\mu URW)$ predicted by the model plotted against those measured experimentally.

Although the agreement in Figure 2-19 is satisfying, the predictive power of the model is offset by the need for the calibration in (2-19). A more demanding test of the model is shown in Figure 2-20, which compares measured and predicted average pressure profiles $\bar{p}$ for the wide wheel ($W = 20\ mm$) for three different parameter settings. For this comparison, the experimental pressure profiles from the four ports across the wheel (at $z = 0, 2.5, 5$ and $7.5\ mm$) that are shown

in Figure 2-13 are integrated by the trapezoid rule, assuming further that the pressure distribution is symmetrical about the centerline $z = 0$ and that $p = p_{atm}$ at the sides. In addition to the pressure distribution comparisons of Figure 2-20, I also made measurements for other test settings. In all cases, the model reasonably matches the observations, with differences of 8% and 2% in the peak and net pressures, and a comparable mismatch in the apparent wetted length. However, the observations of the lateral pressure gradients at the wheel edge in Figure 2-13(b) do not fully support the parameterization in (2-12) with $\Delta = C\sqrt{Rh_0}$ (the observed pressure profiles are little different, even though $\sqrt{Rh_0}$ varies by a factor of about two).

Further experimental measurements that can be compared against theory include the direct measurement of the upstream position of the bow wave from the side profiles (*i.e.* x_l; see Figure 2-11), and the ratio of the minimum gap h_0 from the proximity probe to the final film thickness h_{out} from LIF (*cf.* Figure 2-8). For a particular test condition, these comparisons are included in Figure 2-17 for x_l (panel (d)) and $\frac{h_0}{h_{out}}$ (panel (f)). The predicted ratios $\frac{h_0}{h_{out}}$ from the model match the measured values to within experimental uncertainties. This ratio is expected to be 2 for higher interactions where printing occurs and the lubrication theory breaks down. On the other hand, the theory consistently over predicts the bow wave position by $1.8\,mm$ on average for the bulk of the experimental conditions. For instance, for the test in Figure 2-11, the theory predicts that $x_l = -16.3\,mm$, whereas the direct measurement is $x_l = -14.1\,mm$, in agreement with what one would infer from the pressure measurements in Figure 2-13 and Figure 2-20. Side-flux fractions, predicted by the model, are also in agreement with the observations to within experimental error (see panel (e) in Figure 2-17).

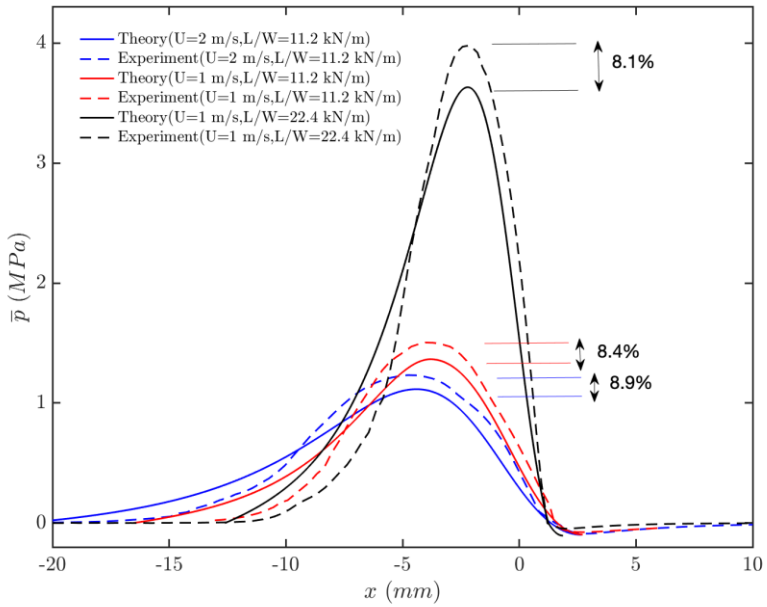

Figure 2-20 Experimental (dashed) and theoretical (solid) pressure profiles, averaged across the wheel and plotted against distance down the track. Other test conditions: μ=8.72 Pa· s and W=20 mm.

2.5 Conclusions

In this chapter, I provided an experimental exploration of a cylinder rolling on a substrate through a pool of viscous fluid. When the cylinder rolls over the pool, some fluid is ploughed ahead of the cylinder, some is pushed laterally, and in some cases, a lubrication film forms between the cylinder and the substrate. Measurements were taken of the gap between the cylinder and substrate, the fluid pressure and the residual film of fluid deposited on the running band. The thickness of the lubrication film rapidly rises to a steady value (which is a function of the fluid viscosity and the cylinder speed, load and width, but not dependent on the depth and length of the initial pool) until the fluid ploughed ahead of the cylinder reaches the end of the pool, whereupon the film thins and the wheel returns to the substrate. The lubrication film splits behind the wheel at a meniscus, but suffers the printer's instability which breaks the deposited films up into filamentary patterns. After

this first interaction, the fluid adhering to the cylinder is then rotated back round to prompt further events of lubricated rolling. The amount of ploughing and side flux declines quickly during these higher interactions, with the film always splitting evenly between the wheel and substrate.

The steady state attained during the bulk of the interaction motivated the development of a model based on Reynolds lubrication theory. The model incorporates the bow wave at the front of the ploughed fluid, the splitting of the downstream meniscus and the flux of fluid to the sides in a cruder fashion. In particular, the side flux is dealt with by introducing a parameterization of the lateral pressure gradient at the sides of the wheel, which requires a constant to be calibrated. With that fitted constant, the model is able to predict the minimum gap, coating thickness, peak fluid pressure and bow-wave position to within root-mean-square errors of less than ten percent. This success is, perhaps, surprising in view of the simplistic approach I have taken in the modelling and given the more complex fluid mechanics that arises at the wheel's sides, bow wave and filamented meniscus.

Some of the findings of this chapter can be used to better understand the wheel/rail interface. In the real application, due to significantly higher loads, liftoff will likely fail to occur and there will be either boundary or mixed lubrication contact. Even if liftoff were to happen, the model generally estimates the coated film thicknesses below $\sim 5\,\mu m$ for the commercial train conditions (simply assuming the product has the same viscosity as glycerin), which are comparable to the scale of surface roughness or irregularities. However, it seems like if liftoff occurs during the first interaction, the printing phenomenon helps in carrying the product to longer distances.

Chapter 3: Lubricated Rolling Over a Non-Newtonian Pool

3.1 Introduction

Many industrially important fluids are non-Newtonian. In this chapter, I carry out an experimental and theoretical study of a cylinder rolling over a pool of shear-thinning fluid. Measurements were taken of the gap size, pressure profiles and the bow wave position for two different shear-thinning liquids. The upstream bow wave and the downstream meniscus were also visualized. The results are presented in §3.3. The experiments are complemented with a lubrication-based model in §3.4. I conclude in §3.5 with a discussion of key findings.

3.2 Materials and methods

The experimental apparatus is that used in Chapter 2 and sketched in Figure 2-2. The experiments were conducted for the wide wheel with $W = 20\ mm$. All components and measurement sensors were the same except the pneumatic air cylinders and the load cell. Heavy load cylinders were initially (Chapter 2) installed in the apparatus to mimic the load present in the rail transport application. However, for the non-Newtonian experiments, it was observed that under this heavy load, the thickness of the lubrication film is very thin even at the high speed. This will lead to the shear rates of $\dot{\gamma} \sim \frac{U}{h_0} \sim 10^4 - 10^5\ s^{-1}$ in the experiments, which is one or two order of magnitudes larger than the measurement range of a typical rheometer and above the range of shear rates at which the sample liquids are believed to maintain a power law behavior. To permit comparison with the theory, which requires a simple power law dependence of viscosity on shear rate, the original air cylinders were replaced with smaller ones (100 N @ 100 psi) to apply lighter loads. Simultaneously, a new load cell with a smaller measurement range was installed (Digi-Key, #FX1901). With the new air cylinders in place, it was possible to reduce the applied load by more

than one order of magnitude, allowing us to achieve the same minimum gap but under significantly lower speeds (i.e., much lower shear rates).

Mixtures of glycerin and xanthan gum at two different concentrations (0.25% and 0.5%) were used as shear-thinning fluids. Technical-grade glycerin (≥ 99.5% pure- #G9012-2L) and the xanthan gum powder (#11138-66-2) were purchased from Sigma Aldrich. To avoid lump formation, the xanthan gum was slowly added to the glycerin in an agitated vessel. The mixing was continued for 12 h. The solutions were left in repose for at least 24 h before experiments.

The rheological properties of the glycerin and xanthan gum solutions were measured on a Anton-Paar Physica MCR 301 rheometer with a Couette geometry and a gap width of 3 mm, and are shown in Figure 3-1. The shear-thinning fluids have a power-law behavior in almost all the shear rate interval, although a mild plateau can be observed for shear rates below $10\ s^{-1}$. The power-law parameters are: $K = 8.8\ Pa \cdot s^n, n = 0.75$ (correlation coefficient: 0.991) for 0.25% xanthan gum, and $K = 42.5\ Pa \cdot s^n, n = 0.56$ (correlation coefficient: 0.987) for 0.5% xanthan gum.

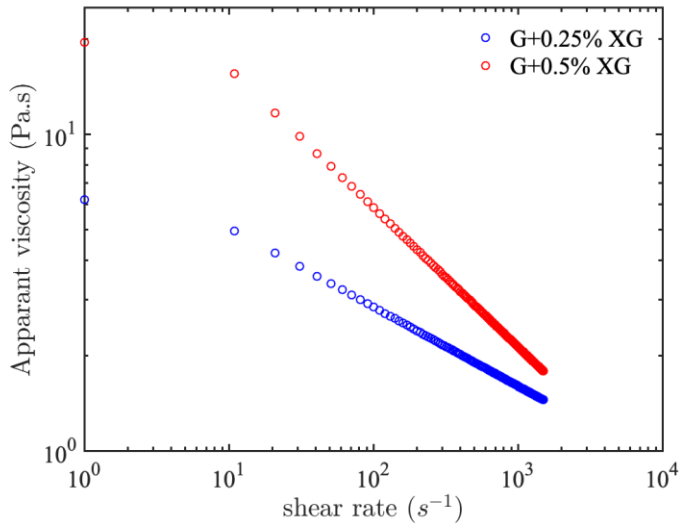

Figure 3-1 Flow curves of the test liquids, apparent viscosity versus the shear rate.

Table 3-1 shows the summary of tests carried out for this chapter.

Table 3-1 Summary of the test details for shear-thinning fluids

Sample	n	K $(Pa \cdot s^n)$	$\frac{L}{W}$ (kNm^{-1})	U (ms^{-1})	W (mm)
G+0.25% XG	0.75	8.8	0.8-1.7	0.4-1.6	20
G+0.5% XG	0.56	42.5	0.8-1.7, 11.2	0.4-1.6	20

3.3 Results

3.3.1 General results

Figure 3-2 shows an example of the deposited film on the track for glycerin with 0.5% xanthan gum, showing four cylinder-substrate interactions. Consistent with Figure 2-7(c), the glycerin beads up on the surface after suffering from printer's instability at the film-splitting meniscus. Similar to the Newtonian fluids, the patterns for higher interactions contain common features between consecutive interactions, suggesting printing. The cross-correlation heat map, displayed in Figure 3-3, shows that Interaction pairs 23 and 34 are correlated with peak correlation coefficients occurring at the center of the images. However, Interactions One and Two are not correlated with a small peak correlation coefficient that occurs far from the center of the images. Printing, therefore, appears to arise after the second interaction.

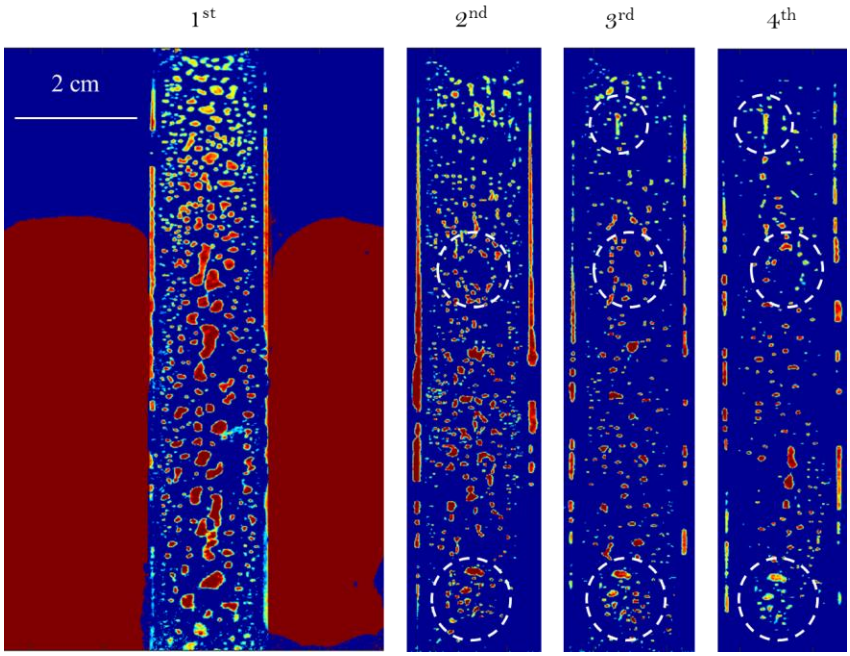

Figure 3-2 LIF images of the coated track for glycerin with 0.5% xanthan gum for four interactions. The dashed circles highlight sectors of the film over which the thickness pattern is reproduced during an interaction. Test conditions: U=0.8 m/s, L/W=1.2 kN/m, L_0=8 cm, h_{in}=500 µm, and W=20 mm.

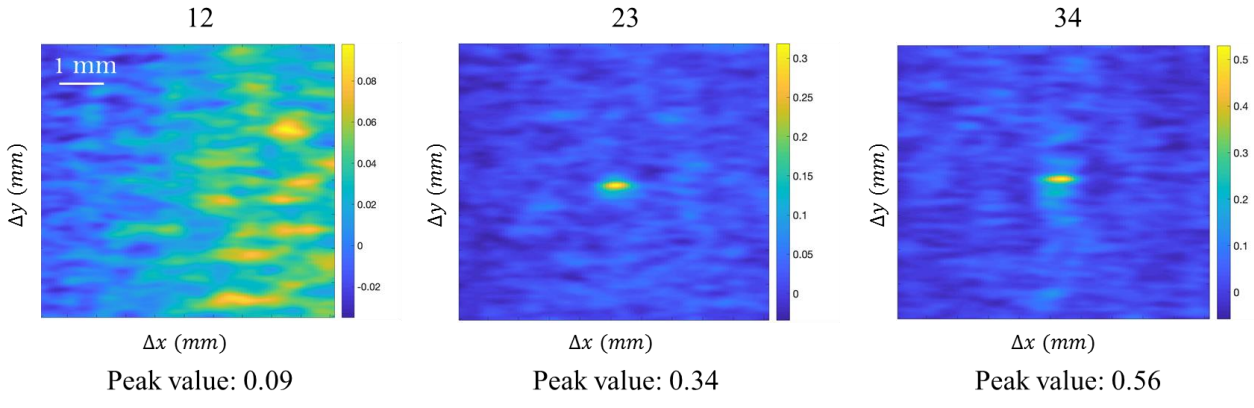

Figure 3-3 Cross-correlation of the experimental images between different interactions for glycerin with 0.5% xanthan gum. As an example, Column "12" refers to the cross-correlation between Interaction pair One/Two. U=0.8 m/s, L/W=1.2 kN/m, h_{in}=500 µm, and W=20 mm.

Observations of the upstream bow wave (Figure 3-4(a)) and downstream meniscus (Figure 3-4(b)) for the 0.5% xanthan solutions qualitatively show a similar fluid structure as for the Newtonian fluid. The bow wave position, however, is quantitatively different; an observation that will be explored in §3.3.2. The meniscus imaging clearly shows the formation and elongation of fluid filaments for the glycerin solutions, but due to dewetting after passage of the wheel, the liquid forms beads on the surface.

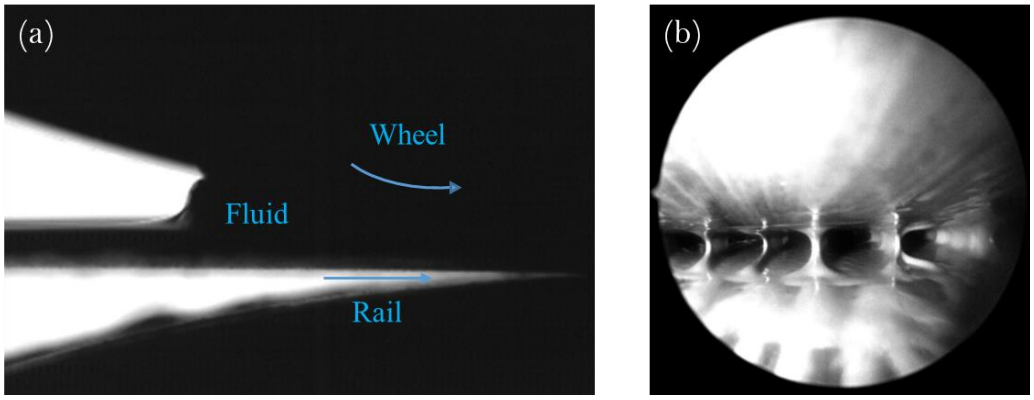

Figure 3-4 High speed image of the upstream interface (a) and borescope image of the downstream meniscus (b) for the G+0.5% XG. U=0.8 m/s, L/W=1.2 kN/m, h_{in}=500 µm, and W=20 mm.

Figure 3-5 shows the gap size variations for the bulk of the experimental conditions versus the distance along the pool. The variations in the gap size generally follow that of the Newtonian fluid: a quick rise in the gap thickness (Phase I), then a steady gap until slightly after the end of the pool is reached (Phase II), followed by a gradual decrease in the gap size (Phase III), and finally the final touchdown of the wheel. The gap size increases with the speed and decreases with the load, as for Newtonian fluids. In Figure 3-6 I show that the non-dimensional grouping $\frac{h_0}{U}\left(\frac{L}{KRW}\right)^{\frac{1}{n}}$ (that I introduce in §3.4) can successfully scale the experimental data, relating the gap size to load by $h_0 \sim L^{\frac{1}{n}}$. The scaling suggests that the dependence of the gap size on the load is non-linear for the shear-thinning fluids, unlike Newtonian fluids. Ideally, for an infinitely wide wheel I expect

that the scaled gap sizes in Figure 3-6 fall onto a straight line; however, in the presence of the side flux occurring for thin wheels, the graph has a downward slope owing to increased side leakage for thicker lubrication films.

Figure 3-6 also shows the results of two experiments run with the heavy load system, for which the shear rates are high ($\dot{\gamma} > 2.5 \times 10^4\ s^{-1}$). The discrepancy between those points and the rest of the measurements with $2000\ s^{-1} < \dot{\gamma} < 7000\ s^{-1}$ (open circle points), is an indication that the liquid ceases to display simple power-law behavior at high shear rates. In fact, other researchers [120], [121] showed that for the aqueous solutions of xanthan gum with shear rates well above $10^3\ s^{-1}$ and up to $10^5\ s^{-1}$, the viscosity function levels off and finally the high-shear-rate plateau (second Newtonian branch) is reached. The onset of this regime depends on the xanthan concentration [120]. This regime, unfortunately, is not completely understood in the literature due to lack of adequate measurement equipment which can go to those high shear rates. As a result the infinite-shear viscosity is often obtained by extrapolating the deviation from the power law behavior using Carreau-Yasuda model. In our problem, a simple extrapolation of the power law behavior for the 0.5% xanthan solution at the shear rate $\dot{\gamma} = 3 \times 10^4\ s$ yields the apparent viscosity $\mu_a = 0.46\ Pa.s$, which is unrealistically low given the viscosity of the base fluid glycerin. This issue will be discussed later in the chapter.

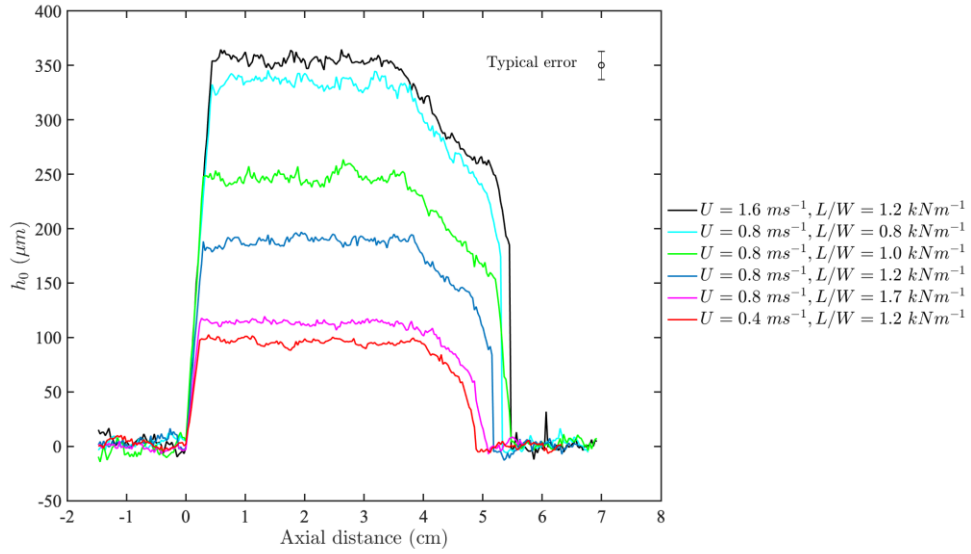

Figure 3-5 Gap size measurements for Interaction One as a function of distance along the pool. Tests fluid is glycerin with 0.5% xanthan gum. Other test conditions: W=20 mm, h_{in}=500 µm, and L_0=4 cm. The error bars correspond to one standard deviation of the data with three repetitions.

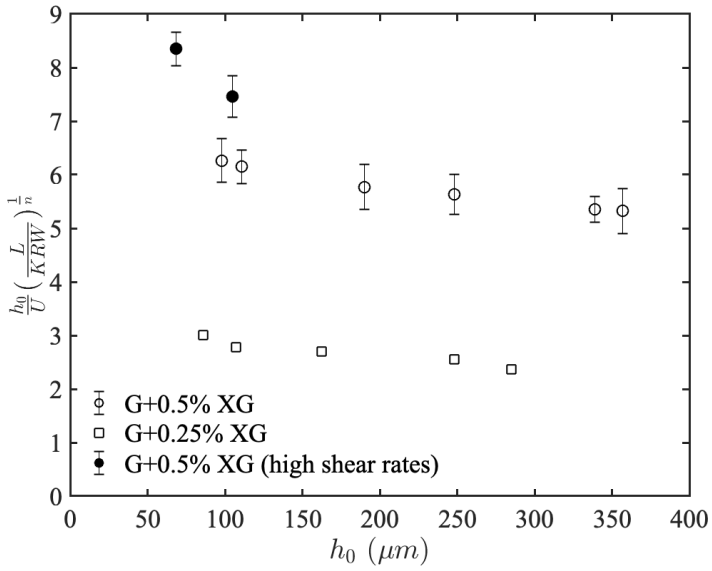

Figure 3-6 Scaled gap sizes for the first interaction for various loads and speeds. As an example, "G+0.5% XG" refers to the solution of glycerin with 0.5% xanthan gum. Solid points show the two experimental points with high shear rates conducted for the higher concentrated solution. The error bars correspond to one standard deviation of the data with three repetitions.

Evidence of wheel lift-off failure, as has been observed for Newtonian fluids, is provided in Figure 3-7. I conducted a sequence of experiments in which I fixed the load and reduced the speeds until the gap size between the wheel and the surface becomes undetectable. As illustrated in Figure 3-7, the wheel remained in solid contact with the substrate at speeds lower than 0.4 m/s for a given load, although extrapolating the film thickness measurements from higher speeds would suggest an easily measurable film would be present for these cases.

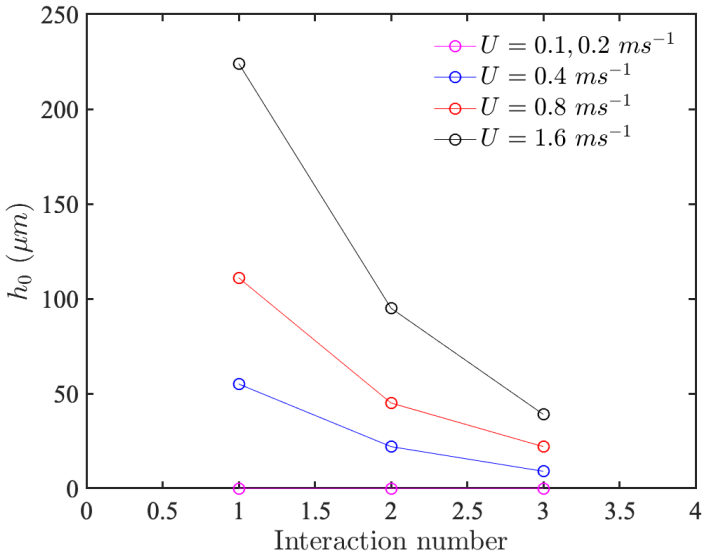

Figure 3-7 Gap size measurements for varying speeds under fixed load L/W=1.2 kN/m. The initial pool has depth h_{in}=500 µm and length L_0=4 cm, and the test fluid is glycerin with 0.5% xanthan.

3.3.2 Direct comparison with a Newtonian fluid

For a precise "head-to-head" comparison of Newtonian and non-Newtonian fluid effects, I ran a separate experiment in which I kept the load and speed constant, and varied the Newtonian liquid viscosity until I had the same minimum gap as for the non-Newtonian fluid run under the same conditions. Then, a comparison of the second interaction and the resulting pressure distributions (axially and laterally) would give evidence of non-Newtonian effects. A new Newtonian liquid

was prepared by thinning the silicone oil used in Chapter 2. By trial and error, a mixture of 68% silicone oil with $\mu = 0.5\ Pa \cdot s$ and 32% silicone oil with $\mu = 8.7\ Pa \cdot s$ produced the same minimum gap (within experimental uncertainties) for Interaction One as for the non-Newtonian fluid (0.5% xanthan gum solution) run under the same loading and speed (Figure 3-8(a)).

With the matched minimum gap and initial pool depth, the ploughing length l_p is shorter for the non-Newtonian fluid, suggesting less fluid accumulation ahead of the wheel (or equivalently greater side leakage). Non-Newtonian effects are particularly clear during Interaction Two (Figure 3-8(b)) where the gap size is smaller for the shear-thinning fluid relative to the Newtonian fluid, even though the two fluids have the same minimum gap size during the first interaction. This finding may be counter intuitive at a first glance as other researchers [96] reported that in roll coating, where the gap size is fixed, the flow rate and consequently the coating thickness increase for the shear-thinning fluids due to increased mobility of the fluid. However, that geometry and underlying physics are completely different from the problem studied here as the load in roll coating is not maintained constant.

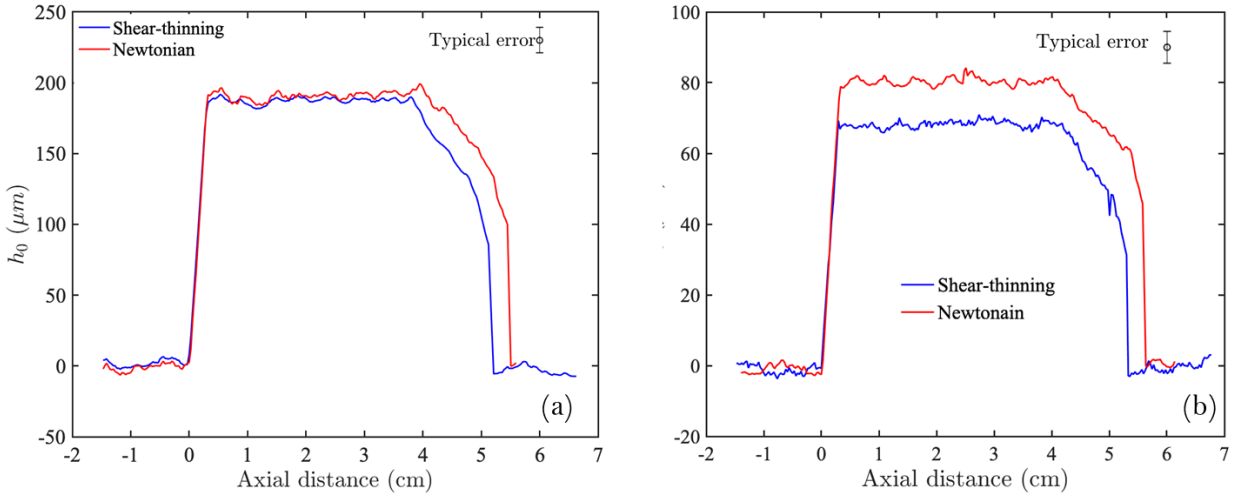

Figure 3-8 Comparison of gap sizes for Newtonian and shear-thinning fluids during Interaction One (a) and Interaction Two (b) under the same speed U=0.8 m/s and load L/W=1.2 kN/m. The shear-thinning fluid is glycerin with 0.5% xanthan and the Newtonian fluid is a mixture of 68% silicone oil with μ=0.5 Pa·s and 32% silicone oil with μ=8.7 Pa·s, as described in the text. The results shown were averaged over three repetitions with the error bar corresponding to one standard deviation of the data.

Comparison of pressure profiles provides further evidence of the non-Newtonian effects. Figure 3-9 shows the axial pressure profiles for four ports across the wheel width during Interaction One for both Newtonian and non-Newtonian samples that generate the same minimum gap. The wetted length over which the pressure develops axially is evidently shorter for the shear-thinning fluids, which is consistent with an observation of shorter l_p. The shorter wetted length leads to a larger peak pressure in Figure 3-9 to maintain the same load. The greater difference, however, lies in the lateral distribution of the pressure. For the non-Newtonian fluid, the lateral pressure distribution is flatter around the wheel centerline and drops more abruptly as one approaches the edge of the wheel.

The pressure profiles of Figure 3-9 are integrated laterally across the width by the trapezoidal rule, assuming zero pressure at the edge, and the resulting profiles are displayed in Figure 3-10(a). The lateral distributions of the normalized peak pressures are shown in Figure 3-10(b). In this figure the peak pressure for each pressure port is normalized by the centerline pressure.

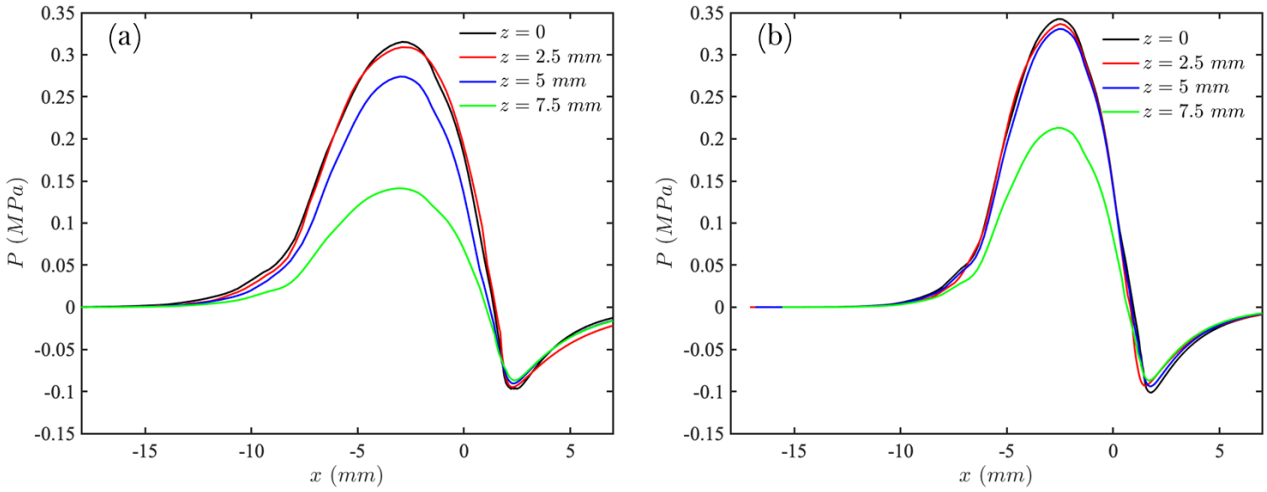

Figure 3-9 Pressure profiles from four pressure ports across the width plotted against the axial distance for the (a) Newtonian fluid and (b) shear-thinning fluid. The fluids are those described in the caption of Figure 3-8. U=0.8 m/s, L/W=1.2 kN/m, W=20 mm.

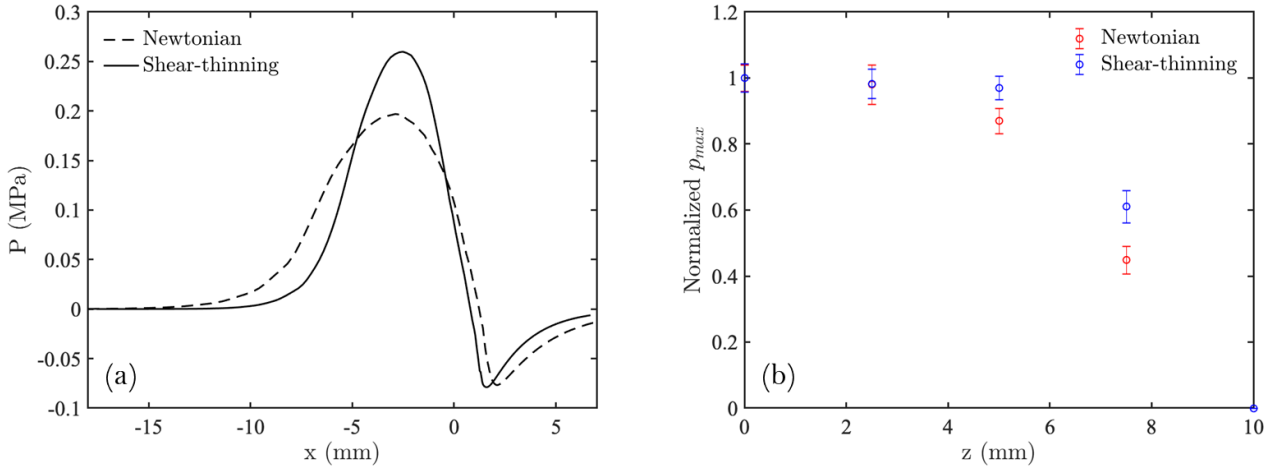

Figure 3-10 (a) Pressure profiles for Newtonian and shear-thinning fluids, averaged across the wheel and plotted against distance down the track. (b) The lateral distribution of the peak pressures. The fluids are those described in the caption of Figure 3-8. U=0.8 m/s, L/W=1.2 kN/m, W=20 mm.

The other observed distinction between the Newtonian and the shear-thinning fluids is the position of the bow wave, as shown in Figure 3-11. Less fluid is accumulated ahead of the wheel for the shear-thinning fluids, consistent with what one would infer from the pressure profiles.

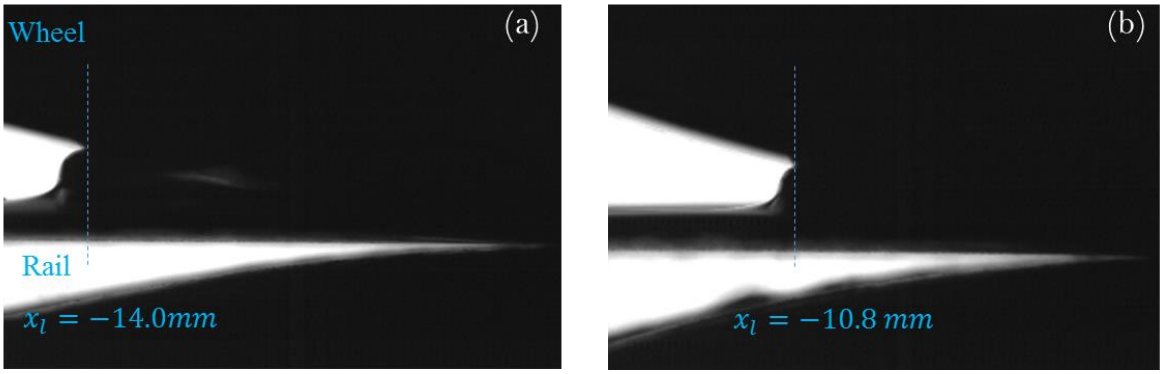

Figure 3-11 Bow wave positions for the (a) Newtonian fluid and (b) shear-thinning fluid. Test fluids are those described in the caption of Figure 3-8. U=0.8 m/s, L/W=1.2 kN/m, W=20 mm.

3.4 Lubrication analysis

The steady state flow (constant gap size) observed during the bulk of the cylinder-substrate interaction motivated the development of an equivalent model for a power-law fluid to that discussed in §2.4. The model is based on the lubrication geometry (from upstream jump $x = x_l$ to downstream meniscus $x = x_m$) and incorporates a shear-sensitive viscosity term. The model is calibrated by the experiments and the comparison is made of the theory and the experiments.

3.4.1 Mathematical formulation

I use the same coordinates and notations that were introduced in §2.4.1. Within the nip region, where the length scale in the y-direction is much smaller than those in the x and z directions, the leading-order expressions of mass conservation and force balance demand

$$u_x + v_y + w_z = 0, \tag{3-1}$$

$$-p_x + \left(K|\dot{\gamma}|^{n-1}u_y\right)_y = 0\,, \tag{3-2}$$

$$p_y = 0, \tag{3-3}$$

$$-p_z + \left(K|\dot{\gamma}|^{n-1}w_y\right)_y = 0, \tag{3-4}$$

where the net shear rate is expressed by $\dot{\gamma} = \sqrt{u_y^2 + w_y^2}$ and K and n are the power law parameters that were introduced in §3.2. Here, I neglected gravity, due to the high lubrication pressure underneath the wheel, and inertia due to the low characteristic Reynolds number. The boundary conditions on the wheel and the rail are those specified in equations (2-6), (2-7). To avoid complications on the free surfaces, I make similar approximations to treat the upstream bow wave and downstream meniscus. For the upstream jump, I replace the bow wave by a discontinuity in

depth and then demand that the flux through the boundary has to be continuous. I also set the pressure to the atmospheric value p_{atm} on that boundary owing to typically large Capillary numbers in the experiments. For the meniscus, I truncate the pressure at the vapor pressure, as suggested by experiments in Figure 3-9. I also assume a stagnation point at the center of the film at the meniscus [18].

According to (3-3), the pressure is independent of y; (3-2) and (3-4) are integrated over y knowing that the shear rate is zero at $y = \frac{h}{2}$. Both sides of the resulting equations are squared and then added to yield an equation for the shear rate

$$\dot{\gamma} = \left(\frac{\sqrt{p_x^2 + p_z^2}}{K}\right)^{\frac{1}{n}} \left|y - \frac{h}{2}\right|^{\frac{1}{n}}. \qquad \textbf{3-5}$$

The fluid viscosity, which is sensitive to the shear, also depends on the pressure gradients in the (x, z)- directions as the shear rates and pressure gradients are related. For ease of writing, I define $S = \sqrt{p_x^2 + p_z^2}$. I can then use the shear rate equation and integrate equations (3-2) and (3-4) with respect to y to get the velocity gradients as follows,

$$u_y = \frac{p_x\left(y - \frac{h}{2}\right)}{K^{\frac{1}{n}} S^{\frac{n-1}{n}} \left|y - \frac{h}{2}\right|^{\frac{n-1}{n}}}, \qquad \textbf{3-6}$$

$$w_y = \frac{p_z\left(y - \frac{h}{2}\right)}{K^{\frac{1}{n}} S^{\frac{n-1}{n}} \left|y - \frac{h}{2}\right|^{\frac{n-1}{n}}}. \qquad \textbf{3-7}$$

The integral of mass conservation (3-1) across the gap ($\frac{\partial}{\partial x}\int_0^h u dy + \frac{\partial}{\partial z}\int_0^h w dy = 0$) then leads to the Reynolds equation for the power-law fluid,

$$\frac{\partial}{\partial x}\left(Uh - K^{-\frac{1}{n}}\frac{n}{2n+1}2^{-\left(\frac{1}{n}+1\right)}S^{\frac{1}{n}-1}\,h^{2+\frac{1}{n}}\,p_x\right) + \frac{\partial}{\partial z}\left(-K^{-\frac{1}{n}}\frac{n}{2n+1}2^{-\left(\frac{1}{n}+1\right)}S^{\frac{1}{n}-1}\,h^{2+\frac{1}{n}}\,p_z\right) = 0, \quad \textbf{3-8}$$

where $h = h_0 + \frac{x^2}{2R}$. For the Newtonian case $n = 1$, the equation reduces to (2-8).

3.4.2 Reduction

The solution of (3-8) is complicated by the unknown locations of the bow wave and meniscus. Similar to the theory for a Newtonian fluid, I take a cruder approach and assume that the wheel is sufficiently wide that the pressure distribution remains that of the two-dimensional problem. With this assumption, the bow wave x_l and meniscus x_m are independent of z, enabling us to solve equation (3-8) more readily. I first integrate the equation over the wheel width W, with the symmetry about the wheel centerline $z = 0$ in mind:

$$\frac{\partial}{\partial x}\left(Uh - K^{-\frac{1}{n}}\frac{n}{2n+1}2^{-\left(\frac{1}{n}+1\right)}S^{\frac{1}{n}-1}\,h^{2+\frac{1}{n}}\,\bar{p}_x\right) = \left[K^{-\frac{1}{n}}\frac{n}{2n+1}2^{-\frac{1}{n}}S^{\frac{1}{n}-1}\,\frac{h^{2+\frac{1}{n}}}{W}p_z\right]_{z=\frac{1}{2}W}, \quad \textbf{3-9}$$

where the average pressure is that defined in (2-11). Equation (2-12) is used to relate the pressure gradient at the wheel edge to the average pressure $\bar{p}$. For the length scale Δ in the dimensional analysis, I again use $\Delta = C\sqrt{Rh_0}$, where the adjustable parameter C has to be re-calibrated by the experiments. Hence

$$\frac{\partial}{\partial x}\left(Uh - K^{-\frac{1}{n}}\frac{n}{2n+1}2^{-\left(\frac{1}{n}+1\right)}S^{\frac{1}{n}-1}\,h^{2+\frac{1}{n}}\,\bar{p}_x\right) = K^{-\frac{1}{n}}\frac{n}{2n+1}2^{-\frac{1}{n}}S^{\frac{1}{n}-1}\,\frac{h^{2+\frac{1}{n}}}{\mathrm{W}\Delta}\,\bar{p}. \tag{3-10}$$

For sufficiently wide wheels, the right-hand side of (3-10) becomes zero, *i.e.*, no side flux. The boundary conditions for bow wave and the meniscus are those specified in equations (2-15), (2-16), and (2-17). I apply the same approximation for p_z in S as was described in Chapter 2. With this assumption, (3-10) becomes

$$\frac{\partial}{\partial x}\left(Uh - K^{-\frac{1}{n}}\frac{n}{2n+1}2^{-\left(\frac{1}{n}+1\right)}|p_x|^{\frac{1}{n}-1}\,h^{2+\frac{1}{n}}\,\bar{p}_x\right) = K^{-\frac{1}{n}}\frac{n}{2n+1}2^{-\frac{1}{n}}\sqrt{p_x^2+\left(\frac{\bar{p}}{\Delta}\right)^2}^{\frac{1}{n}-1}\,\frac{h^{2+\frac{1}{n}}}{\mathrm{W}\Delta}\,\bar{p}. \tag{3-11}$$

Referring to (3-8), the lubrication pressure scales as $K\left(\frac{U}{h_0}\right)^n\left(\frac{R}{h_0}\right)^{1/2}$, but at the same time depends on the length scale ratio $\mathcal{R}$ and the dimensionless incoming flux λ (both parameters were introduced in §2.4.3). The global load balance (2-17) then suggests a scaling for the minimum gap as

$$h_0 \sim U\left(\frac{KRW}{L}\right)^{\frac{1}{n}} I(\mathcal{R},\lambda)^{\frac{1}{n}}, \tag{3-12}$$

where I is the dimensionless load, incorporating the effects of the side flux and the bow wave position, that was discussed in detail in §2.4.3.

3.4.3 Calibration of C

The measured gap sizes are used to calibrate the model and then pressure traces are tested against the experiments. The values of C for each test was obtained so that the predicted gap size matches

the measured one, and those values are plotted in Figure 3-12(a) versus the non-dimensional width $W/\sqrt{Rh_0}$ for both non-Newtonian samples. Note that the experiments are only conducted for the wide wheel ($W = 20\ mm$), equivalent to region II in Figure 2-18. The scatter of the data (except for experiments with high shear rates) is insignificant and, hence, the experiments support the parametrization of the model. For the 0.5% xanthan solution ($n = 0.56$), only the experiments with the lower range of the shear rates (open blue circles) are used to calibrate the model.

The free constant C depends on the flow index n, and the dependence is plotted in Figure 3-12(b), including C for the Newtonian fluid ($n = 1$). The smaller values of C for fluids with $n < 1$ are also consistent with the measured pressure profiles (see Figure 3-10(b)), where the length over which the pressure drops laterally is smaller for the shear-thinning fluids. In addition, smaller C in the model implies a higher degree of side flux for the shear-thinning fluids, which is also consistent with the observations presented in Figure 3-8(b). Figure 3-12(a) also shows that the fitted C for the low shear rate experiments (open blue circles) with the 0.5% Xanthan gum solution is markedly lower than for the high shear rate experiments (solid blue circles), which provides further evidence of a breakdown in the power law behavior of this fluid at high shear rates.

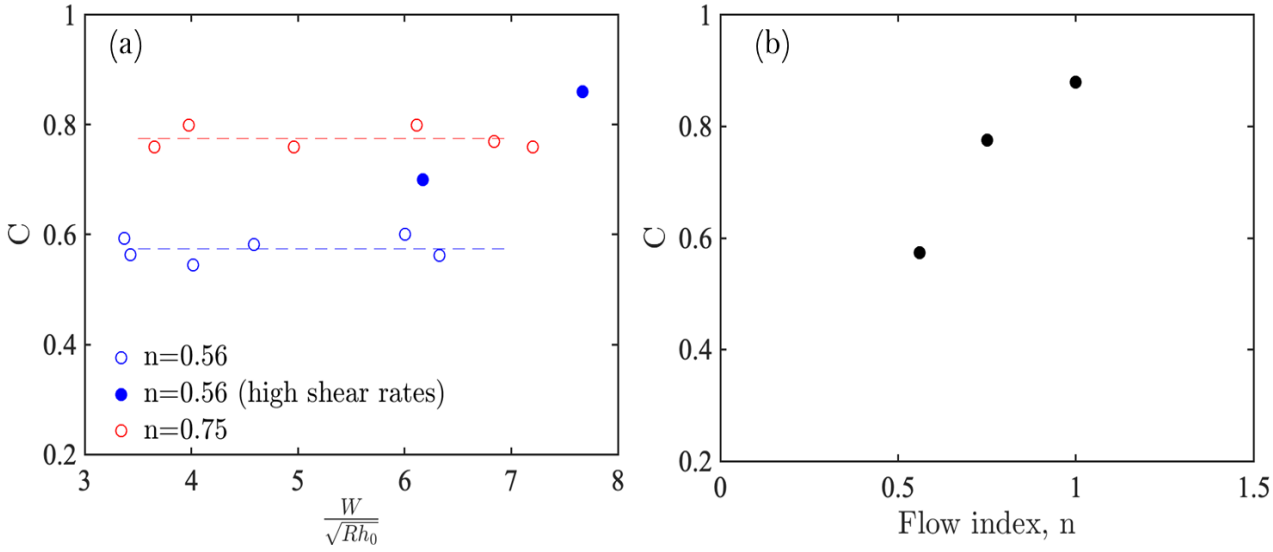

Figure 3-12 (a) Evaluation of the constant C as a function of the ratio $\frac{W}{\sqrt{Rh_0}}$ for glycerin solutions with 0.25% xanthan (n=0.75) and with 0.5% xanthan (n=0.56), (b) averaged fitted C versus the power-law index. The wheel width is w=20 mm.

3.4.4 Comparison of theory and experiments

Figure 3-13, using the calibrated value of C, compares the measured and predicted gap sizes for both samples, where agreement (except for high shear rates data points) is observed. The general agreement is expected as the model is calibrated by the measurements of the gap size.

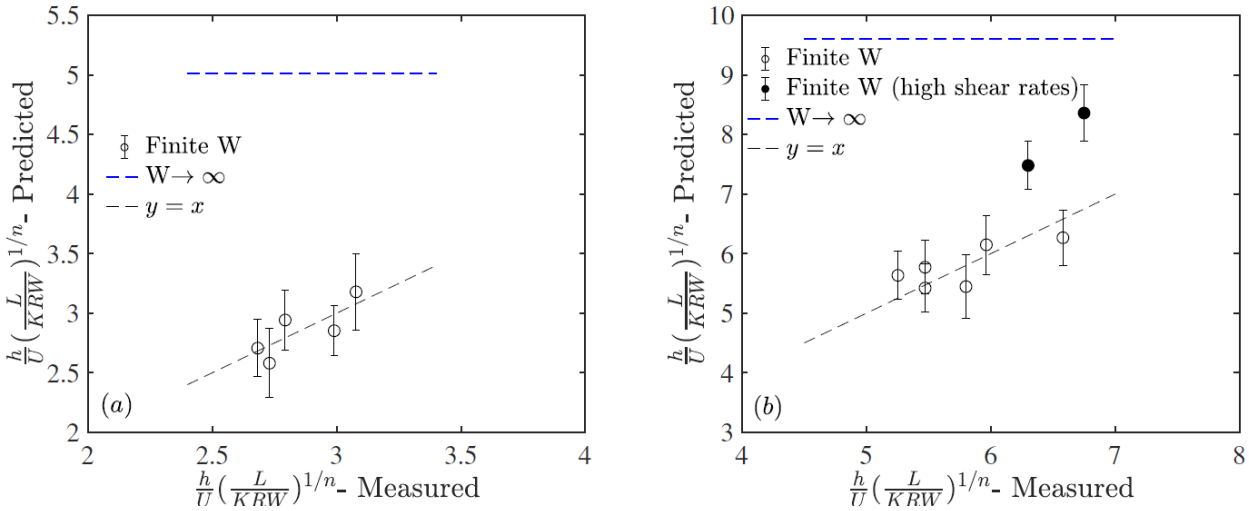

Figure 3-13 Scaled gap size predicted by the model (for both cases: finite W and infinitely wide wheel) plotted against those measured experimentally for (a) 0.25% xanthan and (b) 0.5% xanthan. For an infinitely wide wheel, the RHS of (3-10) disappears and the problem becomes pure two-dimensional.

A more demanding test of the model is the measured pressure profiles. Measured and predicted average pressure profiles $\bar{p}$ are compared in Figure 3-14. For the Newtonian fluid tested in §3.3.2 (panel(a)), the same level of agreement is observed with the rest of the Newtonian measurements that were discussed in chapter 2. For shear-thinning samples (panels(b) and (c)), the power-law model underpredicts the peak pressure by about 14%, and there is a commensurate mismatch in the wetted length. For this particular experimental condition, the model predicts the bow wave position $x_l = -13.0\,mm$ for 0.5% xanthan, whereas it was measured to be $x_l = -10.8\,mm$ in Figure 3-11(b). To demonstrate that the proposed non-Newtonian model has advantages over the Newtonian model, I can assume that the fluid is Newtonian in the model and find the Newtonian viscosity that produces the same minimum gap under identical speed and load (this is only for the sake of the theoretical pressure profiles and is a different approach than that taken in §3.3.2 to match a Newtonian fluid experimentally). I can then use that viscosity to predict the fluid pressure from the Newtonian theory (labelled as "Equivalent Newtonian model" in Figure

3-14). As is apparent, this simplified theory is significantly less predictive than the non-Newtonian model for both the wetted length and peak pressure.

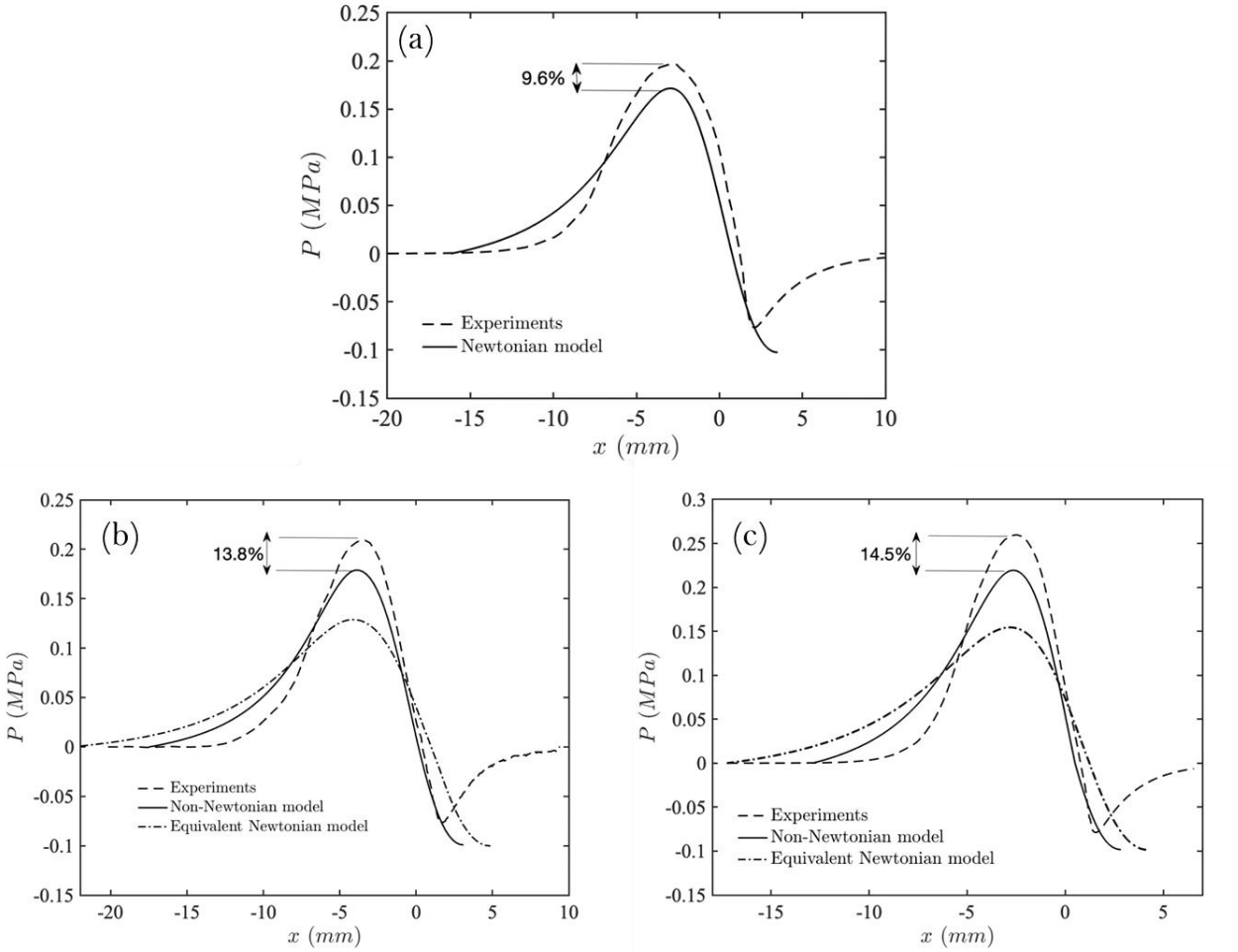

Figure 3-14 Comparisons of the experimental and theoretical pressure profiles for (a) Newtonian fluid (mixture of 68% silicone oil with μ=0.5 Pa·s and 32% silicone oil with μ=8.7 Pa·s), (b) glycerin with 0.25% xanthan and (c) glycerin with 0.5% xanthan. Test conditions: U=0.8 m/s, L/W=1.2 kN/m, W=20 mm.

Lastly, to further illustrate the differences between the fluid behaviors at high and low shear rates, I compare the pressure profile prediction with experiment for a high shear rate case in Figure 3-15. As apparent in this figure, relative to the low shear rate cases, the opposite trend between the model and the experiment is observed, *i.e.* smaller predicted wetted length and larger predicted

peak pressure, which clearly contradicts the direct high-speed imaging of the bow wave position. The difference in peak pressure is also substantially larger (~34%) compared to the previous trials at low shear rate.

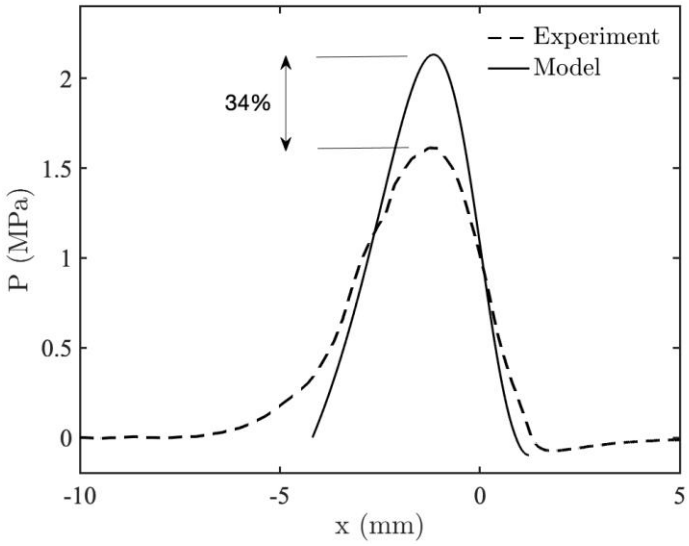

Figure 3-15 Comparison of the experimental and theoretical pressure profiles for the high shear rate (under high loading) experiment. Test fluid is glycerin with 0.5% xanthan and other test conditions are: U=3 m/s, L/W=5.5 kN/m, W=20 mm.

3.5 Conclusions

In this chapter, I presented the experimental and analytical explorations of a cylinder rolling over a pool of shear thinning fluid. The test fluids were mixtures of pure glycerin with 0.25% and 0.5% xanthan gum, both of which showed power-law behavior in almost the full range of the rheological measurements. I showed that although some qualitative features of the lubricated flow are similar to the Newtonian fluid (such as interface profiles at the upstream and downstream free surfaces, failure of wheel liftoff at low speeds, and the printed pattern at higher interactions), quantitative features are different. When compared with the Newtonian fluid under identical speed, load and

minimum gap, shear-thinning fluids have a shorter wetted length and consequently a higher peak pressure. Flux to the sides of the wheel increases for the shear-thinning fluid, leading to a shorter ploughing length l_p. Also, unlike Newtonian fluids, the load dependence of the gap size is non-linear for shear-thinning fluids ($h_0 \sim L^{\frac{1}{n}}$). For both types of the fluids, the dependence on the speed is linear.

The theoretical model, first presented in Chapter 2, was extended to the power-law fluids to account for shear-dependent viscosity. The model posits that the flow under the wheel from the bow wave to the meniscus is a lubrication flow and includes a free constant, which is a function of the flow index that needs to be calibrated by the experiments. With the fitted free constant, the model can successfully predict the peak fluid pressure, minimum gap, and the bow wave position to within about 15%. However, the model fails to explain the observations at high shear rates ($\dot{\gamma} > 2.5 \times 10^4\ s^{-1}$), which suggests that the power-law behavior is likely violated by the test fluids at elevated shear rates.

It is also worth mentioning that the simple shear-thinning fluids used in this chapter are different than friction modifiers used in practice (they will be explored in the next chapter). As discussed earlier, FMs are complex fluids showing viscoelasticity and often contain solid particles. Suggested by the results from this chapter, FM's rheology becomes even more complicated by the high shear rates at the wheel/rail interface. Thus, conducting rheological measurements at high shear rates would really aid the industry in formulating their products.

Chapter 4: Carrydown of Liquid Friction Modifier- Industrial Application

4.1 Introduction

In this chapter, I study carrydown of a commercial liquid friction modifier. Carrydown is a process by which liquid is conveyed along the track via splitting between the train wheel and the track. Carrydown is not fully understood yet and the literature gaps were discussed in Section 1.2.6. Motivated by those gaps, this research aims to enhance our understanding of the carrydown mechanism. The chapter is comprised of two parts: laboratory studies on a novel apparatus and field trials on an operating track. In Section 4.2 I describe the methodology for both types of experiments, and in Section 4.3 I present the results and draw parallels between the laboratory studies and the field trials. Finally, in Section 4.4 I summarize the key findings.

4.2 Methodology

4.2.1 Lab experiments

A custom rig was developed at the laboratory scale to understand the LFM behavior at the wheel-rail interface and the mechanism for subsequent carrydown. The details of the apparatus are provided in Section 2.2.1 and is shown schematically in Figure 2-2. The apparatus was not intended to accurately mimic all aspects of the full-scale wheel-rail contact, but rather represents a simplified geometry that is governed by the same physics. It consists of a highly modified woodworking band saw, chosen because the band saw provides a long and continuous moving surface. The band saw blade represents the top surface of the rail. The blade is made of carbon steel and is 0.9 mm thick. To reduce the light reflection from the surface of the band-saw blade (which is a requirement for the film thickness measurement technique, described next), the blade

was chemically treated with black oxide. The treated blade has an RMS roughness of ~850 nm (measured with an optical profilometer), close to the railhead typical roughness of 1 μm [122].

The wheel design was based on the work conducted by Naeimi et al. [123], where they showed that a 1/5 scale train wheel under the scaled loading could produce a contact pressure comparable to that at the wheel-rail interface. The wheel diameter is 0.2 m (roughly 1/5 of the actual wheel diameter). The wheel was driven by a separate motor than the blade to allow for independent speed control over the blade and the wheel, although in the tests described here the two surface speeds are the same (i.e., there is no creepage). Two magnetic Hall Effect sensors were used to measure the speed of the blade and the wheel. A normal force was applied to the wheel by means of pneumatic air cylinders that are controlled by fast-acting solenoid valves. A backing wheel, which spins freely on its axle, was mounted opposite the driven wheel behind the blade, and was present to prevent deflection of the blade under the applied normal load. Both wheels were mounted on a linear rail guide to ensure smooth and accurate activation. A 12 kN load cell measured the normal force at the wheel-rail contact patch. The instantaneous gap size between the wheel and the rail was measured using a proximity sensor (Baumer #OM20-P0026.HH.YIN). A high-speed camera (Phantom V.12, with a resolution of 512×512 pixels, and frame rates of 2000-5000 fps) was used to image the LFM from the side, as the liquid moves through the nip and splits at the meniscus. The flow was backlit with a 6700 lumen LED light source.

The wheel and rail geometries did not match the commercial geometries in some regards. The blade was flat, unlike the crowned cross-section of a railhead [124]. Three wheels, which approximate railroad wheels, were fabricated from mild steel. One wheel has no crowning (i.e., it is a simple cylinder), one has a constant crowning radius of $R_c = 200\ mm$, and one wheel has a constant crowning radius of $R_c = 400\ mm$. These values of crowning radius are comparable to

what has been measured in the field. The cylindrical wheel has the width W=10 mm (to approximately match the width of the train wheel running band) and the crowned wheels have the width W=20 mm. For the cylindrical wheel, the apparatus can generate wheel-rail contact pressures of up to ~1 GPa (based on the Hertzian contact model for a cylinder on a substrate). Partial slip was not introduced to the testing due to experimental difficulties although slip may significantly affect the rolling process. The wheel-track cross sections for both the laboratory apparatus and commercial trains are compared in Figure 4-1 to show key differences in wheel and rail geometries.

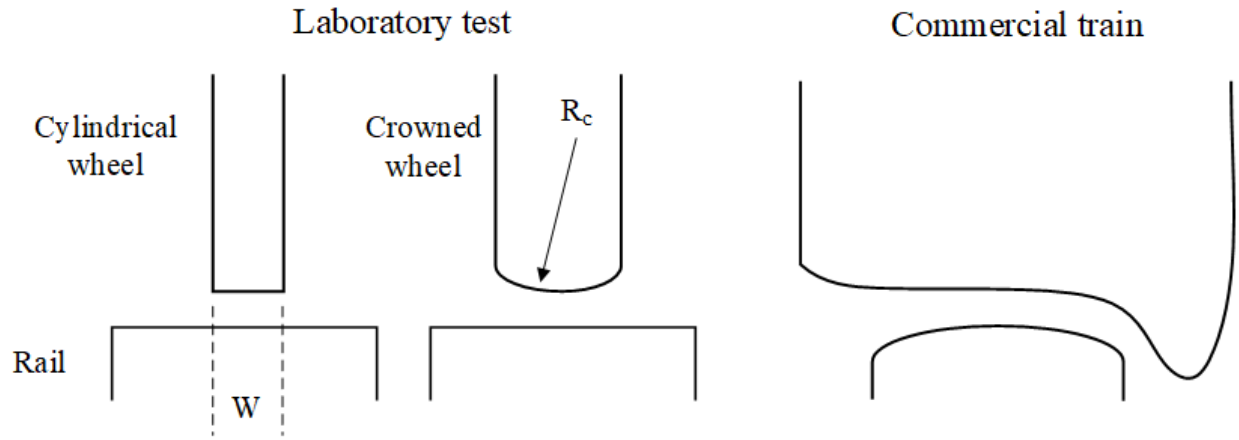

Figure 4-1 Cross sections of the wheel/rail interface in both laboratory and field settings. The schematic is not to scale.

KELTRACK (a water-based LFM) was the test fluid. It is a non-Newtonian fluid exhibiting shear thinning and elastic behavior with the measured viscosity of $\mu = 5.1\ Pa \cdot s$ at a shear rate $\dot{\gamma} = 100\frac{1}{s}$. At the start of an experiment, a pool of KELTRACK with a known thickness and length (comparable to those used in practice) was applied to the blade with an initial pool length L_0 and an initial pool depth h_{in}. Then, the operating pressure and the speeds of the wheel and blade were set. Once a photo diode sensor detected a marker on the blade, the pneumatic cylinders were

activated, driving the wheel into contact with the blade upstream of the pool of liquid. The wheel then rolls over the liquid pool and picks up some of the liquid as it passes. One circumference downstream from the original pool, the liquid adhering to the wheel passes into the nip between the wheel and the blade, and the process repeats. The large length of the blade allowed six wheel-rail interactions before the wheel again approaches the initial pool location. The wheel and the blade were run at a maximum speed of ~30 km/h, somewhat lower than typical freight train speeds. Once the experiment was complete, to evaluate the carrydown performance, the optical technique (described in Section 2.2.3) was employed to measure the residual fluid thickness on the for all wheel-blade interactions.

4.2.2 Field experiments

Field experiments were performed on a track located in Delta, BC, Canada. The track was limited to freight and maintenance trains. A wayside unit (Figure 4-2) was installed on a tangent track located about 500 m upstream of the curved track. An applicator bar (visible in Figure 4-2(b) and (c)) was used to distribute the LFM on the railhead. The wayside unit was equipped with a magnetic sensor to detect train wheels. The sensor counted the number of passing axles, and for every seven axles the unit pumped 2.8 mL of LFM onto the track, consistent with the supplier recommendations. The same dyed LFM used in the laboratory experiments was also used in the field experiments. An overview of the track along with the relevant distances from the application unit are presented in Figure 4-3.

Figure 4-2 (a) Installed trackside application unit, (b) Distributed LFM on the rail utilizing two applicator bars, (c) Application site after the passage of the train.

Experiments were conducted in two trials. In the first trial, Phase I, the application of dyed LFM coincided with the start of the trial. In other words, a single train with 628 axles carried the product downstream prior to measurement of carrydown. In the second trial, Phase II, the track was pre-conditioned with LFM for several days before measurement of LFM on the track. During the conditioning period, 33,000 or 40,000 train axles passed over the LFM pool, westbound and eastbound, respectively. A handheld portable tribometer (Salient Systems) was used to measure the coefficient of friction along the track. The experiment phases are summarized in Table 4-1. I only investigated the LFM coverage on the rail, as it was not possible to stop the train to measure LFM adhering to the wheels.

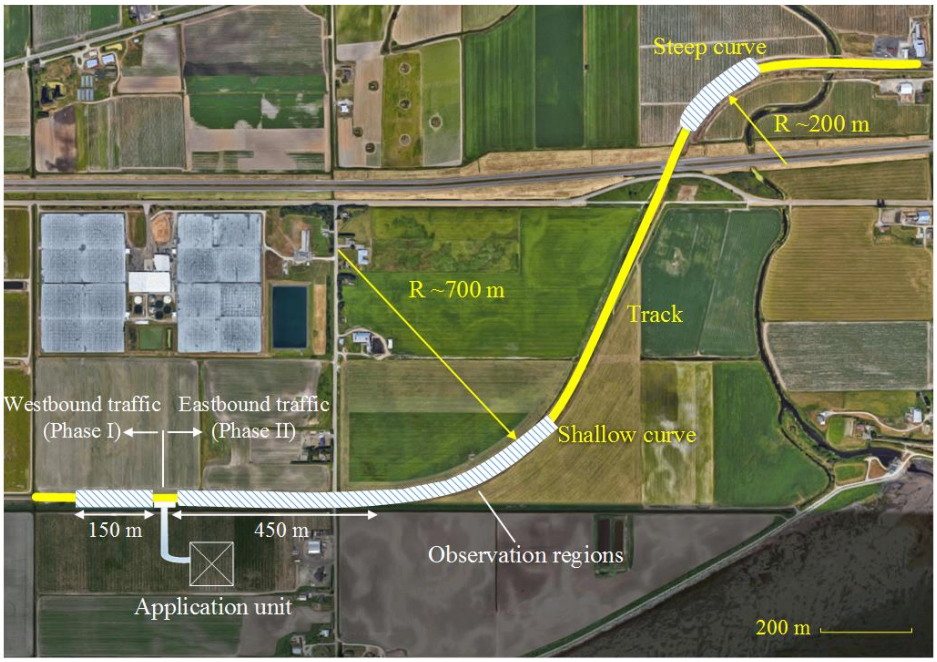

Figure 4-3 A top view of the studied track showing the location of the application unit, different phases of the trial, and the relevant distances. The shallow curve starts at about 450 m from the application site and the steep curve extends to about 2 km downstream. The observation regions for both phases are marked in the image. Image source: google earth, 33MF+V7 Delta, British Columbia (49°05'05.0"N 122°55'36.5"W). http://www.earth.google.com [June 18, 2021].

Table 4-1 Summary of the test details

	Location	Conditioning	Object	Distance
Phase I	Delta, BC	None and 33000 axles	Tangent track	~150 m
Phase II	Delta, BC	40000 axles	Tangent and curved tracks	~ 2100 m

Imaging of the LFM on the tracks after the passage of the train was done using a portable version of the experimental LIF apparatus used in the laboratory. The portable setup (Figure 4-4) was clamped to the rail and imaged the track at different distances downstream of the application

unit. Since no electricity was available on site, two car batteries, coupled with an inverter, were used to power the laser, camera, and computer. For the LIF setup to work properly, one needs to eliminate the ambient light, as it would otherwise interfere with the collected LIF signal. Accordingly, the whole optical setup was fully enclosed and covered by a dark cloth.

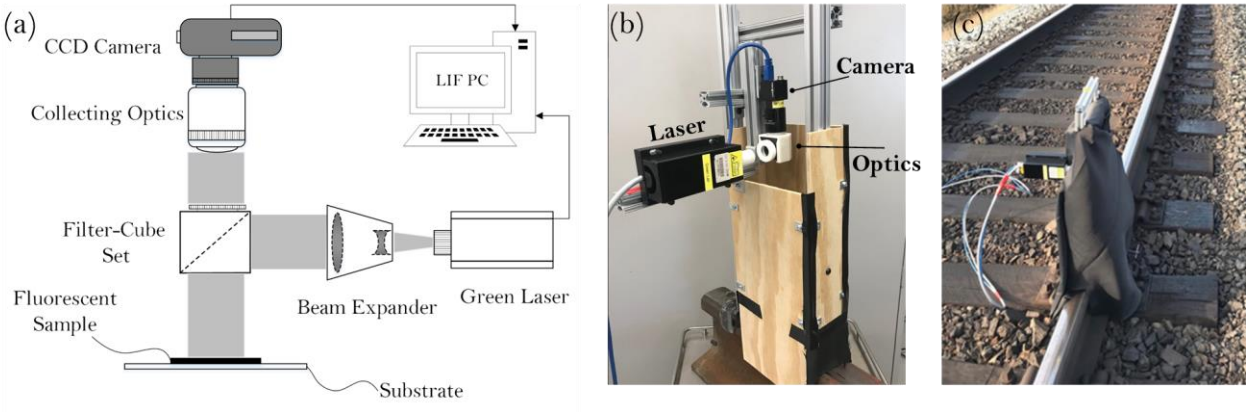

Figure 4-4 (a) Schematic of the LIF setup used to measure the thickness of the carrydown LFM. (b) and (c) The portable LIF setup built to measure the LFM thickness on the rail.

4.3 Results and discussions

4.3.1 Lab experiments

First, I present results for the cylindrical wheel. I refer to the location where the wheel rolls over the original LFM pool as Interaction One. Interactions Two to Five may show carrydown from LFM that adhered to the wheel during Interaction One. Throughout this chapter, the Hertzian contact model is used to estimate the wheel-rail contact pressures. For a very lightly loaded wheel, perhaps comparable to an empty freight car, with a Hertzian contact pressure $p = 46\,MPa$, the LFM forms a lubrication film under the wheel (similar to Chapters 2 and 3). The resulting film thickness contours are plotted in Figure 4-5, showing the deposited KELTRACK on the rail after the passage of the wheel for initial contact (a) and subsequent carrydown (b). In Figure 4-5(a), the

initial pool depth, 500 µm, far exceeds the saturation level of the LIF detection system, and hence the entire pool outside the contact band is shown with a depth of 100 µm. For lightly loaded wheels, the hydrodynamic pressure generated within the fluid is sufficient to balance the applied load. The lubrication film carries down the track for the subsequent wheel-rail interactions (Figure 4-5(b)). The dynamics governing the lubrication film formation (which only occurs at comparatively low contact pressures) are quite different from LFM interaction for a heavily loaded train, and were explored in detail in Chapters 2 and 3.

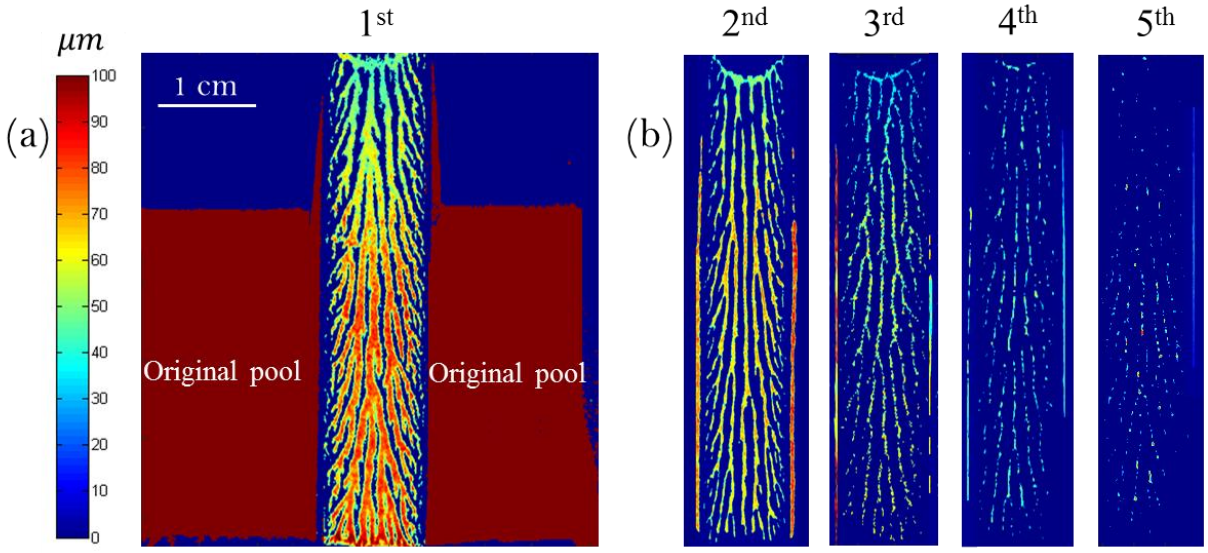

Figure 4-5 An example of the KELTRACK lubrication film formation in the wheel-rail contact band under a very light applied load to the cylindrical wheel. In (a), we show Interaction One and in (b), we show the subsequent carrydown of this lubrication film (Interactions Two to Five) onto the rail after the wheel has made full revolutions downstream from the initial pool. The vertical axis is the direction of wheel motion (from bottom to top), and the horizontal axis is parallel to the wheel axle. The color map shows the liquid thickness in µm (signal is saturated in the untouched portion of the LFM pool in (a)). Test conditions are U=28.8 km/hr, load-to-width ratio L/W=9.2 kN/m (equivalent to Hertzian contact pressure of P=46 MPa), and W=1 cm. The initial pool length is L_0=4 cm, and the initial pool depth is h_{in}=500 µm.

Figure 4-6 shows similar contours but for test conditions comparable to those in the real application. As for the experiments in Figure 4-5, the initial pool depth ($500\ \mu m$) exceeds the saturation level of the LIF signal. In the contact band, it is evident that the maximum thickness of the LFM layer is less than the 3.4 μm (detection limit of the LIF system). The vast majority of the LFM originally located in the contact band therefore cannot withstand the high contact pressure and is squeezed out of the nip laterally, where some of it adheres to the edges of the wheel. It is also apparent that some LFM is plowed ahead of the wheel as the wheel rolls over the pool, resulting in the two thin wedges of LFM (labelled as "Edge liquid") extending downstream from the original pool. This edge liquid, in addition to the edge liquid picked up by the wheel as it passes through the original length of the pool, is carried forward on the rotating wheel and some of it redeposits on the blade during subsequent interactions (apparent as two distinctive stripes on either side of the running band in Figure 4-6(b)). The carried down liquid reduces in depth with each interaction, weakening the observed pattern.

I posit that a minuscule amount of LFM passes through the nip in the valleys between surface roughness features (the rail surface has an RMS roughness of ~850 nanometers). This scale is certainly below the detection limit of the measurement technique. To test this hypothesis, gravimetric measurements were performed. Aluminum strips were attached to the wheel and the blade, and the samples were collected before and after each wheel-rail interaction. Subsequently, the samples were weighed carefully using an accurate analytical balance. For Interaction Two, the gravimetric measurements consistently showed an increase in the strip mass of 0.29 ± 0.04 mg for both wheel and rail. The equivalent film thickness, which I am confident is not in the form of a continuous film, is on the order of ~520 nanometers. Therefore, the gravimetric measurements confirm a minuscule amount of LFM is present on the contact band that cannot be otherwise

detected by the LIF setup. In fact, in a separate test that was conducted at LB Foster Rail Technologies using the twin-disc apparatus, the friction was consistently lower than that of bare metal-to-metal contact up to 1000 disc rotations. However, the fluorescence signals were not detectable after approximately 100 rotations, providing additional evidence to support the hypothesis that amounts of LFM below the detection limit of LIF can still appreciably reduce friction.

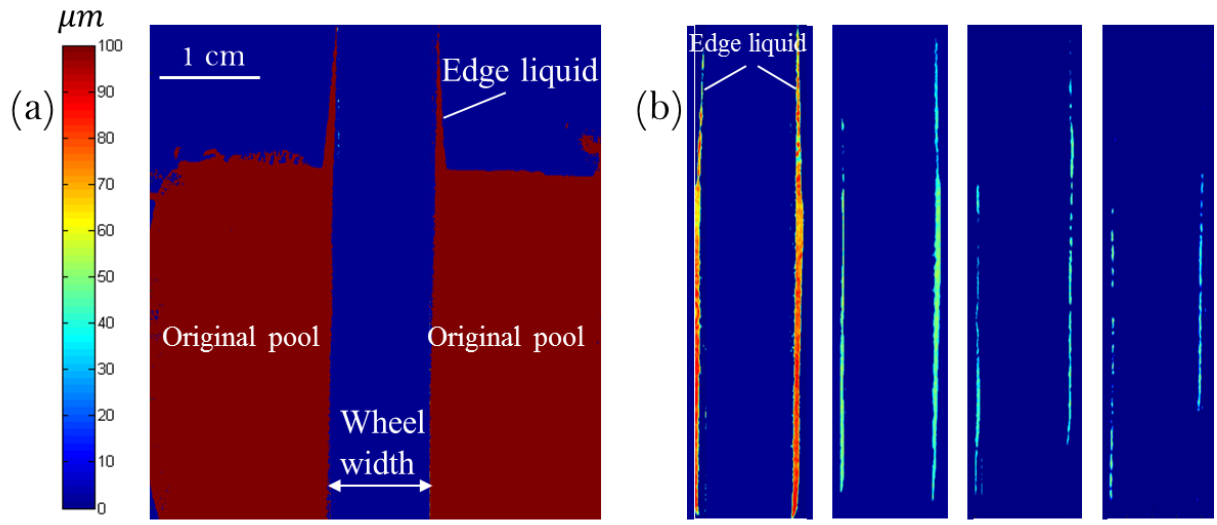

Figure 4-6 a) Product remaining on the blade after the first wheel-rail interaction, b) subsequent carrydown by the coated wheel. Test conditions are U=28.8 km/hr and load-to-width ratio L/W=450 kN/m (equivalent to Hertzian contact pressure of P=420 MPa). The initial pool length is L_0 =4 cm, and the initial pool depth is h_{in}=500 µm. The wheel width is W=10 mm.

Figure 4-7 displays side-view photographs captured by the high-speed camera, showing the film splitting between the side of the wheel and the rail. In (a), the LFM is initially picked up by the wheel, and in (b), the LFM is transferred back from the wheel to the rail on the next wheel revolution (Interaction Two), resulting in LFM carrydown. The images also show the formation, elongation and break-up of the fluid filaments as the film splits on the sides of the wheel.

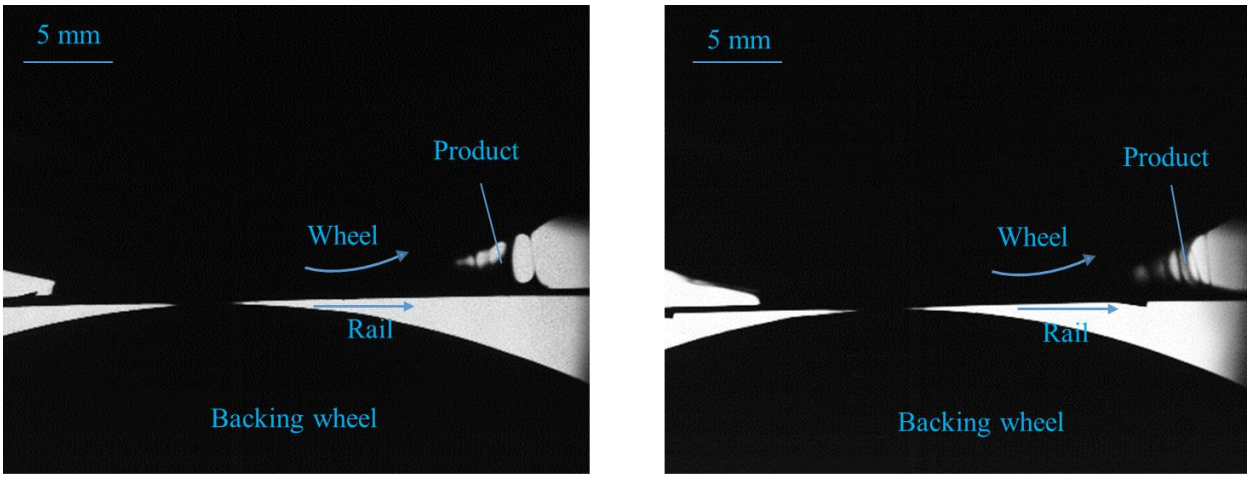

(a) Initial pickup (b) Subsequent carrydown

Figure 4-7 High-speed images of the film splitting behind the wheel. In (a), the product is picked up by the wheel, and in (b), the product is originally present on the wheel and is transferred back to the rail. Test conditions are U=28.8 km/hr, L/W=450 kN/m , L_0=4 cm, h_{in}=500 µm, and W=10 mm.

Figure 4-8 shows the track left by the passage through the LFM pool of crowned wheels of width 20 mm. In (a) and (b) I show the results for the crowned wheel with $R_c = 200\ mm$, and in (c) and (d) I show the results for the wheel with $R_c = 400\ mm$. These values of R_c correspond respectively to gap size increases of $250\ \mu m$ *and* $125\ \mu m$ from the wheel centerline to the outside edge. Similar to the case of the heavily loaded flat wheel (Figure 4-6), the images evidently show that there exists a contact band (with a width of ~4 mm) with dry contact between the wheel and blade for both crowned wheels. The experiments were repeated for different test conditions over a wide range of speeds (14.4 to 28.8 km/hr) and loads (9.2 to 450 kN/m), but in no case was a continuous film of LFM detectable across the entire wheel width observed. This contrasts with the case of uncambered wheels, for which wheel liftoff was observed at low loads (Figure 4-5).

The lateral distribution of LFM film thickness is plotted for various speed and loading cases in Figure 4-8(b) and (d). In this plot, film thicknesses are averaged in two steps. First, thicknesses

are averaged in the direction of wheel motion. The resulting thicknesses are then additionally averaged over stripes symmetrically located on either side of the wheel centerline; therefore, the abscissa goes from $z = 0$ (wheel centerline) to $z = 1\ cm$ (wheel edge) for these wheels of width W=2 cm. There is good agreement between the deposited film thickness and the dash-dot line representing half the gap size, implying that the liquid filling the gap between the wheel and blade splits approximately 50:50.

Within a distance of 2 mm on either side of the wheel centerline no LFM was detected. I conducted experiments with a higher tracer dye concentration (Figure 4-9) to explore this region. The higher concentration improved the detection limit to 1.3 μm, allowing for thinner films to be detected, although it resulted in a concurrent saturation of the fluorescence signals emitted from films deeper than $\sim 40\ \mu m$. As seen in the Figure 4-9 inset, the higher sensitivity permitted us to detect the thin films present close to the wheel centerline. To confirm the presence of LFM even closer to the wheel centerline, narrow aluminum strips (70×2 mm) were adhered to the wheel centerline. The strips were weighted with a precision balance before and after the wheel-rail interaction. The measurements revealed that, similar to the heavily loaded flat wheel, there is a 0.16 ± 0.05 mg increase, on average, in the mass of the aluminum strips, corresponding to an average film thickness of 800 nanometers (comparable to the blade surface roughness).

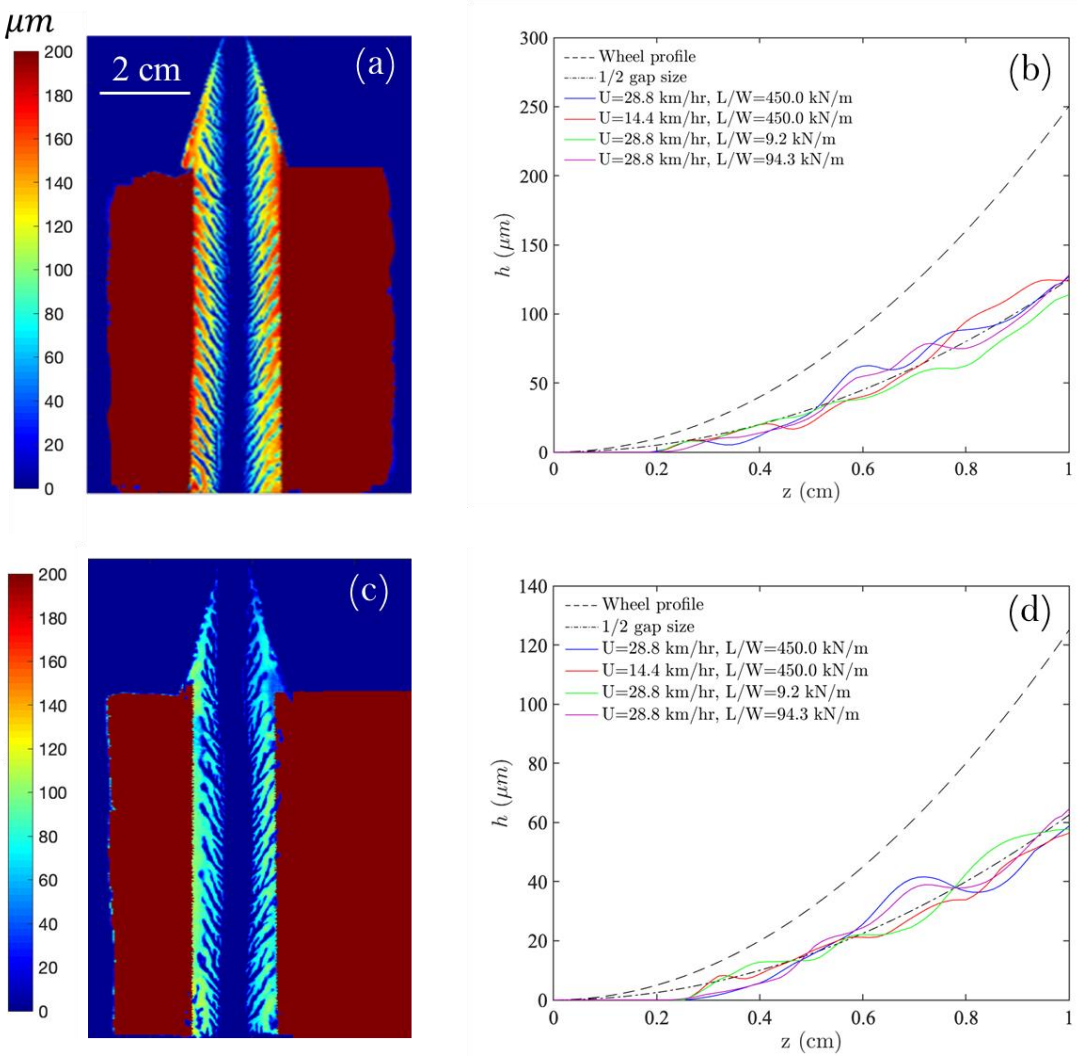

Figure 4-8 a) A typical example of the measured film on the rail after the passage of the crowned wheel of R_c=200 mm. b) Corresponding film thickness variations across the wheel width for R_c=200 mm. c). Deposited film on the rail for R_c=400 mm, and d) corresponding film thickness variations for R_c=400 mm. In (b) and (d), z=0 corresponds to the wheel centerline (a plane of symmetry), and z=1 cm corresponds to the wheel outside edge. The wheel widths are W=2 cm. ½ gap size is also marked on the graphs to show the expected film thickness if film splitting is symmetrical.

Carrydown was not detected from the crowned wheels, even with the high dye concentration. I posit that, since the film splits evenly between the wheel and blade, the LFM adhering to the wheel is insufficiently thick to bridge the gap to the blade, and hence there is no

transfer back to the blade. I also developed a lubrication-based theory for the crowned wheel rolling over a pool, however the model is of no use since the liftoff does not occur. This theory is detailed in Appendix B.

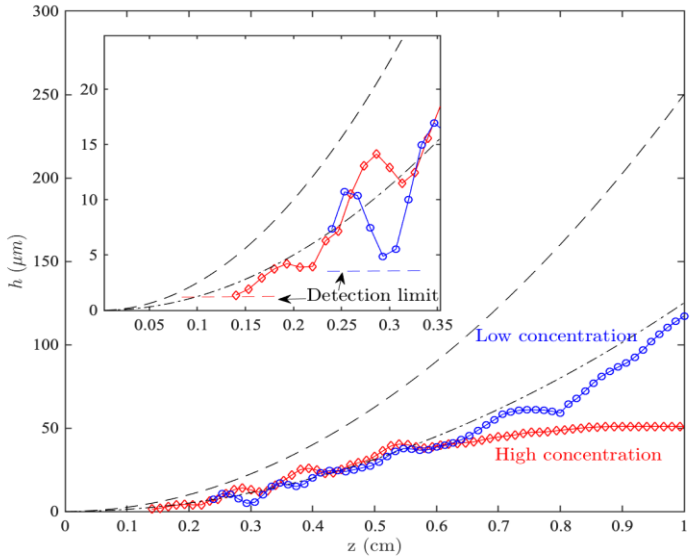

Figure 4-9 Lateral variation of film thickness measured at higher dye concentration. The higher dye concentration allows thinner films to be detected but causes fluorescence signal saturation for thicker films (> ~40 μm). Test conditions are U=28.8 km/hr, L/W=9.2 kN/m, and W=2 cm.

4.3.2 Field experiments

Phase I

In Phase I, the tangent track is studied up to 150 m from the application site. Figure 4-9 shows an example of the coated rail image (raw and post-processed), taken 9 m from the application unit. The rail was not pre-conditioned in this image, *i.e.* it was photographed immediately after application of LFM and passage of the first train. The approximate contact band is marked and it is clear that in most of the contact band the thickness of LFM is below the detection threshold of

the experimental technique (about 3 µm). Within the contact band the product is mostly visible in the grooves and cavities of the surface.

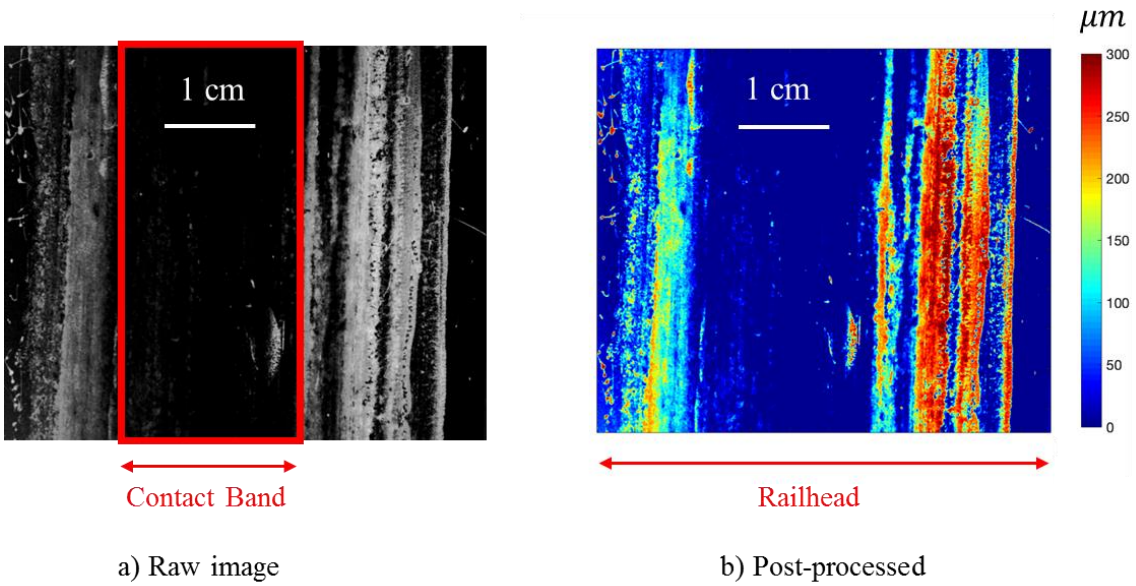

Figure 4-10 a) Raw LIF image of the deposited FM on the rail. b) Color map of the film thickness, where the signal intensity in a) is converted to the film thickness. The field side is on the left and the gauge side is on the right. The train is moving from bottom to top. Images were taken at 9 m from the application unit. The field of view is 6.5 × 6 cm.

Figure 4-11 displays coated rail images from various distances down the track. A repeating pattern is seen in all images: a minute amount of LFM on the contact band but significant carrydown of fluids from the edge of the contact band. I hypothesize that this carrydown on the (crowned) train wheels is due to modest changes in the location of the contact band, for example, due to lateral motion of the train or due to the variable geometry of different wheels. Figure 4-12 shows similar images as Figure 4-11, but for these tests the rail was pre-conditioned with approximately 33000 axles for three days. As expected, the measured films are thicker than for the clean rail experiments. However, the contact band is still mostly free of LFM.

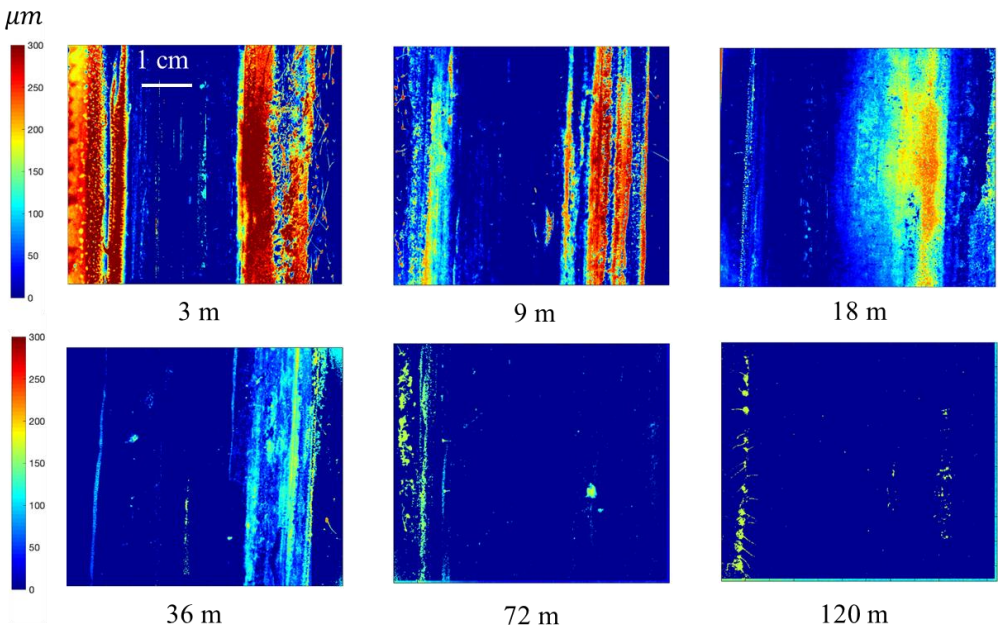

Figure 4-11 Deposited LFM on the rail at various distances from the TOR application unit, after the passage of a single train with 628 axles.

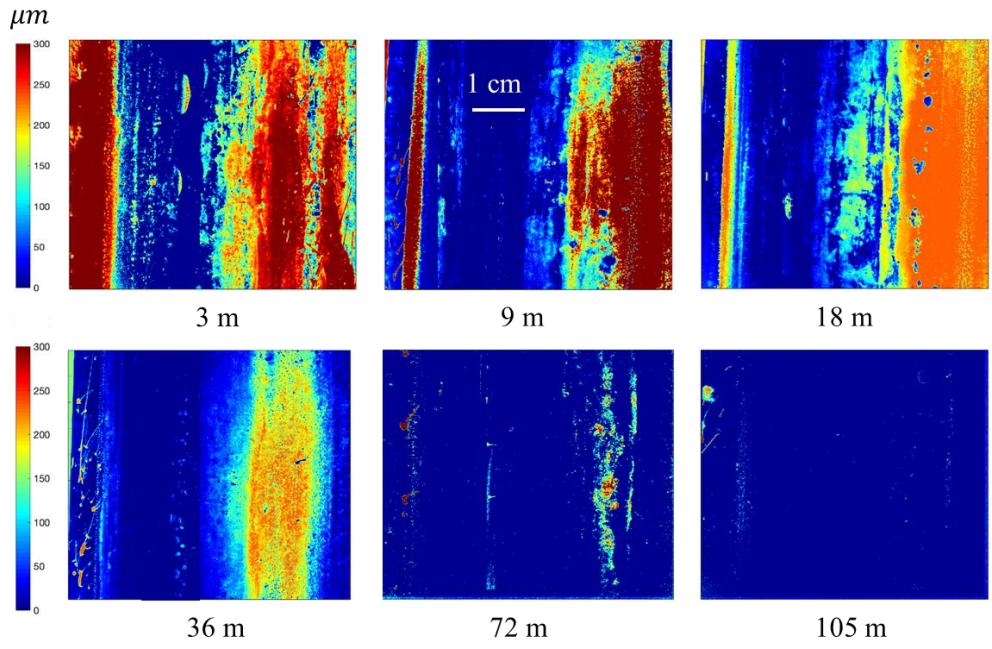

Figure 4-12 Deposited LFM on the rail at various distances from the TOR application unit. The rail was pre-conditioned for three days with 33000 wheel axles.

Figure 4-13 presents the average measured film thickness as a function of the distance from the application unit for both single train passage and pre-conditioned rails. With the measurement system, it is possible to differentiate the LFM on the contact band from other parts of the railhead. Averaged over the entire top of the rail (Figure 4-13(a)), the LFM is present over the entire scanning distance (~150 m, corresponding to the 47th wheel-rail interaction, assuming that the wheel diameter is 1 m). However, according to Figure 4-13(b), on the contact band, the carrydown distance is limited to approximately 100 m. When the rail is pre-conditioned, the FM is often detected for slightly longer distances, which is intuitive. The magnitude of the film thickness, and the approximate way in which it varies with distance from the application unit, are consistent with the findings of Khan et al.[118], who reported the deposited film thickness on the wheel contact band. However, it is unclear whether those authors studied the carrydown on a previously clean rail or a pre-conditioned rail.

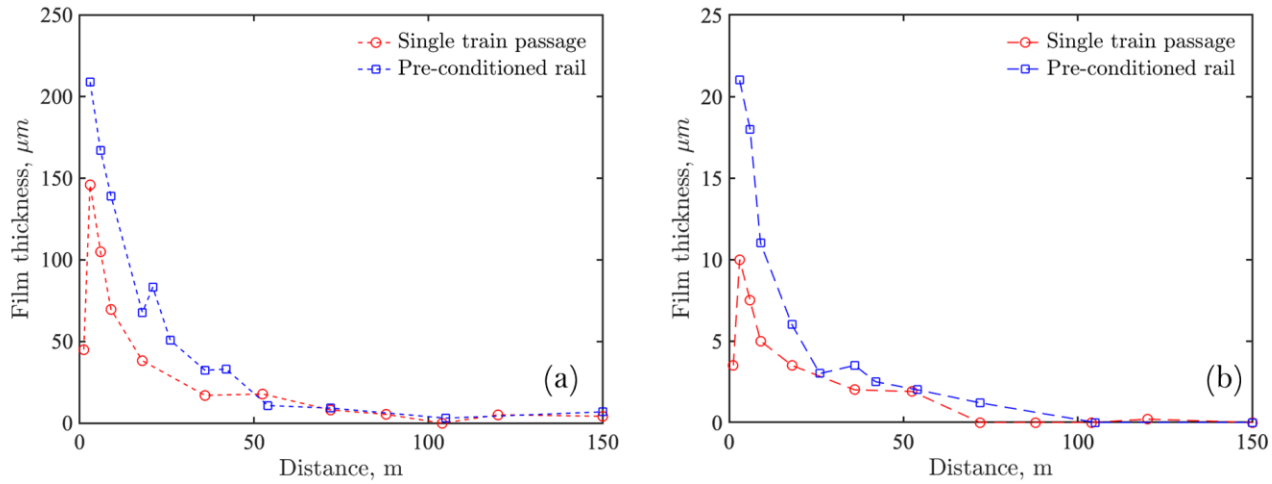

Figure 4-13 FM film thickness on the rail at various distances from the application unit averaged over (a) entire railhead and (b) contact band.

When interpreting these results, the detection limit of the measurement technique must be considered. For instance, after ~150 m on the track, an undetectable fluorescence signal does not

necessarily mean the complete absence of the LFM. As discussed above, the product may be present on the track if the thicknesses are below the detection limit.

Phase II

In this phase, the tangent and curved tracks were studied up to 2 km eastbound from the TOR application unit. The tangent track extends from the application unit to ~450 m downstream, followed by two curved tracks extending to approximately 2 km downstream. For all tests, the rail was pre-conditioned with approximately 40000 axles. Similar to Phase I, LFM was detected on the rail up to about 200 m from the TOR application unit. After that, no product was detectable on the rail until the end of the tangent section. Upon entering the curved section of the track, the LFM can again be measured on the railhead, which was a surprising finding. Some sample images of the LFM detected on the curved tracks are shown in Figure 4-14 and the LFM thicknesses are plotted in Figure 4-15. Although the average thickness of the LFM present on the curve is typically less than $15\ \mu m$, it is perhaps sufficient to reduce the lateral friction and wear, as claimed by some manufacturers. There is also some product on the wheel (not considered in this study), contributing to lower lateral forces and wear. Coefficients of friction (CoF) were also measured immediately downstream of the TOR application unit, and are plotted on the secondary axis in Figure 4-15. The trend in CoF is consistent with the measured thicknesses; it rises as film thickness decreases.

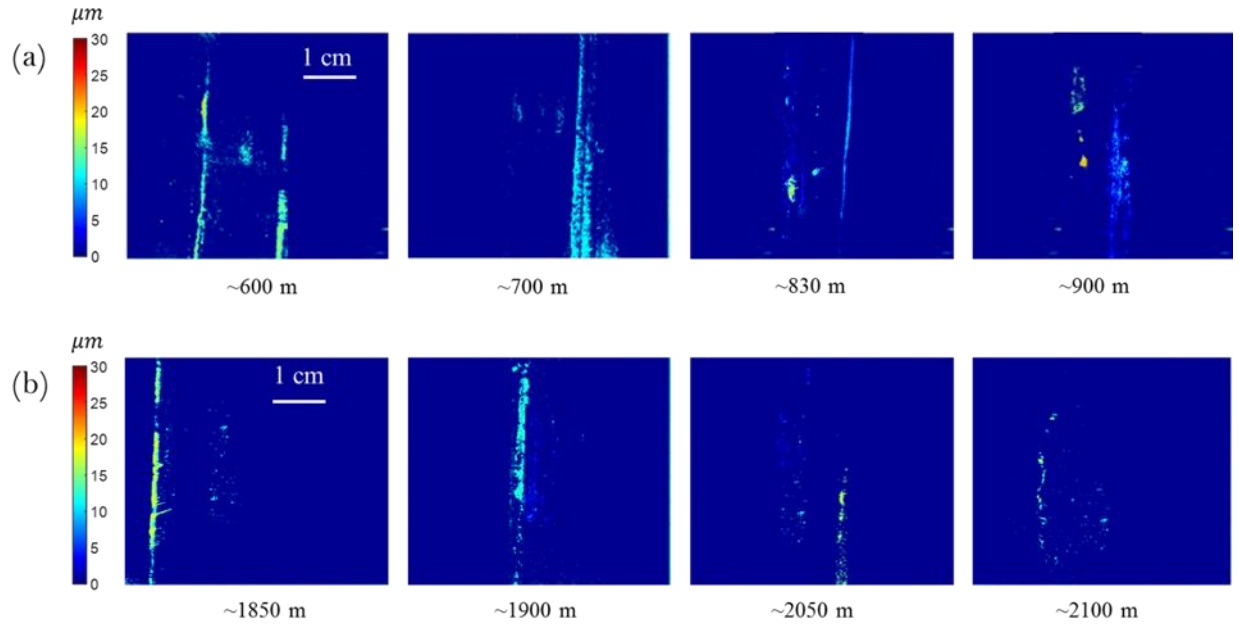

Figure 4-14 Images of LFM detected on (a) the shallow curve and (b) the steep curve for various downstream distances.

The surprising finding of LFM on the railhead on the curved track more than a kilometer downstream of where it is last observed on the tangent track requires an explanation. I hypothesize that as each wheel passes through the LFM pool at the application site, LFM is pressed out of the running band and adheres to the wheel adjacent to the running band. As the bogie hunts or sways on the tangent track, small excursions of the location of the running band on the wheel deposit the LFM onto the rail immediately adjacent to the running band. However, after a few hundred meters of motion all the LFM near the nominal running band that can be transferred to the track has transferred, and none remains on the wheel. However, when the bogie rounds a curve centrifugal forces combined with wheel conicity substantially change the running band location, bringing fresh LFM into contact with the track, where it is deposited. This hypothesis is consistent with the

experiments of Khan et al.[118], who showed that FM stays on the wheel for a distance longer than 3 km.

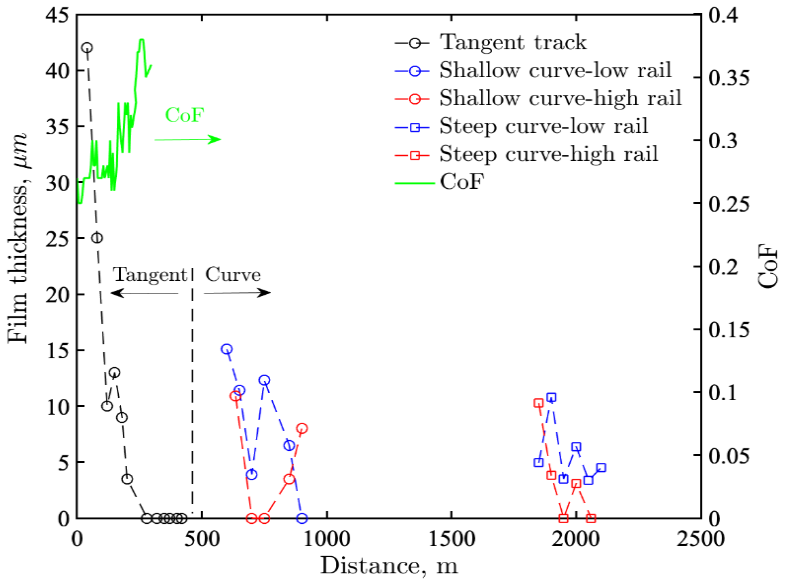

Figure 4-15 LFM film thickness (primary axis) and CoF (secondary axis) at various distances for both tangent and curved tracks. The vertical dashed line shows the approximate location where the curved track starts.

4.4 Conclusions

Laboratory and field experiments were carried out to study water-based TOR-LFM (KELTRACK) behavior at the wheel-rail interface and the associated carrydown. An optical technique, based on the fluorescence of a tracer dye, was used to scan the rail and generate a map of the film thickness. The key findings of this research are as follows:

(i) Both laboratory and field experiments clearly show that the LFM cannot withstand the characteristic high contact pressure at the wheel-rail interface to form a lubrication layer. Therefore, the LFM is pressed out of the contact band in locations where the wheel and rail are smooth. This liquid adheres to the non-contact surface of the wheel.

Careful gravimetric measurements show that unless there are significant surface irregularities, only a minute amount of LFM is carried through the nip. This LFM is believed to be carried in the valleys between surface roughness features.

(ii) At a significantly lower contact pressure, the hydrodynamic pressure developed in the fluid is sufficient to balance the wheel load. However, this low-pressure condition is not expected to occur in practice for loaded freight trains.

(iii) The LFM adhering to the non-contact surface of the wheel can subsequently be transferred to the track, if the location of the contact band on the wheel changes, e.g. due to hunting or sway.

(iv) LFM has been measured on the tangent track for a distance up to ~200 m from the application unit. On the contact band, however, this distance is limited to ~70 m.

(v) LFM can be detected in track curves up to 2 km from the application unit. The presence of LFM on curved track kilometers from the application unit is thought to be due to the lateral movement of the contact band as each bogie rounds a curve.

Chapter 5: Summary and Future Research Directions

In this chapter, I provide a summary of this thesis along with major contributions in §5.1. Then, I discuss some limitations of the research in §5.2. I close in §5.3 with some directions for the future research.

5.1 Summary

In this thesis, I provided experimental and analytical explorations of a cylinder rolling on a substrate through a pool of viscous fluid. A novel experimental apparatus is designed, with rail transport application in mind, reproducing some relevant physical conditions. A number of idealizations were introduced to better suit an interrogation of the underlying fluid mechanics. Experiments included measurement of the nip pressure and the gap between the cylinder and substrate, and observation of the liquid free surface (upstream bow wave and downstream meniscus). The film thickness left on the substrate after the passage of the wheel was measured using laser-induced fluorescence of the dyed liquid. Following conclusions were made:

- As the cylinder advances through the pool, some liquid is ploughed ahead of the cylinder and some is pushed laterally towards the sides of the cylinder. I showed that there are two possible outcomes of this interaction, depending on the operating conditions. In a preferred format, a lubrication film forms between the cylinder and the substrate. On the other hand, for low speeds or high loads, the cylinder remains in solid contact with the substrate. The thickness of the lubrication film rapidly rises to a constant value (which is a function of the wheel speed, fluid viscosity, applied load, wheel width, etc.) and then gradually drops when the end of the pool is reached, before abruptly dropping to zero. The steady gap between the two surfaces is independent of the pool depth and length.

- A short distance downstream from the nip the lubrication film splits evenly between the cylinder and substrate, and during the splitting process experiences a ribbing instability and may form beads on both the cylinder and substrate. As a result, the fluid adhering to the cylinder is non-uniformly distributed. If the pool length is less than the cylinder circumference the fluid adhering to the cylinder is convected by the cylinder rotation back into contact with the dry substrate. If there is sufficient adhered fluid a lubrication film once again forms between the cylinder and substrate, which is again well modeled by the theory. Conversely, for lesser amounts of adhered fluid no contiguous lubrication film is formed and a different form of interaction, which I label "printing", occurs.
- The steady state attained during the bulk of the interaction motivated the development of a model based on Reynolds lubrication theory. In Chapter 2, an approximation of the lubrication model for wheel passage over a Newtonian fluid is presented. The theory obviously cannot account for persistent solid-to-solid contact, predicting that the cylinder always lifts off the substrate. The model posits that the flow between the wheel and rail is a lubrication flow between a jump location upstream of the nip and a meniscus located downstream of the nip, and includes a "side flux" term that accounts for the lateral motion of liquid out of the gap. The appropriate form of the model is a function of $\frac{W}{\sqrt{Rh_0}}$. When $\frac{W}{\sqrt{Rh_0}} < 2.5$, the wheel width ($W$) is the relevant length scale describing the side flux; when $\frac{W}{\sqrt{Rh_0}} > 2.5$, the characteristic streamwise length, $\sqrt{Rh_0}$, is the relevant length scale. The model includes a single unknown constant (that differs for very thin versus moderate width wheels) that is fitted by comparison with the experiment. With the fitted constant, the 3D model was found to be in agreement with experiments. The model predicts the minimum gap, coating thickness, peak pressures, and bow

wave position to within root-mean-square errors of less than ten percent. However, the model consistently overpredicts the bow wave position by about 1.5 mm, on average. This is not surprising, however, in view of the simplistic approach I have taken in modeling the upstream boundary and given the complex fluid mechanics at the bow wave.

- In Chapter 3, I explored the problem for a non-Newtonian fluid. Mixtures of glycerin and xanthan gum at two concentrations were used as shear-thinning fluids. The measurements were taken for the wide wheel $W = 20\ mm$. I experimentally showed that some qualitative features of the lubricated flow are similar to those for Newtonian fluids. For instance, the cylinder may not lift off the substrate if the speed is low or the applied load is high. Printing interactions were also observed for the shear-thinning fluids. However, some quantitative measurements were different, confirming that the non-Newtonian effects are present. For instance, in a comparison with the Newtonian fluid under similar conditions, the pressure profiles, the wetted length, the peak pressure, and the ploughing length l_p were all different for the shear-thinning fluid. The wetted length becomes smaller for the shear-thinning fluids, which causes the peak pressure to increase to maintain the same load. The model is also modified for a power-law fluid by including a shear-sensitive viscosity term. Once the adjustable parameter in the model is calibrated against the experiments, the model can successfully predict the minimum gap, peak pressures and the bow wave position. However, this time the free constant is a function of the flow index n, in addition to $\frac{W}{\sqrt{Rh_0}}$. It was additionally observed that at high shear rates (estimated by U/h_0), the model fails to explain the observations, indicating that the fluid rheology deviated from power-law behavior at those high shear rates.

- In Chapter 4, I discussed the application of this research. First, I conducted a separate set of lab experiments for the conditions that closely resemble those at the wheel-rail interface, i.e., by increasing the applied load to the wheel and also using discs with a simple crowned lateral profile. Subsequently, I performed field experiments and drew parallels between the lab results and field experiments. The test liquid was a water-based TOR-LFM (KELTRACK). A portable version of the LIF setup was designed to scan the rail and generate a map of the film thickness. Both laboratory and field experiments clearly showed that the LFM cannot withstand the characteristic high contact pressure at the wheel-rail interface to form a lubrication layer. Therefore, the LFM was pressed out of the contact band in locations where the wheel and rail are smooth. This liquid adheres to the non-contact surface of the wheel. Careful gravimetric measurements showed that unless there are significant surface irregularities, only a minute amount of LFM was carried through the nip. This LFM is believed to be carried in the valleys between surface roughness features. LFM has been measured on the tangent track for a distance up to ~ 200 m from the application unit. On the contact band, however, this distance is limited to ~70 m. However, LFM can be detected in track curves up to 2 km from the application unit, which is consistent with the manufactures' claims. The presence of LFM on curved track kilometers from the application unit is thought to be due to the lateral movement of the contact band as each bogie rounds a curve.
- Some of the findings of this research can help the rail industry in terms of the product development and its application to the track. In Chapters 2 and 3, I showed how the thickness of the lubrication film (if any) varies with the operational conditions and fluid rheology and those information can be used to further optimize the application. For example, it may be beneficial to use a higher viscous fluid to ensure the wheel liftoff and the thicker resulting

lubrication film. In addition, I demonstrated in Chapter 4 that for freight trains, the wheel does not lift off from the rail due to heavy loading. However, I believe that in transit applications (where the applied load is significantly smaller), the product may act more efficiently. Furthermore, the printing phenomenon that was observed in the lab experiments for higher interactions may increase the carrydown distance. If the initial pool placed on the railhead is patterned, the fluid is being printed between the wheel and the rail from the beginning and that may lead to a longer carrydown distance.

Major Contributions of this research

The major findings of this research are summarized below:

- As a cylinder rolls over a pool of viscous fluid, the cylinder lifts off from the substrate if the speed is sufficiently high or the applied load on the cylinder is sufficiently light. In that case, a lubrication layer forms between the cylinder and the underlying substrate whose thickness increases with the speed and viscosity, but decreases with the load.
- A simple proposed analytical model is capable of offering insights into this lubricated flow by predicting the steady gap, fluid pressure, and the coating thickness once it is calibrated by the experiments. An adjustable parameter in the model differs for the thin wheels versus the wide wheels, and also depends on the flow index n.
- The results were evaluated for the industrial application of this research (rail transport), where a liquid product is applied to the wheel-rail interface. It was observed that the high pressure in the wheel-rail contact drives the fluid sideways and leaves no lubrication film behind. This side flux, although not beneficial on the tangent track, re-enters the contact band as the train rounds a curve and provides tribological benefits.

5.2 Limitations

A number of advancements have been made, as summarized above. Although, I should acknowledge some limitations in our theoretical and experimental studies. In what follows, I address the limitations of the current research:

- The smallest coating thickness that I could measure, using LIF technique, was about $2-3\ \mu m$, and that depends on the dye concentration, base liquid and optics. Whereas, the surface roughness scale is typically less than $1\ \mu m$. Therefore, the technique resolution has limited us to accurately confirm the presence of the fluid between the cylinder and the underlying substrate.
- In Chapter 3, I replaced the pneumatic air cylinders in the apparatus with the smaller ones to apply lighter loads to the system. This process was done to ensure that the fluid's shear rates are within or close to the range of rheological measurements. But I was limited on how low I could go with the load as the friction in the system required a minimum force before it starts to move the wheel on the linear guide. As a result, the shear rates for some of the experiments, although very close, are outside the rheological measurement range. This adds some challenges to this study as the exact fluid's rheology at those high shear rates is not known. That information is necessary for a solid comparison with the theoretical model.
- The theoretical models developed for both Newtonian and non-Newtonian models are approximations of the lubrication model, which adapt to include the lateral motion of the lubricated flow towards the edges of the cylinder. I was limited on having a full 3D solution because of the three-dimensional instabilities at the meniscus and complicated 3D structure of the fluid at the bow wave. The full 3D solution predicts the fluid behavior

in the lateral direction more accurately and eliminates the need of the calibration in the model.

- **Industrial applicability:** Although the laboratory experiments and theories presented here gave valuable insight into the fluid behavior between the wheel and the track, the findings cannot be generalized for the industrial application for the following reasons. First of all, the geometries of the commercial train and the track are very different than those studies in the lab, even though when the wheel was crowned. In addition, in practice, multiple wheels of the train contribute to the product carrydown along the track, whereas I only had one wheel interacting with a pool of liquid. Furthermore, the location of the train wheel contact band moves from one wheel to another or when the train rounds a curve, and that was very difficult to implement in the lab.

5.3 Future work

The work raises a number of questions that warrant further attention: first, at low speeds or high loads, the cylinder does not lift off from the substrate but maintains solid-to-solid contact. By contrast, the model predicts that lift off should always occur. Surprisingly, the condition for the failure of lift-off is not sensitive to the roughness of the surfaces, as in the lubrication of bearings (Lu & Khonsari [84]; Vogelpohl [83]). The theory presented in the current thesis pertains to the steady state region, so one might be able to develop an unsteady version of the lubrication model (focusing on the initial phase of the wheel lift off, phase I) which may explain the failure of lift-off under certain conditions. The unsteady theory may also help to understand the final touchdown of the wheel. Alternatively, it is believed that a full 3D solution to the lubrication equations may result in interesting findings, which can be used to justify the observations for the lift-off failure.

During the higher interactions, the filamentary pattern generated by the printer's instability is visibly reproduced after the passage of the cylinder. This indicates that the fluid pattern does not become squeezed back into a continuous film underneath the cylinder, but becomes printed on to the substrate without significant fluid flow. Our lubrication model does not apply to such printing interactions, which require a three-dimensional squeeze-flow analysis. I hypothesize that failure to liftoff is associated with the presence of the continuous liquid pool, as liftoff does occur with the discontinuous droplets or filaments present during printing. Therefore, additional experiments, with a patterned liquid pool initially placed on the wheel or the substrate, may aid in understanding the printing. Theoretically, the squeeze-flow analysis may also shed some light on the underlying fluid mechanics for the printing interactions.

In Chapter 3, I showed that the shear rates achieved in the experiments can be substantially larger than the range of a typical rheometer. The mismatch between the theory and the experiment indicates that the fluid's rheology is likely different for those high shear rates, however it would be interesting to have more solid evidences. This would be possible by carrying out the rheological measurements by a different rheometer, perhaps using microfluidic rheometry in which larger shear rates (by one or two order of magnitudes) can be achieved.

For the experiments with the cambered wheel, no liftoff was observed for the range of the speeds and loads tested. Yet, I developed a simple analytical model for the cambered wheel (see Appendix B). It would be interesting to confirm the model experimentally. This would be possible by conducting experiments under substantially lighter loads, and then compare the minimum gap, nip pressure, and the bow wave position.

As discussed several times in this thesis, there are key differences between the geometries of the wheel and rail used in the laboratory apparatus and the commercial train. For future research,

it would be helpful to make the apparatus more representative to the actual contact. In rail transport applications, the wheel has a specific crowned lateral profile and the track surface has a specific curvature, whereas the works presented here pertain to cylindrical wheels (or wheels with a simple crowned lateral profile) and a flat track. Inclusion of partial slip in the apparatus can also greatly enhance the representation of the actual contact.

In addition, it would be interesting to measure the spatial distribution of LFM coverage on the wheel, perhaps using LIF (the coated track was only imaged in the field). Performing field experiments for an oil-based FM would also aid in understanding the role of liquid evaporation on carrydown. It is believed that water-based LFMs dry faster on the wheel and consequently has a shorter carrydown distance. Conversely, the oil-based LFMs get carried down further along the track owing to slower drying properties.

The liquids applied to the track to modify frictional properties often exhibit elastic behavior and have yield stress. Carrying out additional experiments with fluids of different properties would elucidate the role of other non-Newtonian properties on this lubricated rolling, although it is believed that yield stress is probably irrelevant at these high shear rates. Experiments with PEO solutions might be a good direction to study elasticity. Likewise, incorporating a constitutive law, that includes elasticity, may complement the elastic experiments.

Bibliography

[1] J. Cotter *et al.*, "Top of Rail Friction Control : Reductions in Fuel and Greenhouse Gas Emissions," *Proc. Int. Heavy Haul Assoc. Conf. Rio Janeiro, June*, p. 7, 2005.

[2] J. Lundberg, M. Rantatalo, C. Wanhainen, and J. Casselgren, "Measurements of friction coefficients between rails lubricated with a friction modifier and the wheels of an IORE locomotive during real working conditions," *Wear*, vol. 324–325, pp. 109–117, 2015.

[3] T. M. Beagley, I. J. McEwen, and C. Pritchard, "Wheel/rail adhesion-Boundary lubrication by oily fluids," *Wear*, vol. 31, no. 1, pp. 77–88, 1975.

[4] X. Lu, J. Cotter, and D. T. Eadie, "Laboratory study of the tribological properties of friction modifier thin films for friction control at the wheel/rail interface," *Wear*, vol. 259, no. 7–12, pp. 1262–1269, 2005.

[5] H. Harrison, T. McCanney, and J. Cotter, "Recent developments in coefficient of friction measurements at the rail/wheel interface," *Wear*, vol. 253, no. 1–2, pp. 114–123, 2002.

[6] M. MATSUMOTO and M. MIWA, "Modeling an Optimal Track Maintenance Schedule in Consideration of Timing of Grinding and Tamping," *Q. Rep. RTRI*, vol. 58, no. 3, pp. 229–235, 2017.

[7] H. Rahmani and S. Green, "Particle-laden liquid jet impingement on a moving substrate," *AIChE J.*, vol. 63, no. 10, pp. 4673–4684, 2017.

[8] H. Rahmani, "Particle-laden liquid jet impingement on a moving substrate," *MASc Thesis, Univ. Br. Columbia*, 2017.

[9] R. Stock, L. Stanlake, C. Hardwick, M. Yu, D. Eadie, and R. Lewis, "Material concepts for top of rail friction management – Classification, characterisation and application," *Wear*, vol. 366–367, pp. 225–232, 2016.

[10] S. Abbasi, U. Olofsson, Y. Zhu, and U. Sellgren, "Pin-on-disc study of the effects of railway friction modifiers on airborne wear particles from wheel-rail contacts," *Tribol. Int.*, vol. 60, pp. 136–139, 2013.

[11] Morgan Hibbert, "Understanding the wheel/rail transfer mechanism in Liquid Friction Modifier carrydown," *MASc Thesis, Univ. Br. Columbia*, 2017.

[12] M. Harmon and R. Lewis, "Review of top of rail friction modifier tribology," *Tribol. - Mater. Surfaces Interfaces*, vol. 10, no. 3, pp. 150–162, 2016.

[13] L. Stanlake, "Film Splitting of Liquid Friction Modifier Formulations in the wheel-Rail Contact," 2012.

[14] J. Eggers, R. R. Kerswell, and T. Mullin, “Balancing a cylinder on a thin vertical layer of viscous fluid,” *Phys. Rev. E*, vol. 87, no. 6, pp. 5–8, 2013.

[15] T. Mullin, H. Ockendon, and J. R. Ockendon, “Levitation by thin viscous layers,” *J. Fluid Mech.*, vol. 888.

[16] M. P. Dalwadi, R. Cimpeanu, H. Ockendon, J. Ockendon, and T. Mullin, “Levitation of a cylinder by a thin viscous film,” *J. Fluid Mech.*, 2021.

[17] S. F. Kistler and P. M. Schweizer, *Liquid Film Coating: Scientific principles and their technological implocations*. 1997.

[18] D. J. Coyle, C. W. Macosko, and L. E. Scriven, “Film-splitting flows in forward roll coating,” *J. Fluid Mech.*, vol. 171, no. 17, pp. 183–207, 1986.

[19] Y. Greener and S. Middleman, “A Theory of Roll Coating,” *Polym. Eng. Sci.*, no. 1, pp. 1–10, 1975.

[20] K. Adachi, T. Tamura, and R. Nakamura, “Coating flows in a nip region and various critical phenomena,” *AIChE J.*, vol. 34, no. 3, pp. 456–464, 1988.

[21] J. Greener and S. Middleman, “Theoretical and experimental studies of the fluid dynamics of a two-roll coater,” *Ind. Eng. Chem. Fundam.*, vol. 15, no. 1, pp. 1–10, 1979.

[22] M. D. Savage, “Mathematical models for coating processes,” *J. Fluid Mech.*, vol. 117, pp. 443–455, 1982.

[23] M. D. Savage, “Mathematical model for the onset of ribbing,” *AIChE JournalE*, vol. 30, no. 6, pp. 999–1002, 1984.

[24] H. Benkreira, M. F. Edwards, and W. L. Wilkinson, “A semi-emperical model of the forward roll coating flow of Newtonian fluids,” *Chem. Eng. Sci.*, vol. 36, pp. 429–434, 1979.

[25] H. Benkreira, M. F. Edwards, and W. L. Wilkinson, “Roll coating of purely viscous liquids,” *Chem. Eng. Sci.*, vol. 36, pp. 423–427, 1980.

[26] J. COYNE and H. ELROD, “Conditions for the Rupture of a Lubricating Film-1,” *J. Lubr. Technol.*, pp. 451–456, 1969.

[27] D. J. Coyle, C. W. Macosko, and L. E. Scriven, “The fluid dynamics of reverse roll coating,” *AIChE J.*, vol. 36, no. 2, pp. 161–174, 1990.

[28] M. S. Carvalho, “Roll coating flows in rigid and deformable gaps,” *PhD Thesis, Univ. Minnestoa*, 1997.

[29] S. J. Weinstein and K. J. Ruschak, “Coating flows,” *Annu. Rev. Fluid Mech.*, vol. 36, pp.

29–53, 2004.

[30] J. P. Mmbaga, R. E. Hayes, F. H. Bertrand, and P. A. Tanguy, “Flow simulation in the nip of a rigid forward roll coater,” *Int. J. Numer. Methods Fluids*, vol. 48, no. 10, pp. 1041–1066, 2005.

[31] B. Malone, “An experimental investigation into roll coating phenomena,” *PhD Thesis, Univ. Leeds*, 1992.

[32] H. Thompson, “A theoretical investigation of roll coating phenomena,” *PhD Thesis, Univ. Leeds*, 1992.

[33] D. J. Coyle, “The Fluid Mechanics of Roll coating: Steady Flows, Stability, and Rheology,” *PhD Thesis, Univ. Minnesota*, 1984.

[34] O. Réglat and P. A. Tanguy, “Experimental Study of the Flow in the Metering Nip of a Metering-Size Press,” *AIChE J.*, vol. 43, no. 11, pp. 2911–2920, 1997.

[35] R. R. Myers, J. C. Miller, and A. C. Zettlemoyer, “The splitting of thin liquid films. Kinematics,” *J. Colloid Sci.*, vol. 14, no. 3, pp. 287–299, 1959.

[36] I. Hoogmartens, D. Vanderzande, H. Martens, and J. Gelan, “Flux distribution in forward roll coating,” *Chem. Eng.*, vol. 47, no. 3, pp. 367–371, 1992.

[37] M. Taroni, C. J. W. Breward, P. D. Howell, and J. M. Oliver, “Boundary conditions for free surface inlet and outlet problems,” *J. Fluid Mech.*, vol. 708, pp. 100–110, 2012.

[38] J. A. Moriarty and E. L. Terrill, “Mathematical modeling of the motion of hard contact lenses,” *Eur. J. Appl. Maths*, vol. 7, pp. 575–594, 1996.

[39] P. H. Gaskell, M. D. Savage, J. L. Summers, and H. M. Thompson, “Modelling and analysis of meniscus roll coating,” *J. Fluid Mech.*, vol. 298, no. 11, pp. 113–137, 1995.

[40] K. J. Ruschak, “Boundary conditions at a liquid/air interface in lubrication flows,” *J. Fluid Mech.*, vol. 119, pp. 107–120, 1982.

[41] M. R. Hopkins, “Viscous flow between rotating cylinders and a sheet moving between them,” *Br. J. Appl. Phys.*, vol. 8, no. 11, pp. 442–444, 1957.

[42] E. Pitts and J. Greiller, “The flow of thin liquid films between rollers,” *J. Fluid Mech.*, vol. 11, no. 1, pp. 33–50, 1961.

[43] P. H. Gaskell, G. E. Innes, and M. D. Savage, “An experimental investigation of meniscus roll coating,” *J. Fluid Mech.*, vol. 355, pp. 17–44, 1998.

[44] B. R. Duffy and S. K. Wilson, “Thin-film and curtain flows on the outside of a rotating horizontal cylinder,” *J. Fluid Mech.*, vol. 394, pp. 29–49, 1999.

[45] W. H. Banks and C. C. Mill, “Some Observations on the Behaviour of Liquids between Rotating Rollers,” *Proc. R. Soceity London. Ser. A, Math. Phys. Sci.*, vol. 223, no. 1154, pp. 414–419, 1954.

[46] G. I. Taylor, “Cavitation of a viscous fluid in narrow passages,” *J. Fluid Mech.*, vol. 16, no. 4, pp. 595–619, 1963.

[47] M. D. Savage, “Cavitation in lubrication. Part 1. On boundary conditions ant cavity-fluid interfaces,” *J. Fluid Mech.*, vol. 80, no. 4, pp. 743–755, 1977.

[48] S. D. R. Wilson and A. F. Jones, “The entry of a falling film into a pool and the air-entrainment problem,” *J. Fluid Mech.*, vol. 128, pp. 219–230, 1983.

[49] J. Quintans Carou, S. K. Wilson, N. J. Mottram, and B. R. Duffy, “Asymptotic and numerical analysis of a simple model for blade coating,” *J. Eng. Math.*, vol. 63, no. 2–4, pp. 155–176, 2009.

[50] M. Dalwadi, R. Cimpeanu, H. Ockendon, J. Ockendon, and T. Mullin, “Levitating a cylinder on a thin viscous film,” *APS Div. Fluid Dyn.*, 2020.

[51] J. Bico, J. Ashmore-Chakrabarty, G. H. McKinley, and H. A. Stone, “Rolling stones: The motion of a sphere down an inclined plane coated with a thin liquid film,” *Phys. Fluids*, vol. 21, no. 8, 2009.

[52] J. R. Smart, S. Beimfohr, and D. T. Leighton, “Measurement of the translational and rotational velocities of a noncolloidal sphere rolling down a smooth inclined plane at low Reynolds number,” *Phys. Fluids A*, vol. 5, no. 1, pp. 13–24, 1992.

[53] Y. J. Liu, J. Nelson, J. Feng, and D. D. Joseph, “Anomalous rolling of spheres down an inclined plane,” *J. Nonnewton. Fluid Mech.*, vol. 50, no. 2–3, pp. 305–329, 1993.

[54] M. Decré, E. Gailly, and J. M. Buchlin, “Meniscus shape experiments in forward roll coating,” *Phys. Fluids*, vol. 7, no. 3, pp. 458–467, 1995.

[55] P. J. Wicks, M. Decre, P. Planquart, and J. M. Buchlin, “Flow topoly associated with disjoint eddies in an asymetric film-splitting problem,” vol. 52, no. 2, pp. 2114–2121, 1995.

[56] M. Carvalho and L. Scriven, “Capillary and viscoelastic effects on elastohydrodynamic lubrication flow film splitting in roller nips,” *Int. Print. Graph. Arts Conf.*, 1994.

[57] M. Beccera, O. Romero, L. F. Azevedo, and M. Carvalho, “Measuring the velocity field in film-splitting flows of Newtonian fluids,” *AIChE J.*, vol. 53, no. 2, pp. 281–289, 2007.

[58] P. M. Schweizer, “Visualization of coating flows,” *J. Fluid Mech.*, vol. 193, pp. 285–302, 1988.

[59] L. Sartor, “Slot Coating: Fluid Mechanics and Die Design,” *PhD Thesis, Univ. Minnesota,*

1990.

[60] K. Chen, “Studies of Multilayer Slide Coating and Related Processes,” *PhD Thesis, Univ. Minnesota*, 1992.

[61] D. F. Benjamin, “Roll Coating Flows and Multiple Rolls Systems,” *PhD Thesis, Univ. Minnesota*, 1994.

[62] A. Clarke, “The application of particle tracking velocimetry and flow visualisation to curtain coating,” *Chem. Eng. Sci.*, vol. 50, no. 15, pp. 2397–2407, 1995.

[63] S. . Keller, “Roll coating in paper industry,” *Pulp Pap. Sci.*, vol. 18, pp. 44–48.

[64] A. E. Young, “A theoretical and experimental investigation of deformable roll coating,” *PhD Thesis, Univ. Leeds*, 1997.

[65] O. Reglat and P. A. Tanguy, “Rheological investigations of CaCO3 slurries in the metering nip of a metering size press,” *Tappi J.*, vol. 81, no. 5, pp. 195–205, 1998.

[66] J. Poranen, M. Kataja, A. Niemistö, N. Oy, and J. Grön, “A method for measuring and controlling the pressure in the metering nip of a metering size press coating process,” *Nord. Pulp Pap. Res. J.*, vol. 15, no. 5, pp. 486–493, 2000.

[67] G. Ascanio, P. J. Carreau, E. Brito-de la Fuente, and P. A. Tanguy, “Forward deformable roll coating at high speed with Newtonian fluids,” *Chem. Eng. Res. Des.*, vol. 82, no. 3, pp. 390–397, 2004.

[68] G. Ascanio, P. J. Carreau, and P. A. Tanguy, “High-speed roll coating with complex rheology fluids,” *Exp. Fluids*, vol. 40, no. 1, pp. 1–14, 2006.

[69] G. Ascanio and G. Ruiz, “Measurement of pressure distribution in a deformable nip of counter-rotating rolls,” *Meas. Sci. Technol.*, vol. 17, no. 9, pp. 2430–2436, 2006.

[70] M. S. Carvalho and L. E. Scriven, “Three-Dimensional Stability Analysis of Free Surface Flows: Application to Forward Deformable Roll Coating,” *J. Comput. Phys.*, vol. 151, no. 2, pp. 534–562, 1999.

[71] D. J. Coyle, C. W. Macosko, and L. E. Scriven, “Stability of symmetric film-splitting between counter-rotating cylinders,” *J. Fluid Mech.*, vol. 216, pp. 437–458, 1990.

[72] J. R. A. Pearson, “The instability of uniform viscous flow under rollers and spreaders,” *J. Fluid Mech.*, vol. 7, no. 4, pp. 481–500, 1960.

[73] M. E. Castillo and A. T. Patera, “Three-dimensional ribbing instability in symmetric forward-roll film-coating processes,” *J. Fluid Mech.*, pp. 323–335, 1997.

[74] G. C. Carter and M. D. Savage, “Ribbing in a variable speed two-roll coater,” *Math. Eng.*,

vol. 1, no. 1, 1987.

[75] P. H. Gaskell, N. Kapur, and M. D. Savage, “Bead-break instability,” *Phys. Fluids*, vol. 13, no. 5, pp. 1243–1253, 2001.

[76] M. Yamamura, “Ribbing instability of Newtonian fluid coated on a topographic surface,” *J. Coatings Technol. Res.*, vol. 17, no. 6, pp. 1447–1453, 2020.

[77] Y. Greener, T. Sullivan, B. Turner, and M. S., “Ribbing instability of a two-roll coater: Newtonian fluids,” *Chem. Eng. Comm.*, 1980.

[78] F. Varela López, L. Pauchard, M. Rosen, and M. Rabaud, “Non-Newtonian effects on ribbing instability threshold,” *J. Nonnewton. Fluid Mech.*, vol. 103, no. 2–3, pp. 123–139, 2002.

[79] Y. H. Chong, P. H. Gaskell, and N. Kapur, “Coating with deformable rolls: An experimental investigation of the ribbing instability,” *Chem. Eng. Sci.*, vol. 62, no. 15, pp. 4138–4145, 2007.

[80] J. H. Lee, S. K. Han, J. S. Lee, and J. Hyun, “Ribbing Instability in Rigid and Deformable Forward Roll Coating Flows,” *Korea Aust. Rheol.*, vol. 22, pp. 75–80, 2010.

[81] K. Tjiptowidjojo and M. S. Carvalho, “Operability limits of slide coating,” *Chem. Eng. Sci.*, vol. 66, no. 21, pp. 5077–5083, 2011.

[82] R. Stribeck, “Kugellager für beliebige Belastungen,” *Zeitschrift des Vereines Dtsch. Ingenieure*, vol. 46, pp. 1341–1348, 1902.

[83] G. Vogelpohl, “Thermal Effects and Elasto-Kinetics in Selfacting Bearing Lubrication,” *Proc. Int. Symp. Lubr. Wear*, pp. 766–815, 1965.

[84] X. Lu and M. M. Khonsari, “On the lift-off speed in journal bearings,” *Tribol. Lett.*, vol. 20, no. 3–4, pp. 299–305, 2005.

[85] X. Lu, “TRIBOLOGICAL ASPECTS OF JOURNAL BEARINGS FOCUSING ON THE STRIBECK CURVE,” *PhD Thesis, Louisiana State Univ.*, 2006.

[86] J. T. Burwell, J. Kaye, and D. A. Morgan, “Effects of Surface Finish,” *J. Appl. Mech.*, vol. 8, pp. 49–58, 1941.

[87] F. W. Ocvirk and G. B. DuBois, “Surface Finish and Clearance Effects on Journal-Bearing Load Capacity and Friction,” *J. Basic Eng.*, vol. 81, no. 2, pp. 245–252, 1959.

[88] F. A. Martin, “Minimum Allowable Oil Film Thickness in Steadily Loaded Journal Bearings,” *Proc. Inst. Mech. Eng.*, vol. 178, pp. 161–167, 1964.

[89] D. Dowson, “History of tribology, 2nd edition,” *Prof. Eng. Publ. London*, 1998.

[90] R. Kulakowski and E. W. Thickness, “Effect of Water-Film Thickness on Tire-Pavement Friction,” *ASTM Int.*, pp. 50–60, 1990.

[91] S. Vincent *et al.*, “Augmented Lagrangian and penalty methods for the simulation of two-phase flows interacting with moving solids. Application to hydroplaning flows interacting with real tire tread patterns,” *J. Comput. Phys.*, vol. 230, no. 4, pp. 956–983, 2011.

[92] Y. Nakajima, E. Seta, T. Kamegawa, and H. Ogawa, “Hydroplaning, Hydroplaning analysis by FEM and FVM-Effect of tire rolling and tire pattern on hydroplaning.” pp. 26–34, 2000.

[93] J. Löwer, P. Wagner, H. J. Unrau, C. Bederna, and F. Gauterin, “Dynamic measurement of the fluid pressure in the tire contact area on wet roads,” *Automot. Engine Technol.*, vol. 5, no. 1–2, pp. 29–36, 2020.

[94] M. A. Johnson, “Viscoelastic Roll Coating Flows,” *Chem. Eng.*, p. 131, 2003.

[95] H. Hayashi, “Recent studies on fluid film lubrication with non-Newtonian lubricants,” *JSME Int. J.*, vol. 34, no. 1, p. 2091, 1991.

[96] D. J. Coyle, C. W. Macosko, and L. E. Scriven, “Film-splitting flows of shear-thinning liquids in forward roll coating,” *AIChE J.*, vol. 33, no. 5, pp. 741–746, 1987.

[97] M. D. Savage, “Variable speed coating with purely viscous non-Newtonian fluids,” *ZAMP Zeitschrift für Angew. Math. und Phys.*, vol. 34, no. 3, pp. 358–369, 1983.

[98] R. W. Hewson and N. Kapur, “Effects of shear thinning on forward roll coating,” *Chem. Eng. Res. Des.*, vol. 91, no. 12, pp. 2427–2436, 2013.

[99] A. B. Ross, S. K. Wilson, and B. R. Duffy, “Blade coating of a power-law fluid,” *Phys. Fluids*, vol. 11, no. 5, pp. 958–970, 1999.

[100] S. Lee and J. Nam, “Transient response of slot coating flows of shear-thinning fluids to periodic disturbances,” *J. Coatings Technol. Res.*, vol. 14, no. 5, pp. 981–990, 2017.

[101] T. Bauman, T. Sullivan, and S. Middleman, “Ribbing instability in coating flows: effect of polymer additives,” *Chem. Eng. Comm.*, vol. 14, pp. 35–46, 1982.

[102] G. A. Zevallos, M. S. Carvalho, and M. Pasquali, “Forward roll coating flows of viscoelastic liquids,” *J. Nonnewton. Fluid Mech.*, vol. 130, no. 2–3, pp. 96–109, 2005.

[103] F. Ali, Y. Hou, M. Zahid, and M. A. Rana, “Theoretical study of the reverse roll coating of non-isothermal magnetohydrodynamics viscoplastic fluid,” *Coatings*, vol. 10, no. 10, pp. 1–27, 2020.

[104] M. Pasquali and L. E. Scriven, “Free surface flows of polymer solutions with models based on the conformation tensor,” *J. Nonnewton. Fluid Mech.*, vol. 108, no. 1–3, pp. 363–409, 2002.

[105] M. Bajaj, J. Ravi Prakash, and M. Pasquali, “A computational study of the effect of viscoelasticity on slot coating flow of dilute polymer solutions,” *J. Nonnewton. Fluid Mech.*, vol. 149, no. 1–3, pp. 104–123, 2008.

[106] D. T. Eadie *et al.*, “The effects of top of rail friction modifier on wear and rolling contact fatigue: Full-scale rail-wheel test rig evaluation, analysis and modelling,” *Wear*, vol. 265, no. 9–10, pp. 1222–1230, 2008.

[107] D. T. Eadie and M. Santoro, “Top-of-rail friction control for curve noise mitigation and corrugation rate reduction,” *J. Sound Vib.*, vol. 293, no. 3–5, pp. 747–757, 2006.

[108] D. T. Eadie, M. Santoro, and J. Kalousek, “Railway noise and the effect of top of rail liquid friction modifiers: Changes in sound and vibration spectral distributions in curves,” *Wear*, vol. 258, no. 7–8, pp. 1148–1155, 2005.

[109] A. Matsumoto *et al.*, “Improvement of bogie curving performance by using friction modifier to rail/wheel interface verification by full-scale rolling stand test,” *Wear*, vol. 258, no. 7–8, pp. 1201–1208, 2005.

[110] Y. L. Cotter J, D. Eadie, D. Elvidge, N. Hooper, J. Roberts, T. Makowsky, “Top of rail friction control: reductions in fuel and greenhouse gas emissions,” in *Proceedings of the Eighth International Heavy Haul Association Conference, Rio de Janeiro, Brazil*, 2005, pp. 327–333.

[111] D. V. Gutsulyak, L. J. E. Stanlake, and H. Qi, “Twin disc evaluation of third body materials in the wheel/rail interface,” *Tribol. - Mater. Surfaces Interfaces*, pp. 1–12, 2020.

[112] L. Stanlake, “Film Splitting of Liquid Friction Modifier Formulations in the Wheel-Rail Contact,” *LB Foster Frict. Manag.*, 2012.

[113] M. Harmon and R. Lewis, “New laboratory methodologies to analyse the top of rail friction modifier performance across different test scales,” *Proc. Inst. Mech. Eng. Part F J. Rail Rapid Transit*, vol. 235, no. 2, pp. 191–200, Feb. 2021.

[114] M. Harmon, B. Powell, I. Barlebo-Larsen, and R. Lewis, “Development of Grease Tackiness Test,” *Tribol. Trans.*, vol. 62, no. 2, pp. 207–217, Mar. 2019.

[115] P. D. Temple, M. Harmon, R. Lewis, M. C. Burstow, B. Temple, and D. Jones, “Optimisation of grease application to railway tracks,” *Proc. Inst. Mech. Eng. Part F J. Rail Rapid Transit*, vol. 232, no. 5, pp. 1514–1527, May 2018.

[116] K. Chiddick, B. Kerchof, and K. Conn, “Considerations in choosing a top of rail (TOR) material,” *AREMA Annu. Conf. Expo.*, pp. 1–21, 2014.

[117] Y. Lemma, M. Asplund, and M. Rantatalo, “Top-of-rail friction measurements of the Swedish iron ore line,” *Proc. 3rd Int. Work. Congr. eMaintenance, Lulea , Sweden*, 2014.

[118] S. A. Khan, J. Lundberg, and C. Stenström, “Carry distance of top-of-rail friction modifiers,” *Proc. Inst. Mech. Eng. Part F J. Rail Rapid Transit*, vol. 232, no. 10, pp. 2418–2430, 2018.

[119] D. Eadie *et al.*, “Implementation of wayside top of rail friction control on North American heavy haul freight railways,” in *Proceedings of the Seventh World Congress on Railway Research, Montreal*, 2006, p. 10.

[120] H. Dakhil, D. Auhl, and A. Wierschem, “Infinite-shear viscosity plateau of salt-free aqueous xanthan solutions,” *J. Rheol. (N. Y. N. Y).*, vol. 63, no. 1, pp. 63–69, 2019.

[121] P. J. Whitcomb and C. W. Macosko, “Rheology of Xanthan Gum,” *J. Rheol. (N. Y. N. Y).*, vol. 22, no. 5, pp. 493–505, 1978.

[122] W. Jeong and D. Jeong, “Acoustic roughness measurement of railhead surface using an optimal sensor batch algorithm,” *Appl. Sci.*, vol. 10, no. 6, pp. 1–11, 2020.

[123] M. Naeimi, Z. Li, and R. Dollevoet, “Scaling strategy of a new experimental rig for wheel-rail contact,” *Int. J. Mech. Aerospace, Ind. Mechatronics Eng.*, vol. 8, no. 12, 2014.

[124] J. Gerlici and T. Lack, “Railway wheel and rail head profiles development based on the geometric characteristics shapes,” *Wear*, vol. 271, no. 1–2, pp. 246–258, 2011.

Appendices

Appendix A Supplementary results for the Newtonian pool

Here we provide some additional results for lubricated rolling over a Newtonian pool, some of which are referenced in Chapter 2.

Figure A. 1 shows the deposited film on the track for all five interactions, analogous to Figure 2-7 in the main body. However, here to remove the distraction of the filamentary or droplet pattern in the deposited films, we average thicknesses over windows with size (2 mm × 2 mm) exceeding the filament or droplet separations. As mentioned, there is a clear variation in average film thickness in the lateral direction, with nearly uniform thickness (consistent with the uniform gap between the wheel and blade) over the middle half of the wheel and a tapering towards the sides. Evidently, fluid is redistributed by the dynamics of detachment at the sides, as well as the film splitting instability.

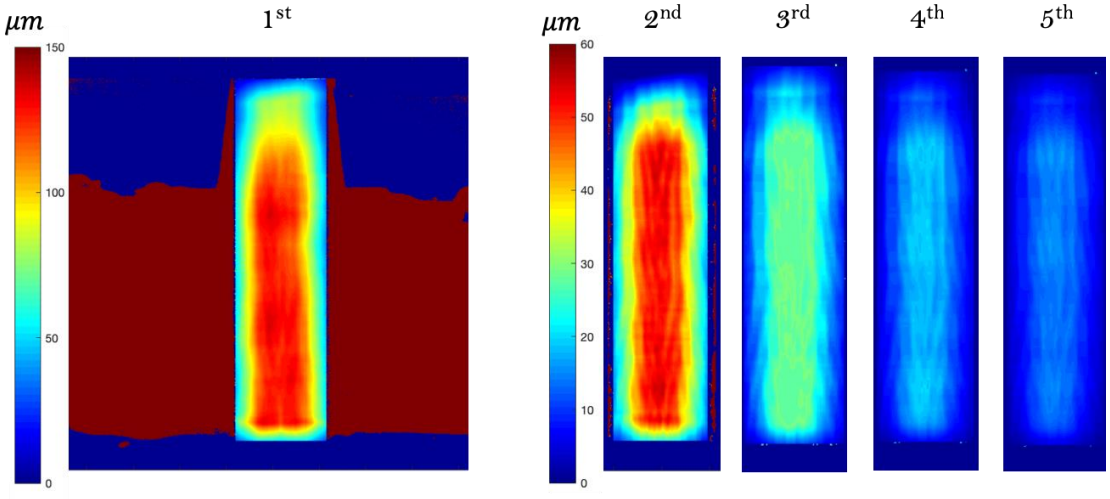

Figure A. 1 Averaged thickness distribution after the passage of the wheel. Two color bars are used for graph clarity. U=1 m/s, L/W=11.2 kN/m, μ=8.72 Pa·s (silicone oil), W=10 mm, and h_{in}=500 μm.

The ratio of the gap size to the coated thickness, both averaged over l_c (the steady state region), is shown in Figure A. 2 for the bulk of experimental conditions (one sample of this comparison is shown in Figure 2-8). Eliminating the printing interactions, the average of measurements is $\frac{h_0}{h_{out}} = 1.83 \pm 0.14$ for Interactions One and Two only, where h_0 is the gap size and h_{out} is the coated thickness, and that is consistent with the model predictions.

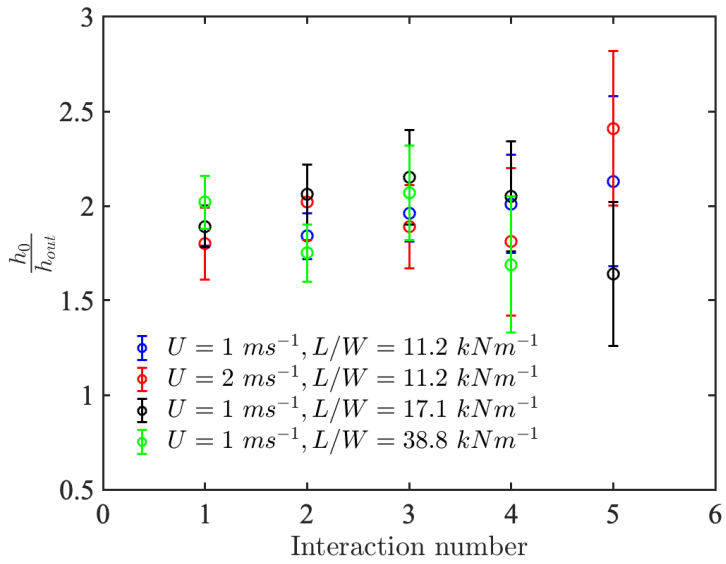

Figure A. 2) The ratio of the gap size to the film thickness for multiple experimental parameters.

The influence of the wheel width on Interaction One is shown in Figure A. 3 for a series of experiments in which the ratio of wheel load, L, to wheel width, W, was fixed to maintain a similar lubrication dynamics. In view of the constant average pressure, if there were no side flux, one would expect an identical film thickness for different wheel widths. However, the average film thickness over the length l_c (Figure 2-10) significantly reduces for thinner wheels due to the comparatively larger side flux. In addition, the number of filaments (or the ribbing wavelength) varies with the wheel width. The ribbing wavelengths are λ=0.5, 1.3, 2.3 mm for W=5, 10, 20 mm, respectively.

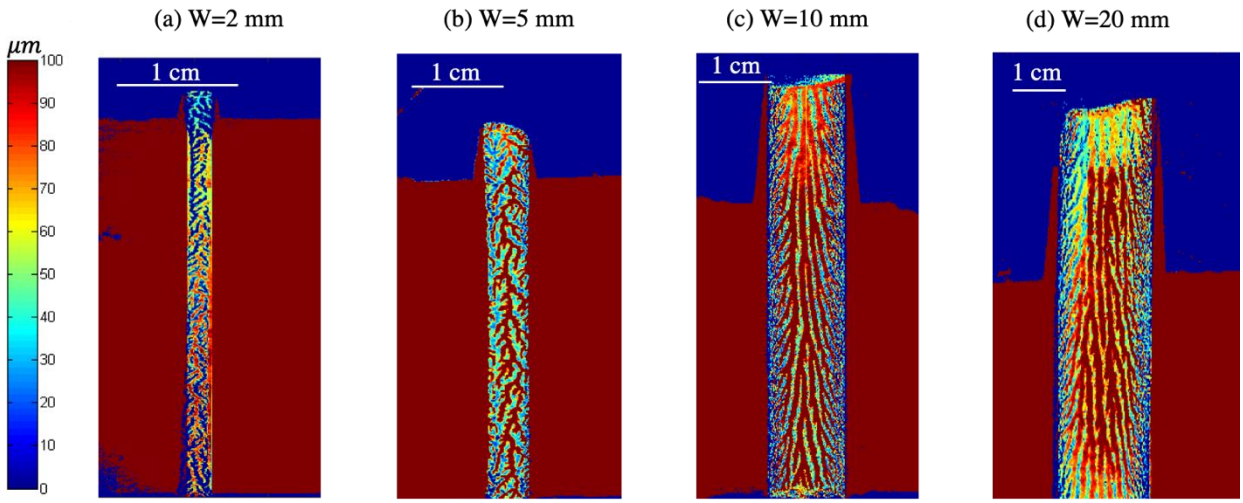

Figure A. 3 LIF images of the deposited liquid on the track for different wheel widths after Interaction One.

Figure A. 4 summarizes the full set of experiments, displaying the coated film thicknesses, averaged over l_c, versus the Interaction number for various speeds (a, b), loads (c), wheel widths (d), and viscosities (e). The gap size increases with increasing viscosity, speed, and decreases with increasing applied load, which are all consistent with the dynamics of lubrication mechanism. Owing to the higher degree of side flux, the gap size decreases markedly with the wheel width under the fixed load-to width ratio.

The centerline pressures for various test conditions are also presented in Figure A. 5. For all experiments, the subatmospheric pressure likely matches the vapor pressure of the liquids. The peak pressure increases with the applied load and decreases with viscosity or speed. In other words, the peak pressure increases for the smaller gap sizes. The wetted length, the length over which the lubrication pressure develops, varies with the test parameters and increases for the larger gap sizes.

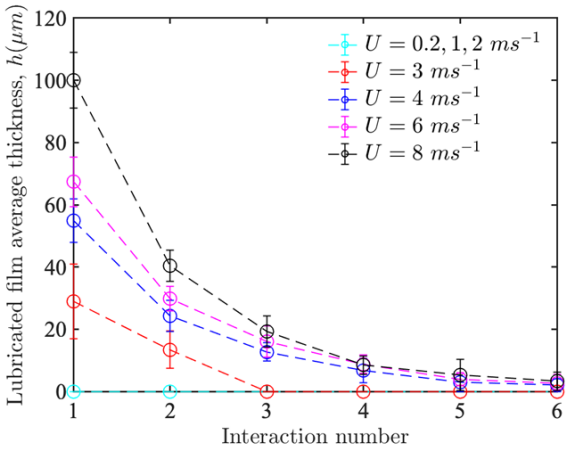

(a) $\mu = 1.19\ Pa.s$ (*glycerin*), $\frac{L}{W} = 11.2\ kNm^{-1}, W = 10\ mm$

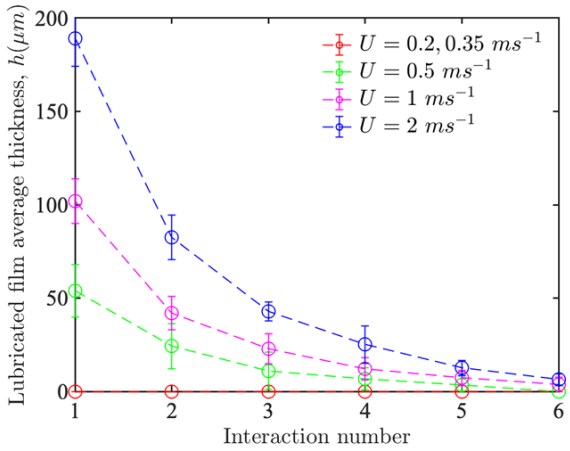

(b) $\mu = 8.72\ Pa.s$ (*silicone oil*), $\frac{L}{W} = 11.2\ kNm^{-1}, W = 10\ mm$

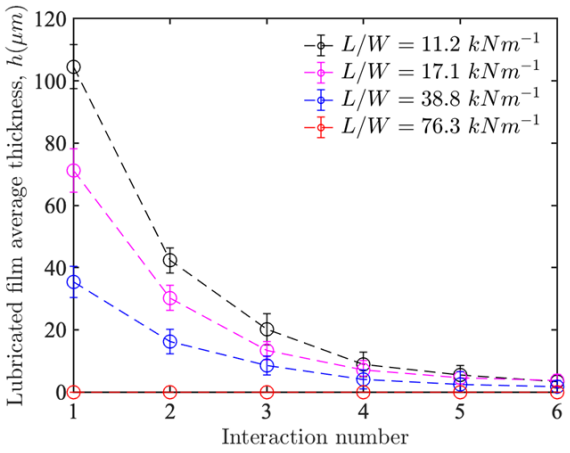

(c) $U = 1\ ms^{-1}$, $\mu = 8.72\ Pa.s$ (*silicone oil*), $W = 10\ mm$

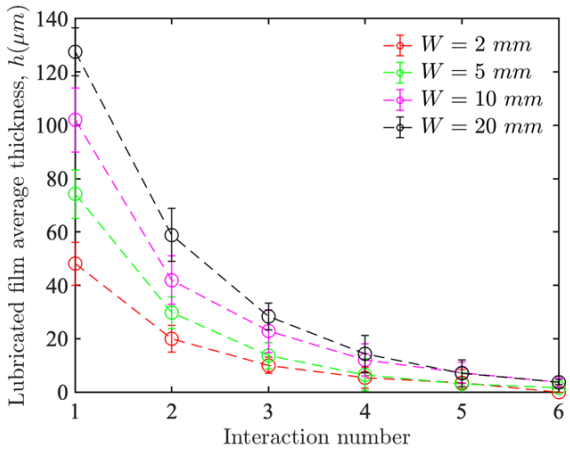

(d) $\mu = 8.72\ Pa.s$, $\frac{L}{W} = 11.2\ kNm^{-1}, U = 1\ ms^{-1}$

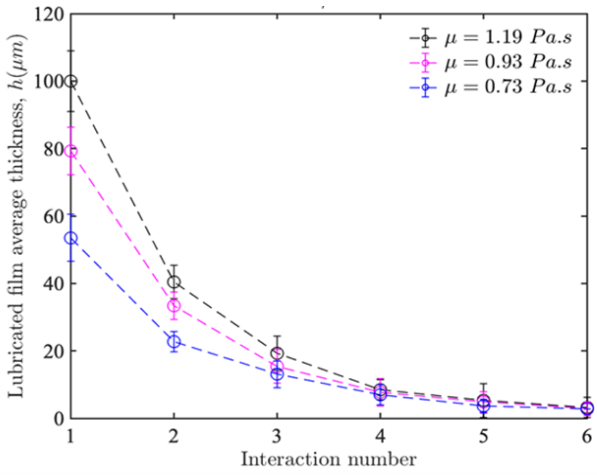

(e) $\frac{L}{W} = 11.2\ kNm^{-1}, U = 8\ ms^{-1}$, W=10 mm

Figure A. 4 Film thickness versus Interaction number for various a) speeds with glycerin liquid pool, b) speeds with silicone oil liquid pool, c) applied loads, d) width, and e) viscosities.

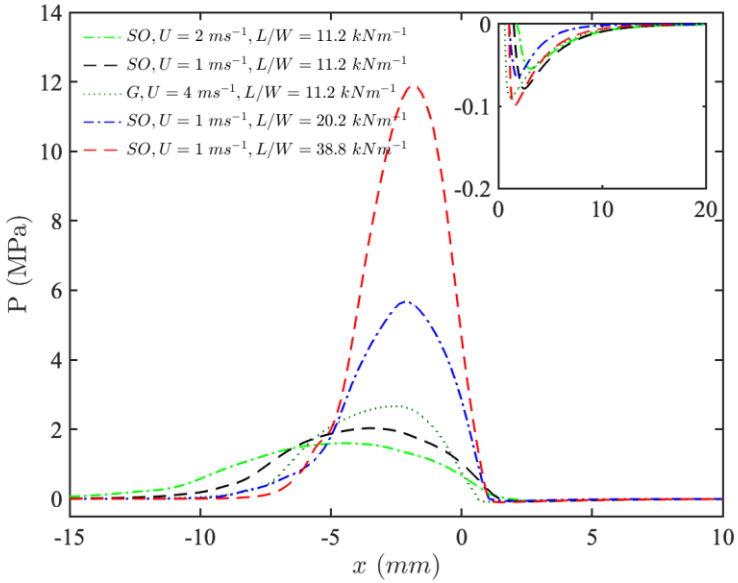

Figure A. 5 Centerline pressure profiles (z=0) versus the axial distance for various experimental conditions. 'SO' refers to silicone oil and 'G' refers to glycerin. The wheel width is 20 mm.

In what follows next, we present additional sample solutions of the model. In Figure A. 6, the solutions include the dimensionless pressure (right axis) and the dimensionless axial flux (left axis) for two arbitrarily chosen upstream position ξ_L. The pressure is normalized by $P = \frac{ph_0^{\frac{3}{2}}}{\mu U R^{\frac{1}{2}}}$ and the axial flux is normalized by $\lambda = \frac{\int_0^h u\, dy}{Uh_0}$. For 2D flows (infinitely wide wheels) with no side flux, λ is constant over the wetted length. The pressure distribution in 3D is similar to that in 2D; however, the integral of the dimensionless pressure (or equivalently the dimensionless load) reduces when the flow is 3D. Therefore, under identical test conditions, the load-carrying capacity of the system reduces. In the present study, since the applied load is fixed, the minimum gap size must reduce instead to account for 3D effects and the side leakage, which is in agreement with the observations. In the presence of side flux, the liquid is squeezed out laterally upstream of the nip and λ decreases with downstream distance. The liquid may re-enter the contact band at the nip exit due to the negative pressure in the fluid. In fact, this suction has been observed by our industrial partners both in the lab and in the field. The suction is not very pronounced in theory as the magnitude of negative pressure (the vapor pressure) is small relative to the magnitude of the peak positive pressure.

Dimensional pressures for various pool depths are plotted in Figure A. 7 for the thin wheel. For deep pools, the pressure profile is virtually independent of the pool depth. In contrast, for shallow pools, as the pool depth decreases the wetted length decreases, and the peak pressure increases (to ensure the load is supported). The wetted length underneath the wheel ($x_m - x_l$) is shorter than the pool length in the experiments, and this difference is particularly true for the higher interactions (smaller h_{in}).

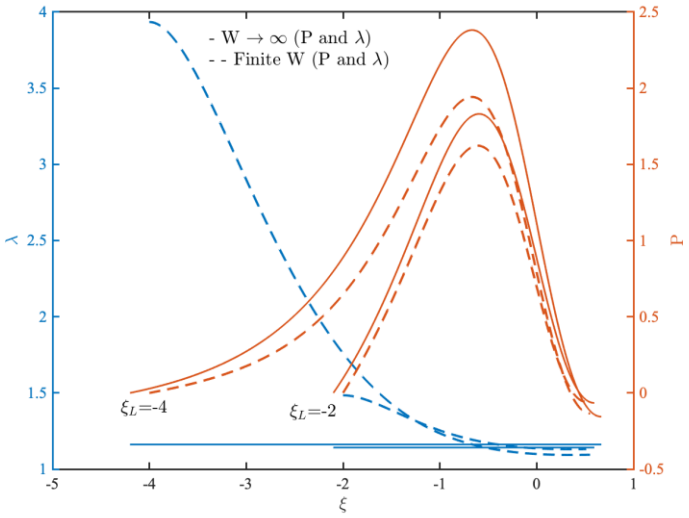

Figure A. 6 Non-dimensional pressure distribution (right axis) and non-dimensional axial flow rate (left axis) when the width is infinitely wide (3D flow) and when there is a side flux (dashed lines). The applied load is fixed in all cases.

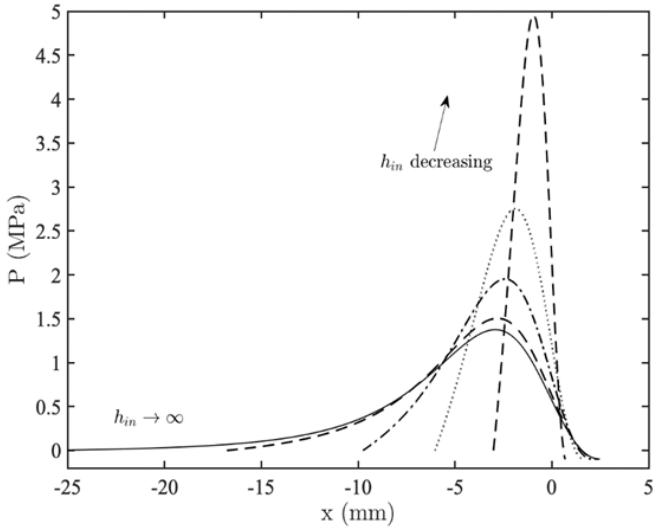

Figure A. 7 Sample dimensional pressures under the wheel using the 3D lubrication analysis. As pool depth reduces, the wetted length decreases and the peak pressures rise. h_{in} is varied from a very large number (h_{in}=1000 µm, above which the pressure is independent of the pool depth) to h_{in}=40 µm.

Appendix B Model for the cambered wheel

B.1 Problem formulation

Here, we extend the lubrication analysis to model the cambered wheel rolling over a Newtonian fluid resting on the substrate. Obviously, the model only applies to the situation where the cambered wheel is lifted off from the substrate by a viscous fluid. Although we have experimentally shown in Chapter 4 that no liftoff is observed for a range of conditions tested in this study, it is believed that liftoff would occur for significantly lower applied loads. In that outcome, the following analysis is useful to explain the observations.

First, we formulate the problem in general settings and then simplify it in a same fashion as we did before to model the fluid loss to the sides. We use the same Cartesian coordinate system and notations that were introduced in Chapter 2. The Reynolds equation does not change for the cambered wheel and is specified in equation (2-8). However, here the gap size, which was only a function of x for the cylindrical wheel, is now a function of both x and z:

$$h(x,z) \approx h_0 + \frac{x^2}{2R} + \frac{z^2}{2R_c}, \qquad \textbf{B. 1}$$

where R is the cambered wheel radius and R_c is the radius of curvature for crowning. In the nip region from the upstream jump to the downstream meniscus, x and z are much smaller than R and R_c (respectively), $x \ll R$ and $z \ll R_c$, validating the approximation made in (B. 1). On the wheel and rail surface, we have no slip condition (equations 2-6 and 2-7). The pressure is set to zero on the jump and is truncated at the vapor pressure at the meniscus. In z, the pressure is zero at the wheel edge and is symmetrical at the wheel centerline. The pressure boundary conditions are summarized as

$$p(x_l, z) = 0 \qquad and \qquad p(x_m, z) = p_{vap} - p_{atm}$$
$$p\left(x, \frac{1}{2}W\right) = 0 \qquad \textbf{B. 2}$$
$$p_z(x, 0) = 0.$$

Treatment of the jump and meniscus is even more complicated for the cambered wheel in view of the highly three-dimensional flow there and the highly curved surfaces in (x, z)-plane. The flux conservation at the upstream boundary demands that the fluid flux normal to the jump surface has to be continuous:

$$\boldsymbol{Q}.\hat{\boldsymbol{n}} = \boldsymbol{Q_{in}}.\boldsymbol{i}, \qquad \textbf{B. 3}$$

where $\boldsymbol{Q}$ is the vector of the flow rate per unit width of the wheel $\boldsymbol{Q} = (Q^x, Q^z) = (\frac{-h^3}{12\mu}p_x + Uh, \frac{-h^3}{12\mu}p_z)$, $\hat{\boldsymbol{n}}$ is the unit vector normal to the jump surface in (x, z)-plane**,** $\boldsymbol{Q_{in}}$ is the vector of incoming flux $\boldsymbol{Q_{in}} = (uh_{in}, 0)$**,** and $\boldsymbol{i}$ is the unit vector in x-direction. Therefore, the jump condition reduces to

$$Q_{in} = \left[Uh - \frac{h^3}{12\mu}p_x + \frac{h^3}{12\mu}p_z\frac{dx}{dz}\right]_{x=x_l}. \qquad \textbf{B. 4}$$

At the meniscus, we assume a stagnation point at the center of the film. This condition dictates that the velocity normal to the meniscus surface in (x, z)-plane to be zero at points midway between two surfaces

$$\boldsymbol{u}.\hat{\boldsymbol{n}} = 0, \qquad \textbf{B. 5}$$

where $\boldsymbol{u}$ is the velocity vector that is found by integrating the momentum equations (equation (2-3) and 2-5) twice with respect to y, $\boldsymbol{u} = (u, w) = (U - \frac{p_x}{2\mu}y(h - y), -\frac{p_z}{2\mu}y(h - y))$. The meniscus condition then reduces to

$$\left[U - \frac{p_x}{2\mu} y(h-y) + \frac{p_z}{2\mu} y(h-y) \frac{dx}{dz}\right]_{x=x_m} = 0 \qquad at \qquad y = \frac{h_m}{2}. \tag{B. 6}$$

Now we have closed the equation system with the required conditions. Similar to previous chapters, to avoid complications arising from this free-boundary problem where the positions of x_l, x_m, and their associated curves in (x, z)-plane are not known at the outset, we make some simplifying assumptions, as follows.

B.2 Approximations

Similar to the analysis for a cylindrical wheel, we adopt an approximation in which we assume that the wheel is wide enough that the sides of the wheel play negligible role in the flow domain. We further assume that x_l and x_m are independent of z, although it is unlikely that this approximation holds for the cambered wheel. We also employ the similar dimensional analysis to relate the pressure gradient at the edge to the average pressure $\bar{p}$, using the length scale for the wide wheel (i.e., $\sqrt{Rh_0}$). We re-write the gap size as $h(x,z) = h_0 + \frac{x^2}{2R} + \frac{z^2}{2R_c} = h'(x) + \frac{z^2}{2R_c}$ and replace it in 2-12 to get

$$\frac{\partial}{\partial x}\left(Uh' - \frac{\bar{p}_x}{12\mu}\left(h'^3 + h'^2 \frac{W^2}{8R_c} + h' \frac{3W^4}{320R_c^2} + \frac{W^6}{3584R_c^3}\right)\right) = \frac{\left(h' + \frac{W^2}{8R_c}\right)^3 \bar{p}}{6\mu W \Delta}, \tag{B. 7}$$

in the dimensional coordinate. It is convenient to define the non-dimensional variables as $\xi = \frac{x}{\sqrt{Rh_0}}, \eta = \frac{y}{h_0}$, and $P = \frac{p h_0^{\frac{3}{2}}}{\mu U R^{1/2}}$. Then, (B. 7) becomes

$$\frac{\partial}{\partial\xi}\left(\eta-\frac{\bar{P}_{\xi}}{12}(\eta^3+\eta^2\frac{W^2}{8R_ch_0}+\eta\frac{3W^4}{320(R_ch_0)^2}+\frac{W^6}{3584(R_ch_0)^3})\right) \quad \textbf{B. 8}$$
$$=\frac{C\sqrt{Rh_0}}{6W}\left(\eta+\frac{W^2}{8R_ch_0}\right)^3\bar{P},$$

in the dimensionless coordinate. The ratio $\frac{W^2}{R_ch_0}$ is the non-dimensional wheel width for cambered wheels and highlights the significance of the crowning. For flat wheels ($R_c\to\infty$), this ratio disappears and the equation reduces to the equation presented for the cylindrical wheel (2-10). On the other hand, the crowning effects become increasingly important for high values of $\frac{W^2}{R_ch_0}$, or equivalently for smaller R_c. The typical value for this ratio in the experiment is $\frac{W^2}{R_ch_0}\approx 10$, based on the experimental conditions of $W=20\ mm$, $h_0=100\ \mu m$, and $R_c=400\ mm$.

B.3 Sample solutions

To provide some physical insights into the solutions of the model, we display a family of solutions for non-dimensional pressure (Figure B. 1 (a)) and non-dimensional axial flux λ (Figure B. 1 (b)) for various ratios $\frac{W^2}{R_ch_0}$. In Figure B. 2, we display the dimensional pressure versus the axial distance (a), the minimum gap variation versus crowning ratio (b), and the fraction of the fluid that is diverged to the sides (c). All model predictions are physically sensible. For higher value of $\frac{W^2}{R_ch_0}$, more liquid leaks to the sides, resulting in a shorter wetted length and larger peak pressure. To plot the following graphs, we used the same value of C fitted to the experiments for the cylindrical wheel over the Newtonian pool, however it would be nice to confirm it experimentally in the future works.

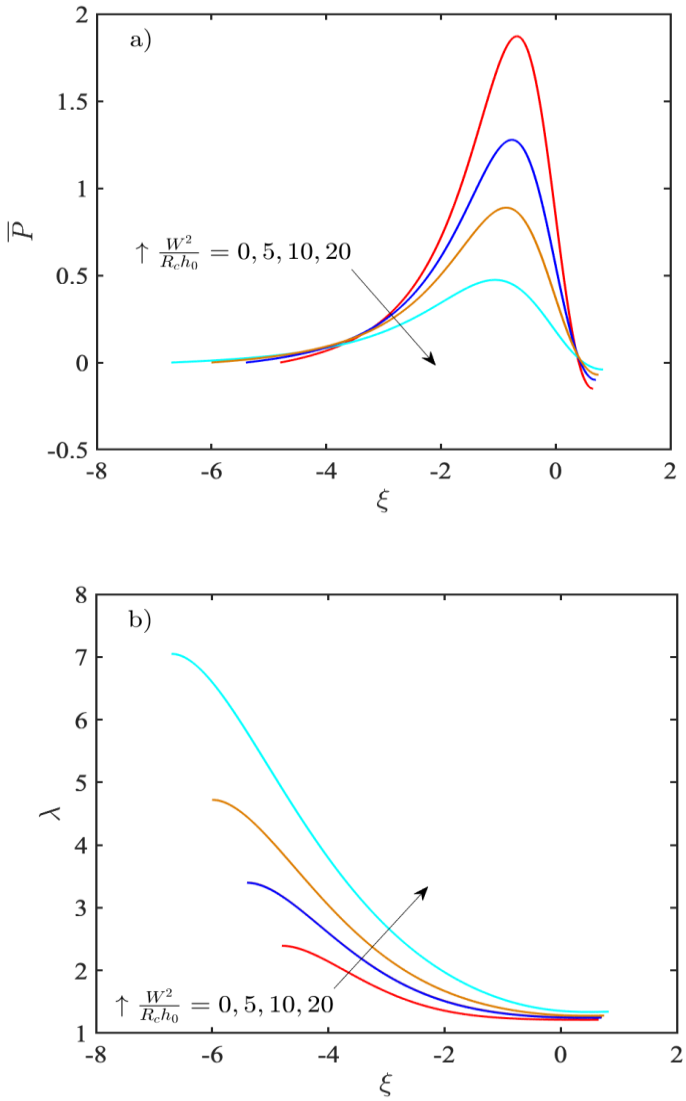

Figure B. 1 Model predictions for the cambered wheel, displaying the non-dimensional pressure (a) and axial flux (b) versus non-dimensional x-axis. Obviously, for the cambered wheels the dimensionless load reduces, resulting in a lower load-carrying capacity of the system under identical conditions. Total load is fixed for all cases. U=1 m/s, L/W=11.2 kN/m, μ=8.72 Pa·s, and W=20 mm.

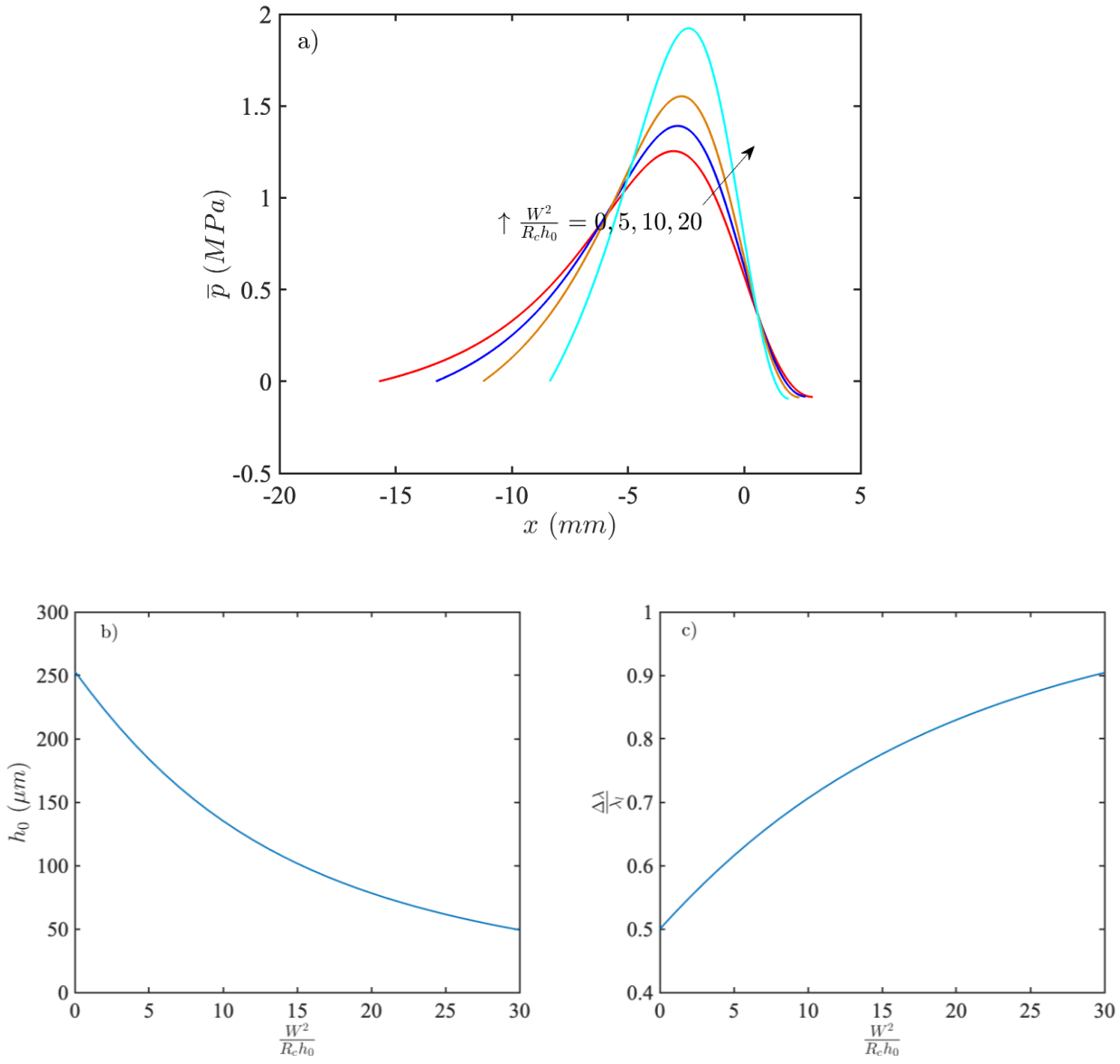

Figure B. 2 Dimensional pressure (a), minimum gap size (b), and the side-flux fraction (c) as a function of the $\frac{W^2}{R_c h_0}$. Test conditions are: U=1 m/s, L/W=11.2 kN/m, μ=8.72 Pa·s, and W=20 mm.